EVALUATION OF MESOSCALE SIMULATIONS OF DUST SOURCES, SINKS AND TRANSPORT OVER THE MIDDLE EAST

by Michael A. Smith

William R. Cotton, P.I.

Colorado State University

DEPARTMENT OF ATMOSPHERIC SCIENCE

Paper No. 785

EVALUATION OF MESOSCALE SIMULATIONS OF DUST SOURCES, SINKS AND TRANSPORT OVER THE MIDDLE EAST

by

Michael A. Smith

Department of Atmospheric Science

Colorado State University

Fort Collins, CO 80523-1371

August 10,2007

Atmospheric Science Paper No. 785

ABSTRACT

EVALUATION OF MESOSCALE SIMULATIONS OF DUST SOURCES, SINKS AND
TRANSPORT OVER THE MIDDLE EAST

Desert dust is ubiquitous in the Earth's atmosphere, with measurable concentrations found everywhere from the Middle East to Antarctica. It has the ability to alter the global radiation balance and affects the African Easterly Jet, along with hypothesized roles in hurrican formation and past climate change. In addition to these large-scale effects, dust can have a deleterious effect on regional hydrology, air quality and visibility. Recent military activity in the Middle East has led to increased interest in looking beyond global models that are chiefly concerned with long distance transport, to mesoscale models capable of resolving smaller scales and incorporating more elaborate radiation and microphysics schemes.

Following the work of Stokowski (2005), who introduced a modification that allowed dust to be radiatively active, a dust emission and deposition module has been added to the CSU Regional Atmospheric Modeling System [RAMS]. The new scheme utilizes a global map of potential sources and parameterizes emissions based on model wind speed and soil moisture. Though many existing models incorporate dust as an offline tracer, RAMS allows it to advect and feed back into the model, affecting the long and shortwave radiative balance at each timestep. Removal is done via Brownian diffusion, gravitational deposition and rain scavenging.

This study focuses on the testing of the new scheme, with emphasis on its ability to accurately model the spatial extent of dust as well as the column optical thickness and surface visibility. Validation is done through a combination of NCEP reanalyzed meteorological maps, Aeronet AOT and back-trajectory data and surface observations. RAMS did well in predicting the areal extent of elevated dust as well as visibility within the higher-resolution nested grid. Prediction of visibility and optical thickness values in the coarse grid exhibited larger absolute errors, though the latter was generally predicted within a factor of two. A persistent dry bias was found through comparison of sounding data with model output. This is thought to be due to the initialization data, and resulted in sometimes-poor simulation of precipitation areal extent, explaining several of the erroneous forecast values.

The work done in this study paves the way for future improvements to the RAMS model, the most important being the addition of dust effects on model microphysics. The structure of the dust scheme also allows for parameters such as in-situ size distribution to be tuned to known regional values, thus presumably improving forecast ability. Several such data sets are already in existence although they were not available for this study.

Michael A. Smith
Department of Atmospheric Science
Colorado State University
Fort Collins, Colorado 80523-1371
Fall 2007

ACKNOWLEDGEMENTS

CONTENTS

FIGURES

Chapter   1

INTRODUCTION

Desert dust, or more generally mineral dust, is a ubiquitous element in the Earth's atmosphere. It has the ability to affect global radiation balance and possibly played a role in past climate change. As observational and modeling capabilities advance, so does our ability to more accurately resolve the impact of the dust that is emitted and transported throughout the most remote regions of the world. At present there is still great uncertainty regarding many characteristics of atmospheric dust. This chapter presents a brief introduction to the current state of knowledge regarding mineral dust, followed by a summary of recent modeling efforts, and finally the goals of the present study.

1.1   Mineral Dust and the Atmosphere

Mineral dust is one of the most prominent natural aerosols in the atmosphere [Yin et al. (2002)], with some studies estimating that it constitutes 45% of the total global aerosol burden [Brooks (2000)]. There is still much disagreement regarding how much of this burden is from 'natural' sources, versus anthropogenic sources such as farming. Meloni et al. (2004) report that 'a significant fraction of dust in the atmosphere is produced by man-induced changes' while Prospero et al. (2002) attribute 'a significant' proportion of global dust to natural sources and Tegen et al. (2004) estimate that dust from agricultural sources makes up less than 10% of the total atmospheric burden. Globally, the strongest and most consistent sources are the Sahara-Sahel region of Northern Africa [Formenti et al. (2003)]

and the Gobi and Taklamakan deserts of China and Mongolia. The Sahara-Sahel region has historically been the most intensly- studied, and various authors [Brooks (2000), Nicholson (2000), Mbourou et al. (1997)] have noted that in recent decades the Sahel has eclipsed the Sahara in terms of mass emissions, with one theory being that most of the erodible material in the Sahara was removed during the drought years of the 1970s. Estimates of total global dust emissions vary widely, with recent studies quoting anywhere from 1000 to 2150 Tgyr^{-1} [IAPSAG (2006)].

The introduction of mineral dust aerosols into the atmosphere depends on many factors including soil moisture, wind speed and grain size distribution. Natural sources are typically associated with topographical lows, in regions with annual rainfall not exceeding 200–250mm: Major sources often contain deep alluvial deposits, evidence of periodic flooding [Prospero et al. (2002)]. Often large particles contribute to the loosening of smaller particles as they bounce along the ground in a process known as saltation. Once dust is lofted from the ground, it may be lifted high into the troposphere by intense convection or frontal uplift and transported long distances. Mbourou et al. (1997) observed a seasonal dust maximum over the Sahara during its wet season, which they attributed to dust mobilization by vigorous convection. Tegen and Fung (1994) define the largest radius for lofting to be 50μm, whereas larger particles have atmospheric lifetimes of less than one hour. Typical removal mechanisms include rain washout, cloud scavenging and gravitational deposition. Emission and removal mechanisms are addressed in a variety of ways by the models described in section 1.2, and a more detailed description of the approach to the problem of dust mobilization and transport used in this study is detailed in Chapter 2.

Dust that is lofted high into the troposphere has been shown to consistently travel very long distances, from both Africa and Asia to North America. A typical transport episode from Nothern Africa involves the injection of dust into the Saharan Air Layer (SAL), a warm, dry mass beginning at around 850hPa. This layer of air is forced up over

the cooler moist air overlying the Atlantic Ocean and is advected to the West, aided by the African Easterly Jet (AEJ). Dust itself plays an important role in determining the strength of the AEJ. Karyampudi and Carlson (1988) showed that a stronger and broader AEJ developed under conditions of heavy dust loading. The AEJ in turn is critical to the formation of easterly waves and convective disturbances [Mbourou et al. (1997)], which then propogate out into the ocean. Transport times accross the Atlantic are on the order of 7 to 10 days and are influenced by the seasonal displacement of the ITCZ. This has been observed and modeled in numerous studies [e.g. PRIDE, DABEX, CRYSTAL FACE]. Perry et al. (1997) used observations to conclude that incursions of North African dust over the North American continent occur on average three times per year and that during these periods dominate local fine soil dust by an order of magnitude or more. Asian dust production and transport has been studied more frequently in recent years, notably during ACE-ASIA [Gong et al. (2003)] during the spring of 2001 and PACDEX in the spring of 2007. Historically it has been assumed that transport across the Pacific occurred only during the spring, however VanCuren and Cahill (2002) found that fine [$<2.5\mu$m] Asian dust is regularly present in the troposphere over Western North America. Uno et al. (2004) and Nickovic et al. (2001) emphasize the need for more detailed studies to reduce uncertainties in, respectively, Sahara-Sahel and Asian dust emission and transport.

Mineral dust has the potential to affect many characteristics of the atmosphere including radiative balance, cloud formation and cloud microphysics, with several studies [e.g. Mahowald et al. (1999)] examining the linkage between dust and climate change in glacial and interglacial periods. Perhaps the best (though still poorly) understood of these are radiative effects, which can influence forecast fields such as surface temperature and boundary layer processes [Wang et al. (2004)]. Mineral dust affects the radiation balance in both the shortwave (solar) and longwave (terrestrial) spectra [Fan et al. (2004)]. The radiative effects may be characterized by considering them as a sum of the direct, indirect

and semi-direct effects. The direct effect is the radiative absorption, scattering and emission due to suspended dust. Myhre et al. (2003) note that the longwave direct radiative impact is always positive, though the magnitude depends on several intrinsic characteristics of the dust [Myhre and Stordal (2001), Hansen et al. (1997)]. These parameters, as well as actual emissions, chemical composition and in-situ size distribution were found to be subject to a high level of uncertainty and a 'low level of scientific understanding' [IPCC (2001)]. In fact, relevant aerosol optical properties for determining radiative effects are optical depth, single scatter albedo and phase function, which depend on composition, size distribution and shape and therefore vary with wavelength. Furthermore, particles of different origins may have significantly different optical properties [Meloni et al. (2004)]. Recent estimates of the global mean direct radiative forcing by dust range from +0.09 to -0.46Wm^{-2} [Formenti et al. (2003)], and Overpeck et al. (1996) found that Asian dust emission may have contributed to warming of up to 5°C downwind of major source areas.

The indirect aerosol effect is generally credited to Twomey (1977) and assumes that an increase in aerosol concentration will lead to smaller droplet sizes, hence an increase in optical thickness and cloud albedo. Though Twomey discussed only effects on liquid droplets, the idea of decreasing size with increasing aerosol concentrations was recently challenged by Chylek et al. (2006), who observed an 'inverse aerosol indirect effect' where higher aerosol numbers resulted in lower ice crystal concentrations and larger crystal sizes. Although pure mineral dust is not generally considered to be an effective cloud condensation nucleus (CCN), it can serve as an effective ice nucleus, with some clay minerals nucleating at temperatures as warm as -5.2°C [Sassen et al. (2003)].

The semi-direct effect refers to a reduction in relative humidity which follows from aerosol absorption of radiation and subsequent warming of the surrounding air. This has the potential to reduce fractional cloud cover on a regional or global scale, and Johnson et al. (2004) found that the strength of this effect depends only on the absorptive properties

of the aerosol in question. The ability of mineral dust to absorb in the shortwave and longwave, mentioned previously, makes this a potentially-important consideration when large plumes are transported through regions of maritime stratocumulus. For aerosols above the boundary layer, the net forcing is negative and results in less entrainment and a shallow, moist boundary layer and by extension inhibits the potential for convection [Brooks (2000)]. With regards to net radiative effects of suspended mineral dust, Lacis and Mishchenko (1994) found that the overall effect on a regional scale is net cooling, while Myhre et al. (2003) used data from the SHADE campaign to calculate a diurnal radiative impact of Saharan dust of -5 to -6Wm^{-2} and a global mean impact of -0.4Wm^{-2}.

Cloud microphysics are another atmospheric process affected by mineral dust, though, like the radiative impact, the nature and degree of the impact remain highly uncertain. As noted, pure mineral dust is generally an effective ice nucleus (IN) [Sassen (2002), DeMott et al. (2003)] and a poor CCN, depending on composition. There is however an emerging body of research examining the phenomenon of coated dust, whereby an otherwise poor nucleator becomes an effective CCN or giant CCN (GCCN) when it is coated by a soluble substance such as sulfate or sea salt [Fan et al. (2004)]. Estimates as to the proportion of lofted dust that is coated range from 35% to 80% [Levin et al. (2005), Rosenfeld et al. (2001), Falkovich et al. (2001), Trochkine et al. (2003)] and the exact coating mechanism is also in question. Levin et al. (1996) proposed four possible pathways:

(1) Dust is coated in situ by sulfate dissolved in rain.

(2) Given a high enough concentration of dust and sulfate (or sea salt), coating could occur by coagulation. Fan et al. (2004) also explored this avenue, hypothesizing that high levels of pollution increase the cloud scavenging of airborne dust.

(3) The oxidation of SO_2 to SO_3 on the surface of a mineral dust particle could result in a soluble coating.

(4) A cloud droplet that was initially activated by sulfate could collect a dust particle. Since most clouds droplets evaporate without precipitating, the particle is left with a soluble coating. This pathway was also examined in a modeling study by Wurzler et al. (2000) who found that not only was it a viable pathway, but that it resulted in a broadened aerosol spectrum.

The combination of radiative and microphysical effects can obviously affect precipitation as well. As with all other effects of mineral dust, these are relatively poorly understand and subject to great variability, however field and modeling studies continue to contribute to the existing body of knowledge. Rosenfeld et al. (2001) examined satellite and airplane data, finding that when dust was present in marine stratocumulus the effective droplet radius was reduced and warm rain was inhibited. These findings were echoed by Falkovich et al. (2001) who also found that Saharan dust provides a very significant concentration of CCN. Levin et al. (2005) noted that there is still disagreement over whether dust actually increases or supresses precipitation, due to its possible role as CCN, GCCN and IN, all of which may have conflicting effects. The IAPSAG (2006) report on aerosols concluded that for an effective analysis of dust impacts on clouds and precipitation, information on CCN, GCCN and IN characteristics are needed, however no published studies on dust budgets include this information.

Another possible effect of dust is a desertification feedback. Several studies have touched upon this subject and come up with conflicting conclusions: Nicholson (2000) and Rosenfeld et al. (2001) support a positive feedback mechanism due to a reduction in precipitation over dust-producing regions while Miller et al. (2005) found a negative feedback based on a modeling study where local heating in dust layers resulted in increased precipitation, increased evaporation, convection and eventually an increase in localized precipitation over source regions. This study did not consider the indirect effect.

Dust uplift and transport near the surface can also cause a host of problems affecting both nature and humans. Bergametti (1998) showed that dust can be a major source of nutrients for ocean vegetation, while Nickovic et al. (2001) found that desert dust with active iron and phosphorous can cause algal blooms when deposited on the ocean surface. Tang et al. (2003) identify a host of chemical reactions that took place in the presence of mineral dust during ACE-ASIA, noticeably affecting regional chemistry. A study by Prospero (1999) found that African dust transported over Florida during the summer can exceed EPA PM2.5 health standards. Lastly, in light of current military operations in the Middle East, dust has the potential to severely disrupt plans by inhibiting visibility and limiting the use of aircraft and land-based laser guided weaponery, increasing the difficulty of navigation for ground-based soldiers and damaging vehicles and instruments [Kuciauskas et al. (2003)].

1.2   Existing Dust Models

Recognizing the potential importance of mineral dust in the atmosphere, a number of models have begun to include its effects. A multitude of obstacles exist for any dust model: At the most basic level, the lack of detailed soil models [Gong et al. (2003)] and a dearth of observations [Wang et al. (2004)] over land and ocean constrain improvements in dust modeling. This is evidenced by the major discrepancies in dust size distribution predicted by existing models and the failure to align with most observations [IAPSAG (2006)]. Additionally many parameterizations are drawn from wind tunnel studies, and Mahowald et al. (2005) highlight the possible hazards of assuming a direct correlation with real-world behavior. Nevertheless, models continue to appear and evolve along with newer and better observations. The approach, scope and goals of each model vary substantially and many mentioned in this section have additional capabilities including detailed chemical and photolysis schemes, however only mineral dust schemes are covered.

One such model, the TM3, is described by Mahowald et al. (1999). It was used with a very coarse resolution of $4° \times 5°$ in an attempt to model dust loading during the last glacial maximum. Although coarse, it includes emission, advection and deposition. Two more recent models include dust on a global scale, with the goal of modeling the present climate as well as forecasting global emission and transport. The GOCART model described by Ginoux et al. (2001) is the origin of much of the methodology applied to the model in this study [see Chapter 2 for more detail]. It includes a detailed emissions and transport model, with seven size classes and includes both dry and wet deposition, rainout and washout. The GOCART model belongs to a class of models referred to as 'offline', meaning that they ingest meteorological output from a separate model, in this case GEOS DAS, running at a resolution of $2°$ latitude by $2.5°$longitude. A five-year simulation found annual global emissions of 1604-1960 Tgyr^{-1}. Seasonal trends and distribution were reproduced with a fair degree of success however the authors concluded that more detailed soil maps are needed, especially over Asia. The NAAPS model [Tratt et al. (2001)] has been developed by the Navy as another offline model. As with the previous two models, NAAPS is run on a global domain, however it is run fulltime as a forecast model. Meteorological input is via the NOGAPS weather model and resolution is $1° \times 1°$. This model has also been run against a number of Middle-Eastern dust outbreak cases with good success.

Several regional models have been modified or developed in support of field campaigns. The ACE Asia campaign of 2001 involved the use of the STEM2K1, CFORS and NARCM models. The STEM2K1 model [Tang et al. (2003)] is an offline model driven by RAMS output. It was run at 80km resolution for the campaign and includes an explicit dust emission scheme along with a sophisticated chemical module. NARCM [Gong et al. (2003)] is driven by the Canadian Aerosol Module and is somewhat unique in that it incorporates a very detailed soil texture map, something that was mentioned by Ginoux et al. (2001) as being necessary for future improvement of dust emission modeling. NARCM includes

soil emission, transport, growth, coagulation along with wet and dry deposition and was successful at reproducing observations except where model meteorology was incorrect. The CFORS model [Uno et al. (2003)] is unique among this group of models in that it is an online model, that is mineral dust (and other chemical species) are considered along the same time steps as other meteorological variables. However chemical species effects are not fed back into the model. Nevertheless, this model also did well at reproducing observed spatial dust distributions.

Several other models should also be mentioned as they continue to be developed or are pertinent to this study. The RAMS-AROMA model, summarized by Wang et al. (2004), is based on the same version of RAMS 4.3.0 as the present study and incorporates assimilation of GOES8 AOT data. Rather than parameterize the emission of dust, the column AOT data is used to initialize, then nudge dust concentrations. This approach yielded good results when simulating observations from the NASA PRIDE campaign. The Oslo CTM2 model described by Myhre et al. (2003) is driven by ECMWF reanalysis data. It is an offline model, and has been used to examine the radiative impact of Saharan dust transport across the Atlantic during the SHADE campaign. It includes parameterization of dust emission and agreed well with measurements taken from MODIS, AERONET and a C-130 platform.

The DREAM model [Nickovic et al. (2001)] is probably the most similar to the current RAMS development. It is designed as an online model, run off of the SKIRON forecast model, which itself is evolved from the Eta/NCEP forecast model. It includes parameterizations of dust emission along with dry and wet deposition. Currently, mineral dust is not allowed to be radiatively active, and it is transported as a passive tracer however this and microphysical interaction are planned in the future. The DREAM model currently provides 72-hour forecasts for the Meditarranean and Southwest Asian regions.

A number of models have been briefly examined. As mentioned earlier, their structure, parameterizations and intended uses vary widely. The current version of RAMS shares many similarities with the DREAM model in current and planned development, however already includes radiative effects of mineral dust which have been shown by Myhre et al. (2003) and Stokowski (2005) to have a potentially large impact on both the shortwave and longwave radiation balance as well as offering important feedback into the atmosphere.

1.3   Goals of this Study

The goal of this study is to implement a dust emission and deposition scheme within the current RAMS 4.3.0 framework. This will directly complement the work of Stokowski (2005) as mineral dust concentrations will be prognosed rather than prescribed, allowing for a more realistic representation of its impacts on meteorological properties. Model results will be compared with existing models as well as with historical observations, though the latter are somewhat sparse and oftentimes subject to their own error. The use of a model built specifically to operate in the mesoscale has several distinct advantages over many existing models:

(1) The RAMS model has been built specifically to operate effectively through a wide spectrum of domains, from the global down to the LES (Large Eddy Simulation) scale [see Cotton et al. (2003)]. The nesting capability of the model allows for a specific area to be examined in great detail, as opposed to many global models that operate on a fixed grid of 80-100km.

(2) The RAMS dust model is run 'online' and is interactive with other model parameters. This allows for a real-time calculation of radiative effects and a more realistic and timely calculation of dust effects on meteorological variables.

(3) The RAMS runs for this study are initialized and nudged using GFS 6-hourly analysis files [see Chapter 4] however it could equally be run in a real-time configuration

using dust data from an existing global model. This would allow for more detail over global dust hot-spots while still conserving computational efficiency.

The remainder of this paper is organized into eight chapters, each highlighting an important aspect of this study. An effort has been made to compartmentalize each chapter, such that each stands on its own to some extent, with references to other sections and papers should further detail be desired. A conclusion summarizes the model performance during the study and includes a number of recommendations for future improvements.

Chapter   2

THE MODEL

This chapter provides an introduction to the RAMS model in use at Colorado State University. A brief overview of past development is provided along with a summary of more recent work by Stokowski (2005). More time is spent on the newest addition to the model and the focus of this thesis: Section 2.2 discusses the dust emission and deposition schemes that were recently added.

The original configuration of the RAMS model has been available since 1991. This was borne from the convergence of several earlier models: A cloud mesoscale model [Tripoli and Cotton (1982)], an updated hydrostatic version of that model by Tremback (1990) and a sea breeze model by Mahrer and Pielke (1977), all summarized in a paper by Pielke et al. (1992). Some characteristics pertinent to this study are mentioned below, and a more complete description of version 4.3.0 is given by Cotton et al. (2003).

RAMS 4.3.0 is a non-hydrostatic model, using a rotated polar-stereographic horizontal grid, and a staggered Arakawa-C vertical grid. Vertical coordinates are allowed to be either terrain-following or standard Cartesian. Time differencing is done via a hybrid combination, with the calculation of the Exner function done with a leapfrog scheme and all other variables using a forward scheme. The most recent radiation incorporates a two-stream scheme and is described in more detail in Section 2.1. Convective parameterization is done either with the Kuo or Kain-Fritsch methods, with explicit cloud representations

for smaller grid spacings. A soil/vegetation model [LEAF2, Walko et al. (2000)] is used for the lower boundary condition over land, and climatic mean SSTs are used for initialization over ocean areas. At the lateral boundaries, radiation is nudged using a Klemp-Wilhelmson radiative condition [Klemp and Wilhelmson (1978)] and synoptic-scale nudging is done on the boundary, excluding the outermost points, following Davies (1983). A sea-salt emission scheme based on O'Dowd et al. (2003) may be used to simulate concentrations of sea salt, which may also be used as a proxy for GCCN in the model.

Up to four levels of nested grids may be used in the model. Higher resolution in the horizontal and vertical directions may be specified using a nesting ratio. Nested grids may be placed anywhere within their parent grid. See figure 3.2 for an example of a nested setup. RAMS grids are interactive, meaning that model variables are passed from the coarse grid to finer grids and vice-versa. This allows part of the domain to be examined in higher resolution without the computational expense of increasing resolution on the whole domain.

2.1   Radiation and Visibility Scheme

The most recent radiative scheme in the RAMS model is a two-stream model developed by Harrington (1997) and described by Cotton et al. (2003). In this model, the azimuthally-independent radiative transfer equation is integrated and the δ-Eddington approximation is applied to eight radiation bands; three solar and five in the near-IR (see table 2.1). The Harrington scheme accounts for the radiative effects of H_2O, CO_2 and O_3 as well as seven classes of water, specifically cloud droplets, rain, pristine ice, snow, aggregates, graupel and hail. This interaction is accomplished by considering three optical properties: The optical depth (τ), the single-scatter albedo (ω) and the asymmetry parameter (g).

More recently, Stokowski (2005) modified Harrington's scheme to include the effects of sulfates, sea salt and mineral dust. This was done by applying Mie theory under the assumption that the aforementioned aerosols are all smooth spherical scatterers and ab-

Band	1	2	3	4	5	6	7	8
λ_{low}	1.53	0.7	0.245	20.0	12.5	8.33	9.01	4.64
λ_{high}	4.64	1.53	0.7	104.0	20.0	9.01	10.3	8.33

Table 2.1: Radiation bands used in RAMS [μm], from Harrington (1997)

sorbers. Using the median radius of each species as an input, and assuming a lognormal distribution, each species is divided into 17 bins using a 3rd order Lagrangian polynomial interpolation scheme.

Using an offline code ($Equim_5$), three lookup tables (four for sea salt and ammonium sulfate) are generated: The extinction coefficient, the scattering coefficient and the asummetry parameter (as well as a deliquescence growth factor for sea salt and ammonium sulfate). The three former are calculated as functions of radiation band, RH and bin number. Ammonium sulfate is considered as a 90% insoluble mineral dust core with 10% sulfate coating while sea salt has no insoluble core. From these lookup tables, total extinction, total scattering and total forward scattering may be determined for each aerosol species, summed and returned to the main radiation subroutine where the aerosol effects are combined with effects of hydrometeors. Because RAMS radiation bands are very broad, the $Equim_5$ code divided each into 100 bins and the resultant extinction and scattering variables were the arithmetic mean of these sub-bands.

Finally, an isotropic visibility may be determined using the Koschmieder equation,

$$x_v = \frac{3.912}{b_{ext}} \tag{2.1}$$

Where b_{ext} is the extinction coefficient in the visible band. Unfortunately, referring to table 2.1, we can see that no one band corresponds to the visible spectrum. The closest that may be achieved is to consider the Koschmieder equation for band 3, which covers 245-700nm. This introduces an error into the visibility parameter whose magnitude and sign will depend on the exact size distribution and composition of particles contributing to
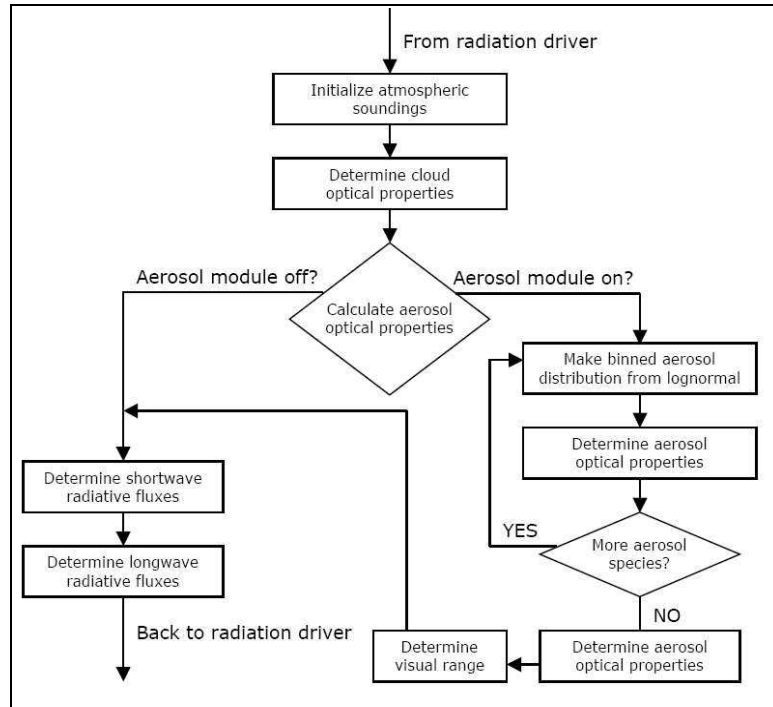
Figure 2.1: Flow Chart for the Harrington radiation scheme, including the new aerosol module. From Stokowski (2005)

the extinction coefficient.

The modified Harrington radiation scheme is shown in figure 2.1. The radiative effects of both dust modes [as presented in Section 2.2.2] as well as sea salt may easily be turned on or off by the user in the RAMSIN control file.

2.2 Dust Emission and Deposition Scheme

The most recent addition to RAMS is a dust emission and deposition scheme. Previously, a user was forced to specify an assumed homogeneous concentration or vertical profile. Now, various parameterizations are applied in order to characterize a vertical flux of dust based on model horizontal wind speed and assumed in-situ particle size and mass

distribution.

2.2.1   Dust Source Function

The probability of dust emission over a given spot on land depends on many factors including soil composition, soil moisture content, vegetative cover and composition and of course wind speed [Prospero (1999)]. Several efforts have been made to characterize global dust sources in the last ten years. Prospero et al (1999) used data from the Total Ozone Mapping Spectrometer (TOMS) to characterize global dust emission sources. The Navy NAAPS model uses a subset of USGS land use types to build a global map of erodible fraction on a $1°\times1°$ grid. This has more recently been augmented by using satellite observations to pinpoint more localized sources of dust. The source function used in RAMS was developed by Ginoux et al. (2001), who took a slightly different approach. They noted that the work of Prospero (1999) consistently showed that dust sources were related to the degree of topographic depression. These areas typically contain an accumulation of fine-particled sediments that are suitable for erosion and transport by winds. Each low-lying basin was assumed to have an area of $10°\times10°$, simplifying calculations but obviously sacrificing resolution. A source function was then defined by the equation

$$S = \left(\frac{z_{max} - z_i}{z_{max} - z_{min}} \right)^5 \tag{2.2}$$

where z_{max} and z_{min} are the maximum and minimum elevations in the surrounding $10°\times10°$ area and z_i is the height of the local grid. The resulting global dust source function showed good agreement with Prospero (1999) and it subsequent use in the GOCART model also showed promise in simulating global dust emission patterns. A map of the source function over the Middle East is shown in figure 2.2.

For the soil characteristics we choose fractions and classes based on Tegen and Fung (1994). Two broad classes of soil are defined; silt and clay. Silt is assumed to constitute

Bin	1	2	3	4	5	6	7
Radius [μm]	0.15	0.265	0.471	0.831	1.5	2.65	4.71
Mass Fraction	0.0009	0.0081	0.0234	0.0676	0.3	0.3	0.3

Table 2.2: Median radius and mass fraction for binned dust source function.

the majority of erodible materials and is assigned 90% of all mass available for lofting, evenly partitioned into three size classes. The remaining 10% is assumed to be clay in the sub-micron range and is partitioned evenly into four size classes, shown in table 2.2.

2.2.2   Parameterization of Emission

As previously mentioned, dust emission depends on a multitude of factors, some of which may be drawn from prognosed model variables and others which must be assumed. To complicate matters, the relationship between emission and parameters such as wind speed is rarely linear [Marticorena and Bergametti (2005)] and in fact no emission occurs below a certain threshold velocity. Marticorena and Bergametti offer a parameterization of this threshold friction velocity (defined as the square root of the ratio of surface stress to air density) based on intrinsic particle characteristics as well as the roughness length of the surface. Cohesion forces between particles also play an important role, such that smaller particles actually have a higher threshold friction velocity. Empirical expressions by Iverson and White (1982) were modified to avoid the necessity of an iterative solution, specifically the Reynolds number was parameterized as

$$Re = aD_p^x + b \tag{2.3}$$

where $a = 1331$, $b = 0.38$ and $x = 1.56$. For dimensional homogeneity, a is given units of cm^{-x}. The following equation then describes the relationship between particle diameter and threshold friction velocity:

$$U_t^*(D_p) = \frac{0.129K}{(1.928(Re)^{0.092} - 1)^{0.5}} \tag{2.4}$$

17
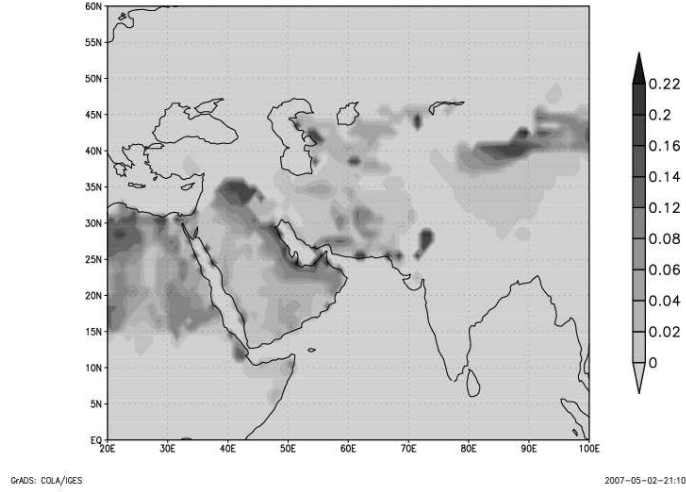
Figure 2.2: Fraction of grid cell acting as a potential dust source

where

$$K = \left(\frac{\rho_p g D_p}{\rho_a} \right)^{0.5} \left(1 + \frac{0.006}{\rho_p g D_p^{2.5}} \right)^{0.5} \tag{2.5}$$

Here, D_p is the particle diameter in $[cm]$, ρ_a is the density of air and ρ_p is the particle density in $[g cm^{-3}]$. A correction is applied to the threshold velocity to account for the effects of soil moisture:

$$U_{twet}^* = U_t^*(1.2 + 0.2 \log w) \tag{2.6}$$

In Equation 2.6, the quantity w is the volumetric soil moisture. A threshold of 0.5 is applied, above which no emission can occur, regardless of the wind speed. In Section 3.2 the sensitivity of dust emission to volumetric soil moisture is examined more closely.

The actual mass emissions are calculated for each size bin and are parameterized by an equation from Gillette and Passi (1988), also used by Ginoux et al. (2001).

$$
F_p = \begin{cases} CSs_p u_{10m}^2 (u_{10m} - u_t) & \text{if } u_{10m} > u_t \\ 0 & \text{otherwise} \end{cases} \tag{2.7}
$$

where C is a scaling factor equal to 1.153 $\mu g s^2 m^{-5}$. This factor scales the global annual emissions to 1851 Tg. The quantity S is the source function described in Section 2.2.1, s_p is the mass fraction of each bin size. The 10m wind speed is interpolated from the lowest model layer wind speed by assuming a logarithmic wind profile.

$$
U(10) = U_{lowest} \frac{ln\left(\frac{10}{z_0}\right)}{ln\left(\frac{dz}{z_0}\right)} \tag{2.8}
$$

where dz and U_{lowest} are the height above ground and wind speed of the lowest model layer and z_0 is the roughness length. Finally, the mass flux in each bin is converted to a number concentration using an assumed density of 2500kgm^{-3} for clay and 2650kgm^{-3} for silt. Sub and super-micron bins are summed into two model variables which are then added to the existing dust concentration and returned to the model. Due to anomalous behavior in the dust emission and advection near grid boundaries, no emission is allowed to occur within three grid points from the grid edge.

2.2.3   Parameterization of Removal Mechanisms

Although there is a quickly-growing segment of research devoted to the role of mineral dust as CCN, GCCN and IN there is no clear consensus, much less a parameterization suitable for inclusion in a mesoscale model. For this reason the only removal mechanisms added in this version of RAMS are gravitational settling and below-cloud scavenging by rain.

Ginoux et al. (2001) estimates that approximately 90% of dust mass is lost to dry, or gravitational deposition while the remaining is lost to some form of in-cloud or below-cloud scavenging. In this version of RAMS a deposition scheme described in Wang et al.

(2006) is modified for use with mineral dust. Because model dust concentrations do not retain information about the binned size described in Section 2.2.2, mean particle radii for the 'small' and 'large' dust categories are used in the sedimentation and washout schemes. These are not straightforward parameters, as the emission scheme described in the previous section results in a threshold friction velocity minimum for particles around $25\mu m$, with a rapid increase for particles smaller that $5\mu m$. A weighted mean of sub- and super-micron bins is inappropriate, but the exact mean radius will vary depending on the assumed in-situ distribution and the model 10m wind speed. Several possible choices were considered, and in the end values weighted toward the larger end of of two modes were chosen: $0.8\mu m$ for the small mode, and $3.50\mu m$ for the large mode.

Dry deposition over water follows the approach of Slinn and Slinn (1980). While Wang et al. (2006) allowed for particle growth in moist environments, this is not allowed in our model, remaining consistent with the radiation scheme in that mineral dust does not undergo moist growth. For all levels above the lowest model layer, fall speed is assumed to equal the terminal fall speed, given by

$$V_g = \frac{\rho_p D_p^2 g C_c}{18\eta} \tag{2.9}$$

from Baron and Willeke (2001), valid for particle Reynolds numbers <0.1. For clay particles of radius 0.8μm and 3.5μm this equation gives fall speeds of 1.8cmh^{-1} and 36.8cmh^{-1} respectively. The slip correction factor and atmospheric viscocity are given by

$$C_c = 1 + \frac{1}{PD_p}\left[15.60 + 7.00exp(-0.059PD_p)\right] \tag{2.10}$$

and

$$\eta = \eta_r \left(\frac{T_r + S}{T + S}\right)\left(\frac{T}{T_r}\right)^{\frac{3}{2}} \tag{2.11}$$

20

where P is the absolute pressure in kPa, D_p is the particle diameter, η_r is a reference viscocity, T_r is a reference temperature and S is the Sutherland interpolation constant.

Two cases are considered for the lowest model layer: Deposition over land and deposition over water. For the more simple case of deposition over water, Equation 2.9 is used as a starting point and the influences of Brownian diffusion and surface characterisitics are are introduced, giving an effective settling velocity described by

$$V_d = \frac{1}{\frac{1}{k_C} + \frac{1}{k_D} - \frac{V_{g_{dry}}}{xkc * xkd}} \tag{2.12}$$

where

$$k_C = V_{g_{dry}} + \frac{1}{1-k} * C_d * U(z) \tag{2.13}$$

accounts for turbulent transfer velocity and

$$k_D = V_{g_{wet}} + \frac{1}{k} * C_d * U(z) * \frac{1}{\sqrt{S_c}} + 10^{\frac{-3}{St}} \tag{2.14}$$

accounts for Brownian diffusion and particle slip.

The drag coefficient C_d, Stokes number St and Schmidt number Sc are given by

$$C_d = 24 * \frac{\eta}{\rho_p * V_{g_{wet}} * D_{p_{wet}}} * (1 + 0.0196 * \rho_p * V_{g_{wet}} * \frac{D_{p_{wet}}}{\eta}) \tag{2.15}$$

$$St = \frac{V_{g_{wet}}}{g} * \frac{u_*^2}{\eta} \tag{2.16}$$

$$Sc = \frac{\eta}{\rho_{air} * Diff} \tag{2.17}$$

The diffusion coefficient is

$$Diff = \frac{k_B * T * C_c}{3 * \pi * \eta * D_p} \tag{2.18}$$

where the Bolzmann constant is $k_B = 1.38 \times 10^{-23}$.

The gravitational deposition over vegetation is taken from an empirical parameterization by Zhang et al. (2000). As with deposition over water, the terminal fall speed in Equation 2.9 is used as a starting point, and the effects of aerodynamic resistance above the canopy and surface resistance are taken into account. Twelve land types and five seasons are defined, including a dedicated classification for snow-covered areas along with accompanying parameters (shown in Zhang et al. (2000), Table 3). The deposition velocity over vegetation is then defined as

$$V_d = V_g + \frac{1}{R_a + R_s} \tag{2.19}$$

where the aerodynamic resistance is

$$R_a = \frac{U(z)}{u_*^2} \tag{2.20}$$

The surface resistance takes into account the efficiencies of Brownian diffusion, impaction and interception. It is given by

$$R_s = \frac{1}{\epsilon_0 u_* (E_B + E_{IM} + E_{IN}) R_1} \tag{2.21}$$

where ϵ_0 is an empirical constant with a value of 3. The Brownian and impaction efficiencies are

$$E_B = Sc^{-\gamma} \tag{2.22}$$

$$E_{IM} = \left(\frac{St}{\alpha + St} \right)^2 \tag{2.23}$$

with the stokes equation being defined by

$$St = \begin{cases} \frac{V_{g_{wet}} u_*}{Ag*1\times 10^{-3}} & \text{if not tundra, desert or ice} \\ \frac{V_{g_{wet}} u_*^2}{\frac{\eta}{\rho_{air}}*g} & \text{otherwise} \end{cases} \qquad (2.24)$$

The interception efficiency is

$$E_{IN} = \frac{1}{2}\left(\frac{D_p}{A}\right)^2 \qquad (2.25)$$

Here, the quantity A is a characterisitic collection radius determined by land type and season and α is a constant, also determined by land type and season. The final quantity to consider is a rebound efficiency R_1. It is defined as

$$R_1 = exp(-\sqrt{St}) \qquad (2.26)$$

The precipitation scavenging rate is calculated for all below-cloud model levels. The Zhang routine orignially included in-cloud scavenging effects, but it was written for use with black carbon, not dust. The large uncertainties associated with the behavior of dust with regards to cloud droplet or ice nucleation led to the decision not to include these effects in the model. Further research is underway to add these effects at a later date. The below-cloud precipitation scavenging rate is parameterized by

$$Scarate = \frac{1}{2}\frac{E_{collect}R_{rain}}{D_{droplet}} \qquad (2.27)$$

The quantity R_{rain} is the rain rate, presently accounting only for liquid precipitation.

The collection efficiency is

$$E_{collect} = \begin{cases} \frac{4}{ReSc}(1+\kappa+A+B)+C & \text{if } St > S_* \\ \frac{St-S_*}{St-S_*-\frac{2}{3}}^{\frac{3}{2}} + \frac{4}{ReSc}(1+\kappa+A+B)+C & \text{otherwise} \end{cases} \qquad (2.28)$$

where

$$A = Re^{\frac{1}{2}}Sc^{\frac{1}{3}} \qquad (2.29)$$

$$B = 0.16Re^{\frac{1}{2}}Sc^{\frac{1}{2}} \qquad (2.30)$$

$$C = 4D_{ratio}(\frac{1}{\eta_{ratio}} + (1 + 2Re^{\frac{1}{2}})D_{ratio}) \qquad (2.31)$$

The quantity S_* is an empirically-determined parameter defined by

$$S_* = \frac{1.2 + \frac{1}{12}\ln(1 + Re)}{1 + \ln(1 + Re)} \qquad (2.32)$$

and other quantities are Sc=Schmidt number, Re=Reynolds number, D_{ratio}=ratio of droplet size to aerosol size, η_{ratio}=ratio between the air and water dynamic viscocities. The precipitation scavenging algorithm is run over every model grid that contains dust and is below a precipitating cloud base. It should be noted that this is only applied to grid points with liquid precipitation. RAMS includes a number of other hydrometeor species including graupel, hail, cloud droplets and snow; these species have no direct effect on dust concentrations in the model.

2.2.4   Summary and limitations of Emission and Removal Mechanisms

The most recent modifications to RAMS have been presented and summarized in this section. These additions are examined more closely in Chapters 3 and 4, however there are some caveats that may be presented here, based on known shortcomings of the methods used.

(1) Microphysical effects of mineral dust are ignored in the present configuration of the model. Numerous studies [Levin et al. (1996), Levin et al. (2005), Rosenfeld et al. (2001), Falkovich et al. (2001), Wurzler et al. (2000), Yin et al. (2002), Vanden-Heever et al. (2006)] have examined the interaction of mineral dust and clouds but

a parameterization suitable for use in a mesoscale model has yet to emerge. Most current studies agree that there is a potentially significant impact of mineral dust either through sulfate coating or as ice nuclei. This omission should be kept in mind for cases where dust may be lofted into cloud layers.

(2) Soil size distributions and compositions are assumed to be homogeneous over all dust-emitting regions. This is also a known oversimplification, as noted by Gong et al. (2003) and Ginoux et al. (2001). The former attempts to characterize dust aerosols over China during the ACE-Asia campaign. This may be a worthwhile modification to the existing scheme if a study is conducted over a specific region with known properties. As a corollary, dust sources are also assumed to be infinite and distributions are not modified over time [Marticorena and Bergametti (2005)]. In this case there is simply not enough information to account for any change in soil properties due to depletion.

(3) The surface roughness length is held constant. Marticorena and Bergametti (2005) note that the roughness length should reflect 'the most frequent state of the surface rather than the integrated effects of the cumulated roughness characteristics.' This is a parameter that may be improved in the future if a high-resolution global surface dataset becomes available and practical to use within the current framework.

(4) Most parameterizations used here were developed using wind tunnel data. In many cases this is not entirely realistic and in fact threshold velocities may differ significantly depending on the parameterization used. They also assume that source regions are composed of loose soils. Areas such as dry lake beds, where soil may be crusted, will not be properly treated. Many factors affecting soil cohesion are also not explicitly treated by this scheme; this may or may not have a large effect on emissions but is worth noting.

(5) The vertical flux parameterization is hampered by inadequate knowledge of local

soil characteristics. As Ginoux et al. (2001) note, complicated vertical flux param-
eterizations are available but are impractical for use in a more generalized model
framework. The equation used in RAMS diagnoses vertical flux based on a crude soil
composition characteristic, wind speed, threshold wind speed and source strength.

(6) Finally, the vertical flux is necessarily scaled to some assumed global emission.
Various estimates for this emission range from 1250 Tgyr^{-1} [Tegen and Fung
(1994)] to 3000 Tgyr^{-1} [Mahowald et al. (1999)]. A change in the scaling factor
will obviously have an effect on the dust emission.

Chapter   3

SENSITIVITY TESTING

This present configuration of RAMS has yet to be tested, therefore it was decided that a series of sensitivity tests should be run before gauging the model's performance against reality. Specifically, the work done by Stokowski (2005) has been tested in an LES configuration, but not in a three-dimensional mesoscale environment. Similarly, the new dust emission and deposition schemes have not been examined at all for their sensitivity to various parameters that may be set by the user in the initial model setup. Three potentially important parameters were identified: The volumetric soil moisture, the vertical stretch ratio and the cell size of a third nested grid. Four output variables were examined for their sensitivity: Total column dust loading, aerosol optical thickness, surface visibility and maximum dust height. Of these, surface visibility is the only parameter that is directly output by RAMS (see Chapter 2 for a complete description of this variable). The others may be calculated during post-processing. These parameters were chosen primarily for later ease of comparison with existing models and observations, which generally output optical thickness and either column or model-layer dust loads.

3.1   The Test Case

For the purposes of sensitivity testing, a date and region where dust emission was known to have occurred was selected. On the morning of 3 May, 2005 satellite images showed large scale dust emission over Saudi Arabia and Eastern Iraq (Figure 3.1). RAMS

NOAA-16 captured imagery of large area of airborne sand and dust blowing from Saudi Arabia into Iraq and over the Persian Gulf. Sandstorms are common in the area and often affect military operations.
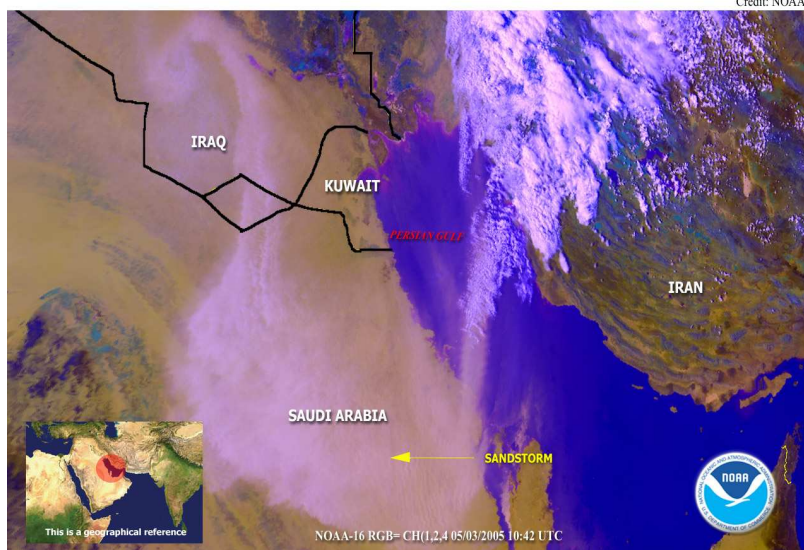
Figure 3.1: Dust plume over Saudi Arabia, 3 May 2005

was set up in a three grid configuration as shown in Figure 3.2. The model was allowed to run for 18 hours, starting at 00Z on May 3rd. The satellite photo shown in Figure 3.1 was taken at 1036UTC and all plots of sensitivity are for the nearest model time of 1030UTC. For this set of runs the visibility parameter (and hence the optical thickness) was set to depend only on dust, sea salt, CCN and GCCN concentrations and omits the influence of cloud droplets and hydrometeros. CCN and GCCN were set to constant vertical profiles so that the magnitude of their influence does not vary with time, or between runs. Four airports, all lying within the 2nd or 3rd grid, were examined for each model run. Their names and locations are given in table 3.1.

Name	Latitude	Longitude
Al Qaysumah	28°19'N	46°07'E
Dharan	26°16'N	50°09'E
Al Ahsa	20°18'N	41°38'E
King Khaled	24°56'N	46°43'E

Table 3.1: Location of Airports used for Sensitivity Testing.

Figure 3.2: Grid setup used for sensitivity testing. Source: www.geographic.org, used with permission.
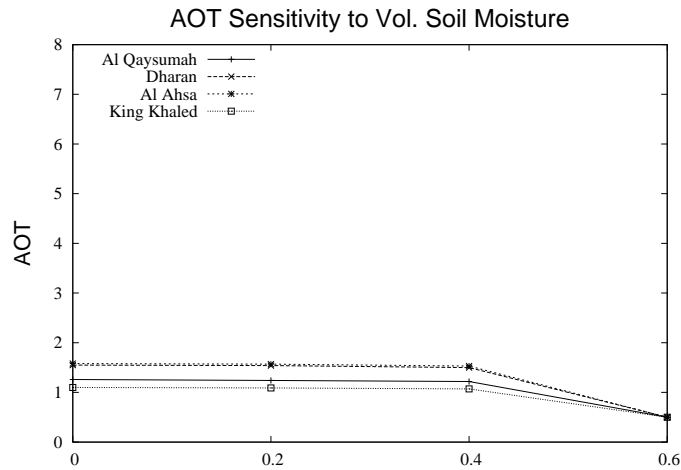
Figure 3.3: AOT sensitivity to volumetric soil moisture

3.2   Volumetric Soil Moisture

The maximum volumetric soil moisture in RAMS depends on the porosity of the specific soil type, but is on average 0.43. An initial value is specified, corresponding to the fraction of the maximum allowed soil moisture. For example a user-specified value of 0.5 would be multiplied by the porosity of the soil type to give an actual volumetric soil moisture. In some cases an intitial value of smaller than 0.25 gave anomalous results and in general most runs outside of the sensitivity testing used an initial value of 0.35 for all soil levels. Values of 0, 0.2, 0.4 and 0.6 were used in order to test both the sensitivity and whether emission is truly inhibited above the designated threshold.

As can be seen in Figures 3.3, 3.4, 3.5, and 3.6 the model shows almost no sensitivity until the threshold volumetric soil moisture fraction (equal to 0.5: Refer to Chapter 2) is reached, at which point dust emission decreases to zero. A future version of RAMS should probably include real-world measured soil moisture rather than a user-designated value, but this does not appear to be of too much concern for the present goal of modeling dust emission and visibility.
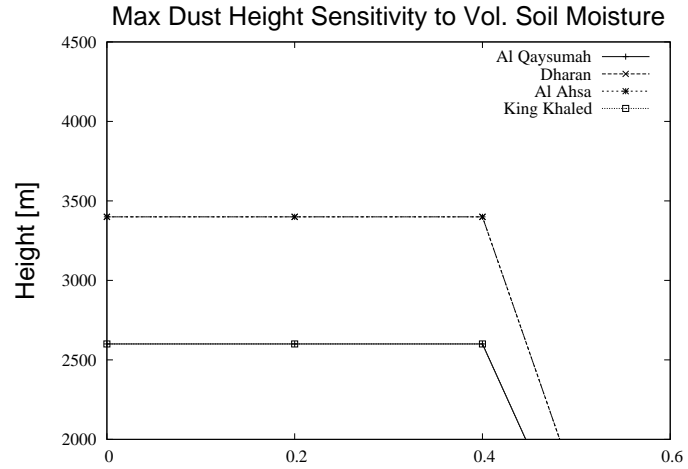
Figure 3.4: Maximum dust height sensitivity to volumetric soil moisture
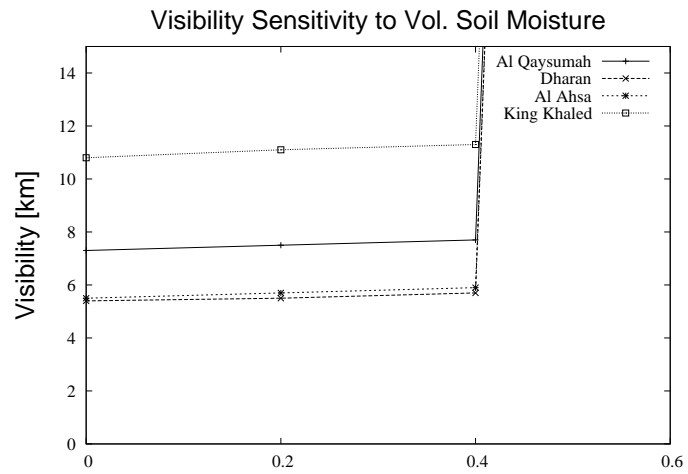
Figure 3.5: Surface visibility sensitivity to volumetric soil moisture
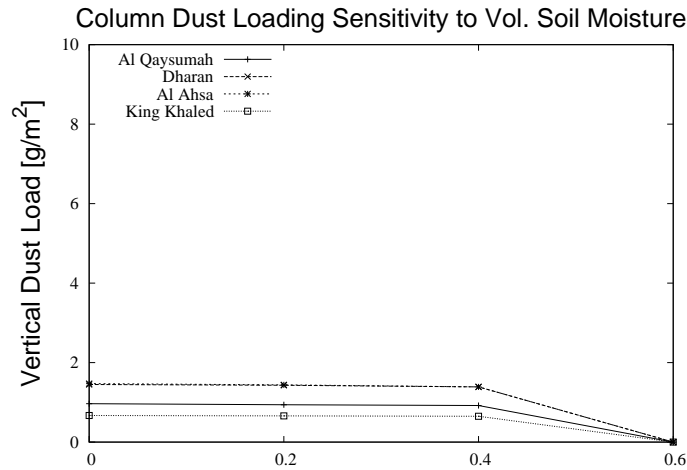
Figure 3.6: Column dust mass sensitivity to volumetric soil moisture

3.3   Grid 3 Cell Size

The cell size in the 3rd nested grid (the smallest) was allowed to vary between 3km and 7.5km while the actual areal extent of the grid remained approximately the same. The goal was to see whether or not a higher-resolution model setup yielded significantly different results than a lower-resolution, computationally cheaper, setup. Note also that although not all stations lie within the 3rd grid, the two-way interactive nature of nested grids makes their response relevant to this portion of the sensitivity testing.

Figure 3.7 shows the AOT sensitivity to grid 3 cell size: With the exception of King Khaled airport, there is almost no response to the size of the grid over the range of tested values. Unlike the AOT, the maximum dust height shown in Figure 3.8 shows a noticeable response to changes in cell size. There is however no clear trend in the response and it should be noted that vertical resolution at this altitude is on the order of 450m, so the difference in many cases represents only one vertical grid cell. This in itself may have implications to the total column dust load since every model grid must by design contain a homogeneous concentration of dust.

The response of surface visibility is shown in Figure 3.9.   As was the case with
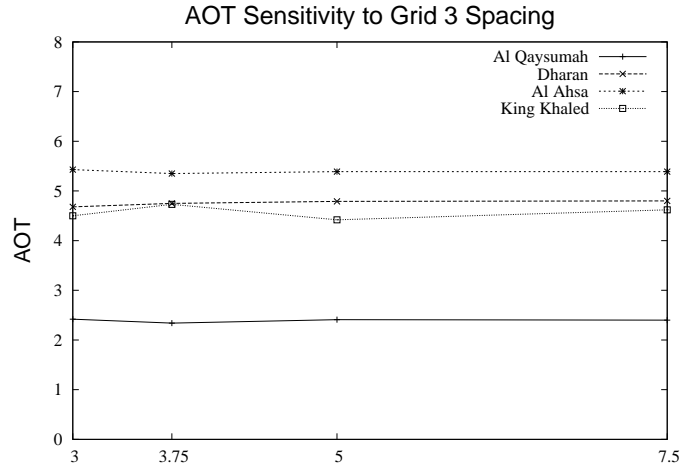
Figure 3.7: AOT sensitivity to grid 3 cell size
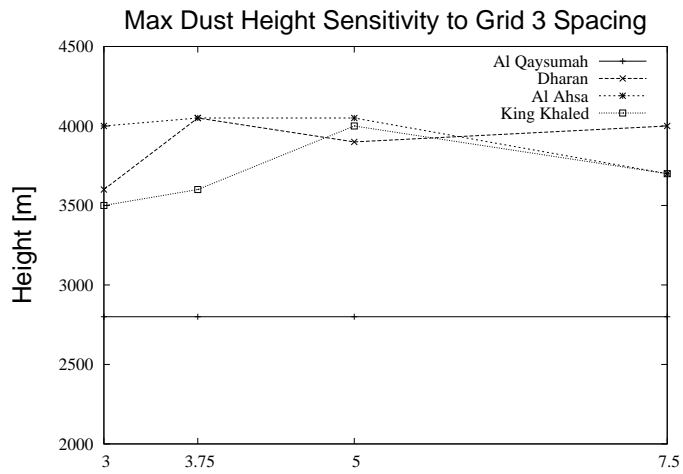
Figure 3.8: Maximum dust height sensitivity to grid 3 cell size
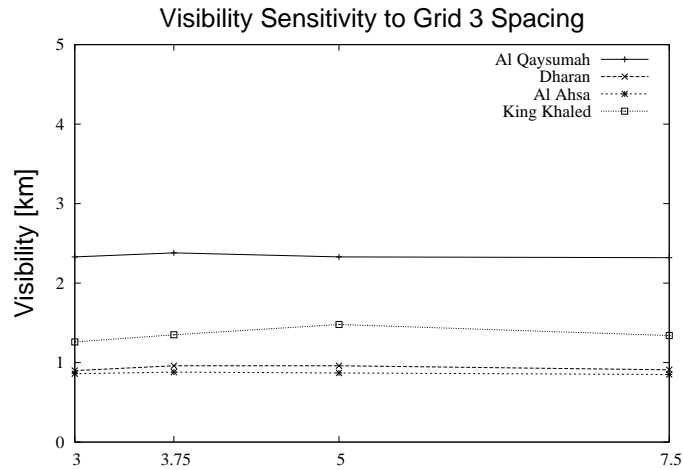
Figure 3.9: Surface visibility sensitivity to grid 3 cell size

maximum dust height, there is no clear trend visibile, with some stations showing increased visibility with increasing cell size, some showing decreasing visibility and some showing no trend at all. Once again, the 'correct' choice likely depends on whether this parameter is tuned to a specific case. Finally, the response of total vertical dust load is given in Figure 3.10. Almost no response is observable at any station. This serves to alleviate some concerns regarding the use of coarse vertical resolution however the stretching parameter will still be examined in Section 3.4. With regards to the effects of grid 3 cell size on total column dust loading, we can conclude that it is of little significance.

From these results we may conclude that over the range of values tested, the resolution of the 3rd grid is not important to the results. This is not to say that model resolution is not important, however given that the source function is only given on a $1° \times 1°$ grid, this should not come as a great surprise. Further improvements in regional dust emission resolution will require a return to these sensitivity tests as some parameters may become more important to the model results.
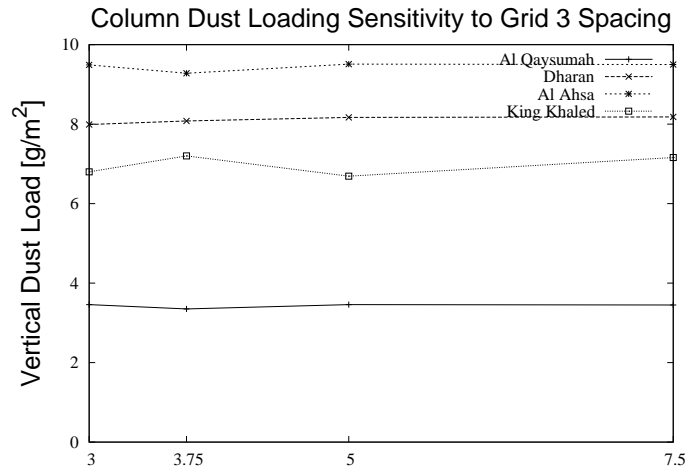
Figure 3.10: Column Dust Mass sensitivity to grid 3 cell size

3.4   Vertical Stretch Ratio

The vertical structure in the RAMS model may either be explicitely defined via an array of physical heights, or alternatively through the use of a vertical stretching ratio. When using the latter method, the thickness of the lowest level is given, followed by a stretching ratio and, if desired, a maximum thickness. The layer thickness thus increases geometrically with height until the maximum thickness is reached, at which point it becomes constant. In this manner a higher resolution may be specified closer to the ground where it is needed, and a coarser resolution higher up in order to save on computational expense. For sensitivity testing, the lowest level layer was set to 90m and the stretching ratio was iterated through values of 1.05, 1.08, 1.10 and 1.12. We could hypothesize that because each grid is assumed to hold a homogeneous concentration of dust particles, that articially-high atmospheric dust loading might be avoided by having a fine vertical resolution close to the ground.

The AOT sensitivity is shown in Figure 3.11. There is a very strong response when the stretching ratio is increased from 1.05 to 1.08, and a further positive response, though less marked for the remaining three values. The one exception is King Khaled airport, where

35
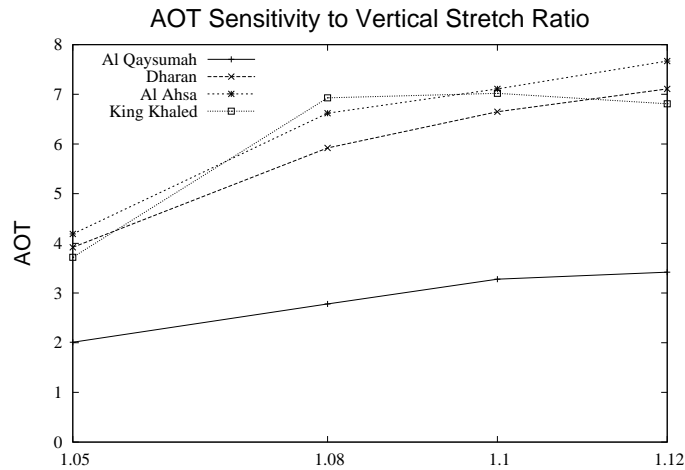
Figure 3.11: AOT sensitivity to vertical stretch ratio

there is actually a slight decrease in AOT between ratios of 1.10 and 1.12. The maximum height reached by the dust layer is shown Figure 3.12. As was the case with AOT, there is a mostly positive correlation between dust height and stretching ratio.

The surface visibility obviously doesn't describe the state of dust in the whole atmosphere, but is worthwhile examining because of its effect on many day-to-day activities. Figure 3.13 shows yet another fairly dramatic response when the ratio is increased from 1.05 to 1.08, and a noticeable, though less dramatic response between the remaining three values. At Dharan and Al Ahsa the visibility is halved over this interval. In the cases of Ryadh and King Khaled there is actually a minute increase in visibility when the ratio is increased from 1.10 to 1.12. It might not intuitively make sense that the lowest model layer should be affected by a finer structure, but this allows dust to loft upwards and out of the lowest several layers more easily, decreasing the chance of sedimentation back into the surface layer. This is simply one possible explanation for increased visibility with finer structure. Based on the response of the other parameters, column dust loading in Figure 3.14 should also increase with increasing stretch ratio. Not surprisingly, this is true, but what is slightly unexpected is the decreased magnitude of the response. One possible
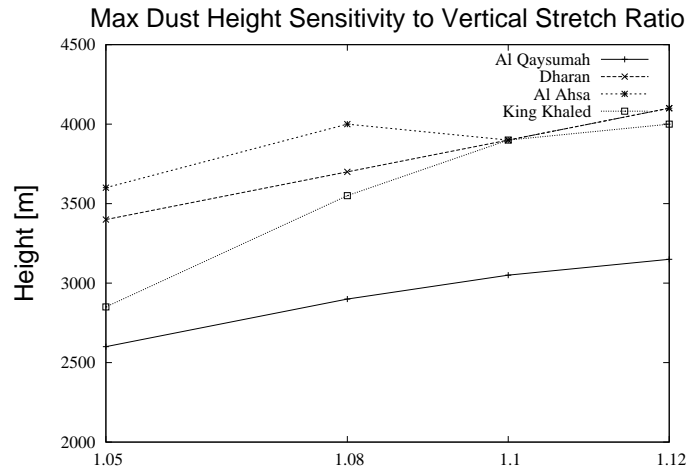
Figure 3.12: Maximum dust height sensitivity to vertical stretch ratio

explanation is that more small particles are lofted to higher levels, generating an increase in AOT but a less dramatic increase in vertical column loading.

Regardless of the specific explanation for each parameter's response, it seems obvious that the vertical structure of the model atmosphere plays an important role in the concentration and distribution of dust and therefore in other quantities such as AOT and visibility. This must be weighed carefully along with other factors such as available computational resources when deciding on the model setup.

3.5   Conclusions on Model Sensitivity

In this section we have examined three user-specified parameters that have the potential to impact the model results. It was found that volumetric soil moisture has very little impact below the cutoff point for emissions. This is good since at the moment, RAMS does not assimilate soil moisture at the beginning of the run and an assumption must be made about the beginning volumetric content. The resolution of a fine grid was also tested and once again, dust concentration and related parameters, both within and and outside of the smallest grid, were found to be relatively insensitive to changes in cell size. Finally the
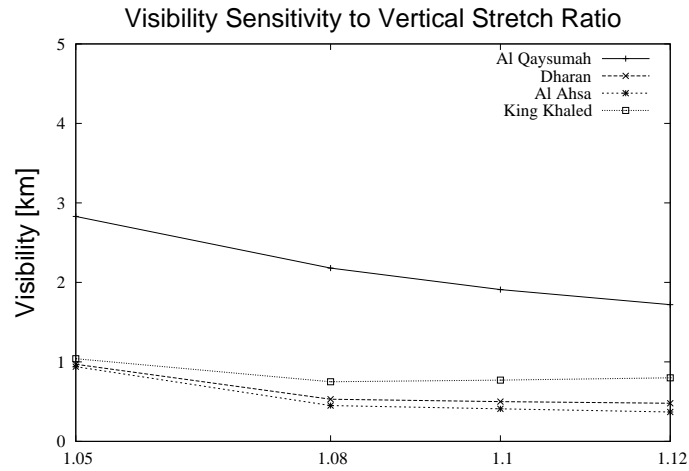
Figure 3.13: Surface visibility sensitivity to vertical stretch ratio
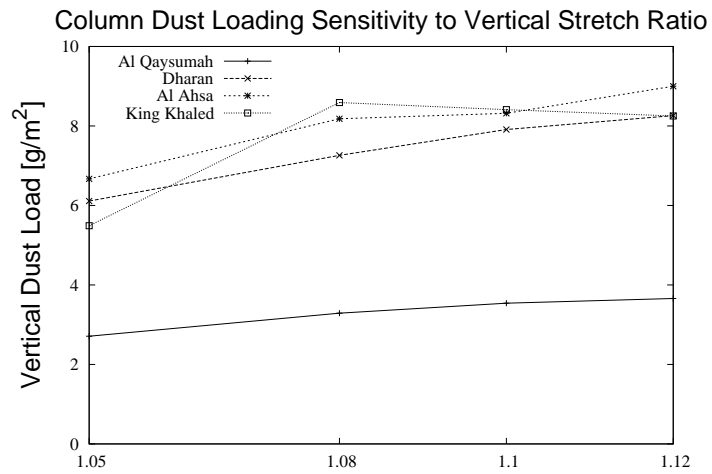
Figure 3.14: Column Dust Mass sensitivity to vertical stretch ratio

vertical stretching ratio was manipulated to test the need for higher resolution close to the surface. Of the three parameters tested this had the greatest effect on model results. Since the effects of dust load will also carry over into the model radiation, careful consideration should be given to the vertical configuration. Also, since dust concentration is assumed homogeneous in every model grid cell, a higher resolution may avoid potential problems of overestimation.

Chapter   4

CASE STUDIES

In the next four Chapters three major Middle-Eastern dust events along with one Sahara-Sahel event are modeled. Each case is examined for its replication of observed meteorology as well as its success in modeling visibility and optical thickness. The results from these cases will allow conclusions to be drawn as to recommended additions or modifications to the dust emission code, as well as the radiation code described by Stokowski (2005).

4.1   General Model Setup

As was mentioned in Chapter 2, RAMS 4.3.0 may be run in a wide variety of configurations. This section will list the choices for some of the variables that were left unchanged for all case study runs. Specifics such as spatial and temporal domain will be listed in the description of each individual case.

During the sensitivity testing detailed in Chapter 3, it was noted that there is little or no benefit to running with a third nested grid given the present surface and dust source models. It is likely that future improvements will make this a more desireable option, but for the present study, only two grids were used. The largest grid (Grid 1) has a grid spacing of 40km and encompasses an area of approximately 25° latitude by 30° longitude, placed such that pertinent meteorological features could be resolved. The smaller grid (Grid 2) measured approximately 8° latitude by 8° longitude and was placed over the area of greatest interest, usually the area with the most stations reporting low visibility due to

suspended dust. Grid spacing in this grid was 10km. All runs used 35 levels in the vertical, corresponding to 150m spacing up to 900m, with gradually increasing thickness up to the model top at 19191m, or approximately 60hPa. This spacing was chosen as a compromise between the need for higher resolution at lower levels, and the instability exhibited in some earlier runs where shallower layers were specified. Timesteps are 45s and 15s for grids 1 and 2, respectively.

All runs use the level 3 microphysics scheme, meaning that all hydrometeor species were prognosed. The modified Harrington radiation scheme described by Stokowski (2005) was used, updated every 15 minutes. The CCN were intialized with a homogeneous concentration of 500cm^{-3}, decreasing to 100cm^{-3} above 4km and with a median radius of 0.04μm. The GCCN were initialized in a similar manner, with a surface concentration of 0.1cm^{-3}, decreasing to 1×10^{-5}cm^{-3} above 4km and with a median radius of 3μm. These values were chosen as they are realistic as far as what may be seen in the atmosphere, and similar parameters were found by Stokowski to have negligible influence on the moisture profile or radiation stream, facilitating the observation of mineral dust effects. The LEAF2 soil and vegetation model was activated and Kain-Fritsch convective parameterization was used in both grids. Parameterization is needed as both grids are too coarse to be able to explicitely resolve convection.

Initialization presented some problems as initially the NCEP global reanalysis, with a resolution of 2.5°× 2.5° in the horizontal, was used to initialize and nudge the model. Unfortunately the coarse resolution meant that crucial frontal features were not adequately resolved, and this proved inappropriate for use in this study. Instead, 1°×1° GFS 0-hour analysis data were used to initialize each run and nudge the model at 6 hour intervals. The disadvantage to this choice is that the input data are perhaps less reliable than an equivalent NCEP reanalysis product, however the increase in resolution was crucial for this study. Every run was allowed a 6-hour spinup before any data were analyzed.

Cases are named using the convention 'XXYYYYMMDD', where XX is a two-letter designation for the country or field campaign, YYYY is the year, MM is the month and DD is the day of interest. A number of cases were examined for inclusion in this study, and in the end four were chosen for inclusion based on availability of verification data, significant dust emission and the assumed absence of anomalously high concentrations of anthropogenic aerosols such as smoke and sulfates.

4.2   Validation Data

As has been mentioned, the paucity of dust measurements increases the difficulty of validating model output. Model performance close to the surface can be evaluated based on reported visibility and other more traditional variables such as temperature, assuming that enough dust is present to affect it. Total suspended aerosol may be evaluated with satellite or ground-based optical thickness data, however this does not validate the model's vertical dust profile, only the total suspended aerosol. Care must also be taken to avoid cases where large quantities of smoke or sulfate aerosols are present, as RAMS does not account for these and observations would be skewed from what would be expected if only dust was present. Several types of data were used for validation: For meteorological verification, NCEP reanalysis data are used. These are valuable because they integrate model output with observations to give the best available picture of the true state of the atmosphere. These are available four times daily at 00Z, 06Z, 12Z and 18Z. Surface conditions are further verified using NWS ADP visibility-reducing weather plots, which include the usual wind and current weather as well as horizontal visibility. Optical thickness verification is done using Aeronet (Aerosol Robotic Network) data. Case SH20000924 is also tested against vertical dust profiles measured by the UK MET C-130 during the Saharan Dust Experiment (SHADE).

Metrics for success or failure are difficult to define, as many of the comparisons in

the following chapters examine only the qualitative, for instance the horizontal areal extent of lofted dust. Similarly, pressure fields and precipitation observations are compared with model output to expose any systematic errors that may impact dust predictions. Nevertheless, each chaper does include some quantitative comparisons of surface visibility and optical thickness. It is important to note that the optical thickness for Aeronet and RAMS includes both clouds and precipitation. A cloud-screened Aeronet product is available however this eliminates well over 50% of the data. The overriding intent of the analysis that follows is to judge the new dust module in a qualitative sense and to identify avenues for further refinement.

Chapter   5

CASE IR20030326

This case is one of several relatively recent dust storms in the Middle East. There has been increased interest in this area in the last several years, due partly to frequent widespread dust storms and also because of military operations in the region. The three-day period was chosen by examining surface plots and noting the incidences of suspended dust accompanied by low surface visibility. In this case sporadic outbreaks were seen on 24 March, with the most widespread and severe outbreak occuring through 25 and 26 March. For this reason the model was started at 12z on 24 March and run through 12z on 27 March. The first six hours were discarded to allow for model spinup, so the actual period of analysis extends from 18z 24 March through 12z 27 March. The largest grid extends from approximately 31°E to 63°E and 10°N to 42°N while grid 2 covers 43°E to 50°E and 25°N to 30°N. Its location was chosen as a compromise between areas of high dust emissivity and periods of very low reported visibility.

5.1   Meteorology

This section provides a brief look at the synoptic conditions affecting the region of interest during IR20030326. The progression of 1000-500mb thickness as well as surface wind speed is presented in order to better understand the effects on dust mobilization. In addition, several soundings are compared to model conditions in an effort to find areas where inaccurate model meteorology may affect the eventual simulation of surface visibility,
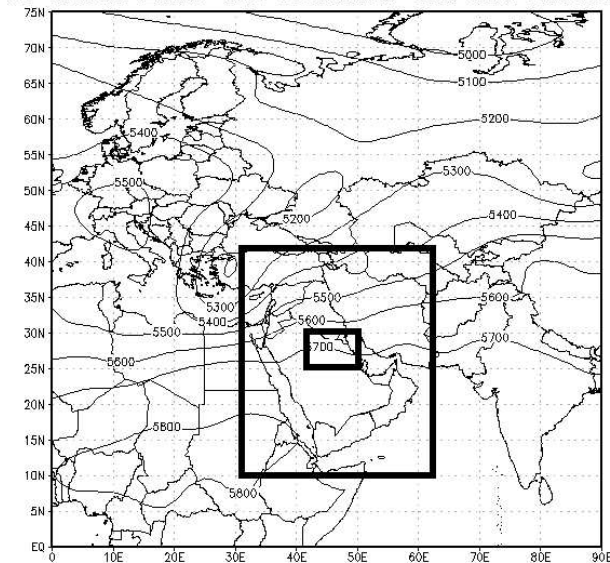
Figure 5.1: Initial Conditions for run IR20030326 12z March 24, and location of Grids 1 and 2

atmospheric dust load and optical thickness. Slightly more space is devoted to examining the meteorology for this case than for other cases. A plot of the initial conditions used for this model run is shown, superimposed with both model grids, in Figure 5.1. A low pressure system is visible over the Eastern Meditarranean, with the flow in the lower atmosphere being generally westerly.

Figures 5.2 and 5.3 show the progression of the 1000-500mb thickness as well as surface wind speed throughout the modeling period. The low pressure system seen in Figure 5.1 can be seen to progress across the model domain in a westerly direction, eventually weakening and dissipating through 26 March. Surface wind speeds over the strongest dust-producing regions adjacent to the Persian Gulf are relatively strong throughout most of 25 March, increasing to $15 \mathrm{ms}^{-1}$ in midafternoon before weakening in the early morning on 26 March. (refer to Figure 2.2 for a map of dust source strength).

The correct resolution of precipitation with the model is one very important factor in
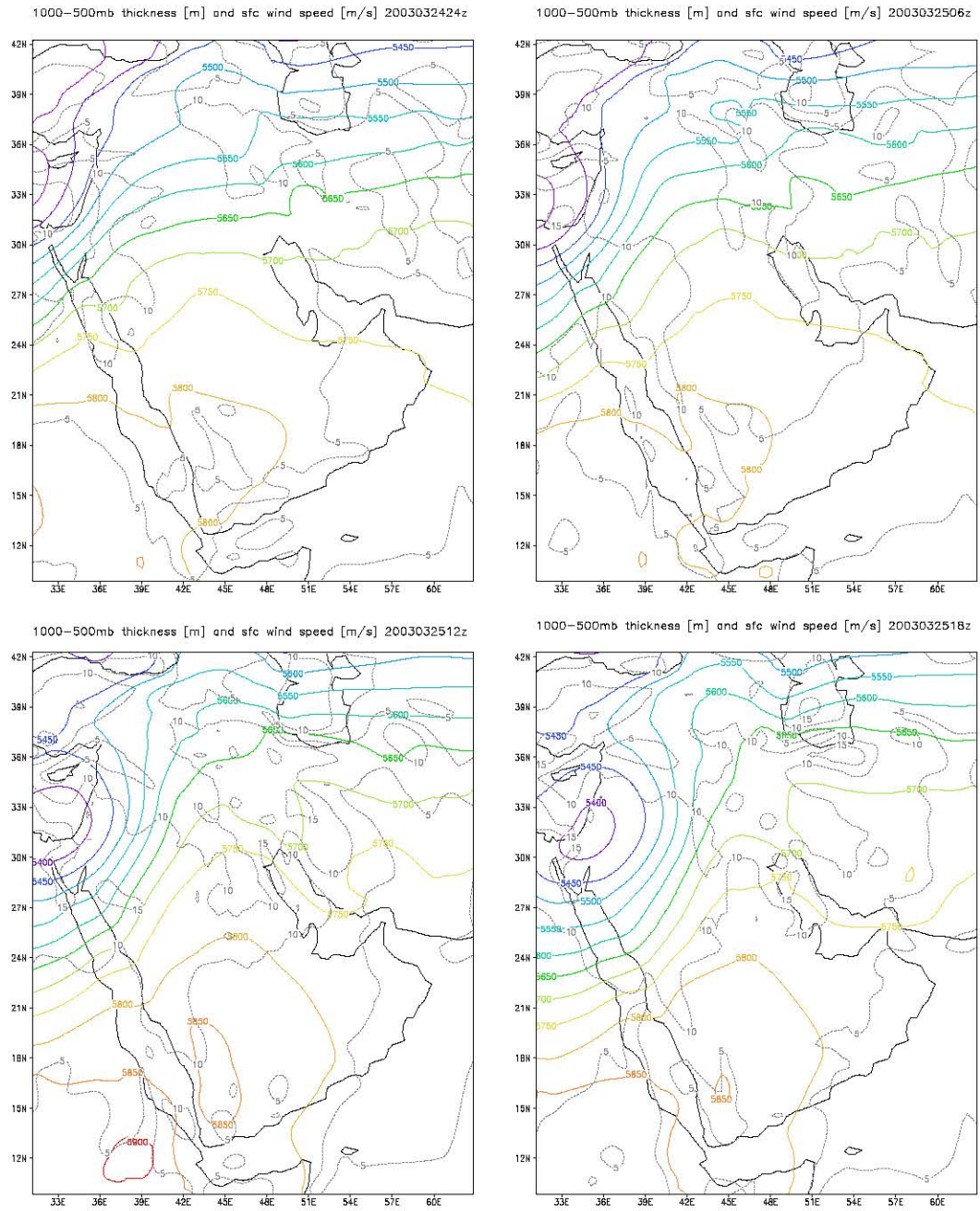
Figure 5.2: 1000-500mb thickness [m] and surface wind speed for the period 00Z to 18Z, 25 March, 6 hour time step. Temporal progression is left to right, top to bottom.
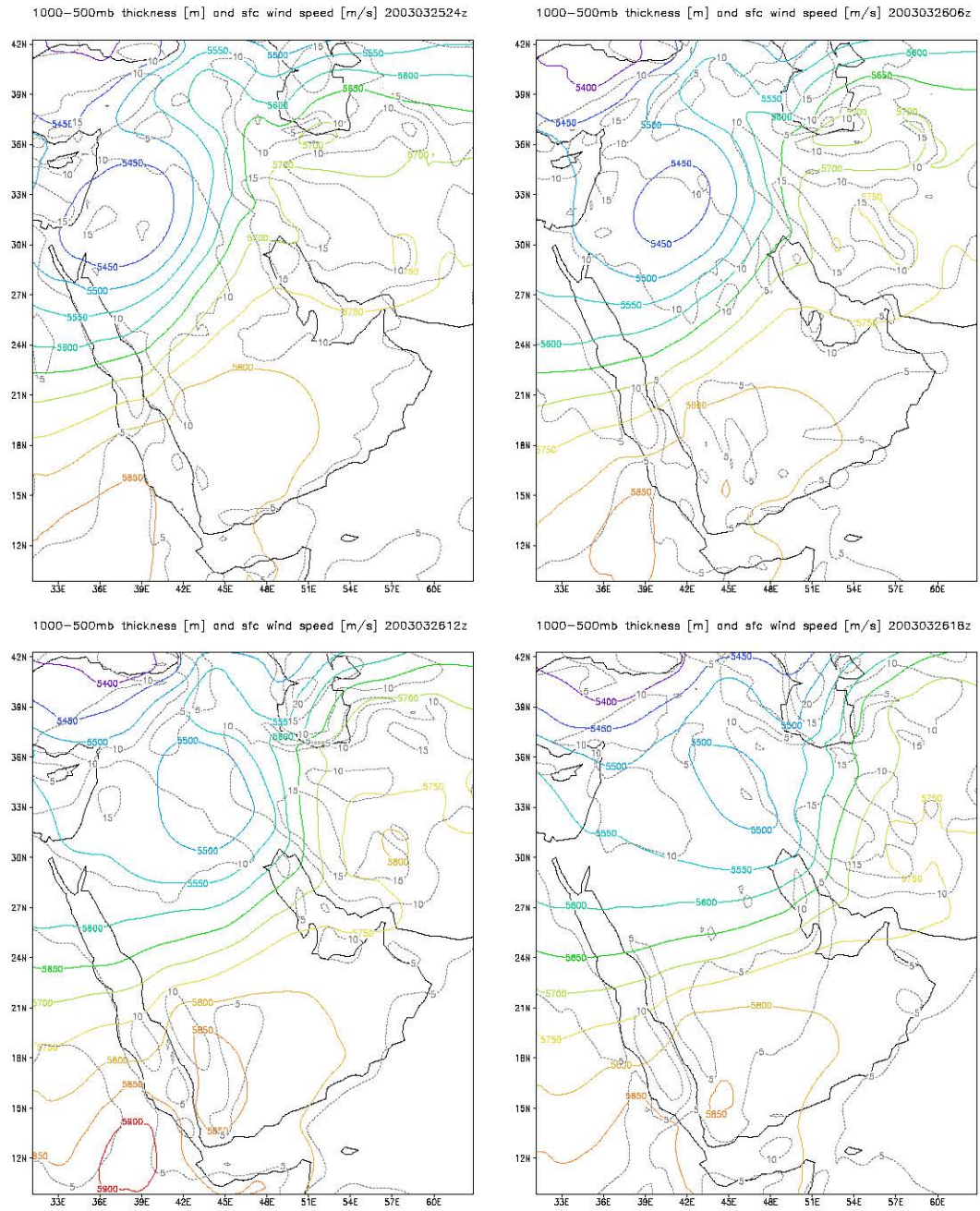
Figure 5.3: 1000-500mb thickness [m] and surface wind speed for the period 00Z to 18Z, 26 March, 6 hour time step. Temporal progression is left to right, top to bottom.

the accurate modeling of dust and its attendant effects on visibility, radiative balance and atmosphere optical thickness. Grid 2 for this case, and all other cases, was tested using no convective parameterization, and also using the Kuo parameterization. Both of these configurations resulted in a gross underestimation of the horizontal extent of precipitation. The use of the KF convective parameterization gave maximum vertical velocities of 0.7ms^{-1} and 2.0^{-1} in grids one and two respectively. It should be noted that the precipitation discussed in this section accounts only for the liquid rain rate, and not snow, hail or graupel. This is because only rain influences dust concentrations in the model and it is more instructive for a critique of model performance.

Figure 5.4 shows the precipitation rate for the period spanning 09z 25 March through 09z 26 March. Prior to this time, a wide area of precipitation develops over Iraq and Syria, agreeing at least qualitatively with surface reports. By 09z, precipitation has developed into a more classic frontal band, arcing through Syria, Northern Iraq and Western Iran. It intensifies throughout the day while moving slowly Eastward and by early morning 26 March has become more fragmented and weak, with the most intense precipitation situated over West-Central Iran. Correlation with surface reports is quite good up until 00z, when the model shows only light amounts while stations in Syria continue to report thunderstorms. There are no surface reports over Iraq for this period so no definitive conclusion can be drawn regarding RAMS performance in simulating precipitation but results are positive in a qualitative sense.

Finally, several soundings are compared with model conditions to verify the accurate reproduction of the vertical structure of the atmoshere. Several features should be examined for their potential impact on dust emissions and transport: Wind speed and direction are of obvious importance not only at the surface, but at upper levels for longer-range transport. Likewise, the temperature and dewpoint will help to determine the initiation and strength of convection. Conversely, the presence and strength of nighttime inversions will suppress
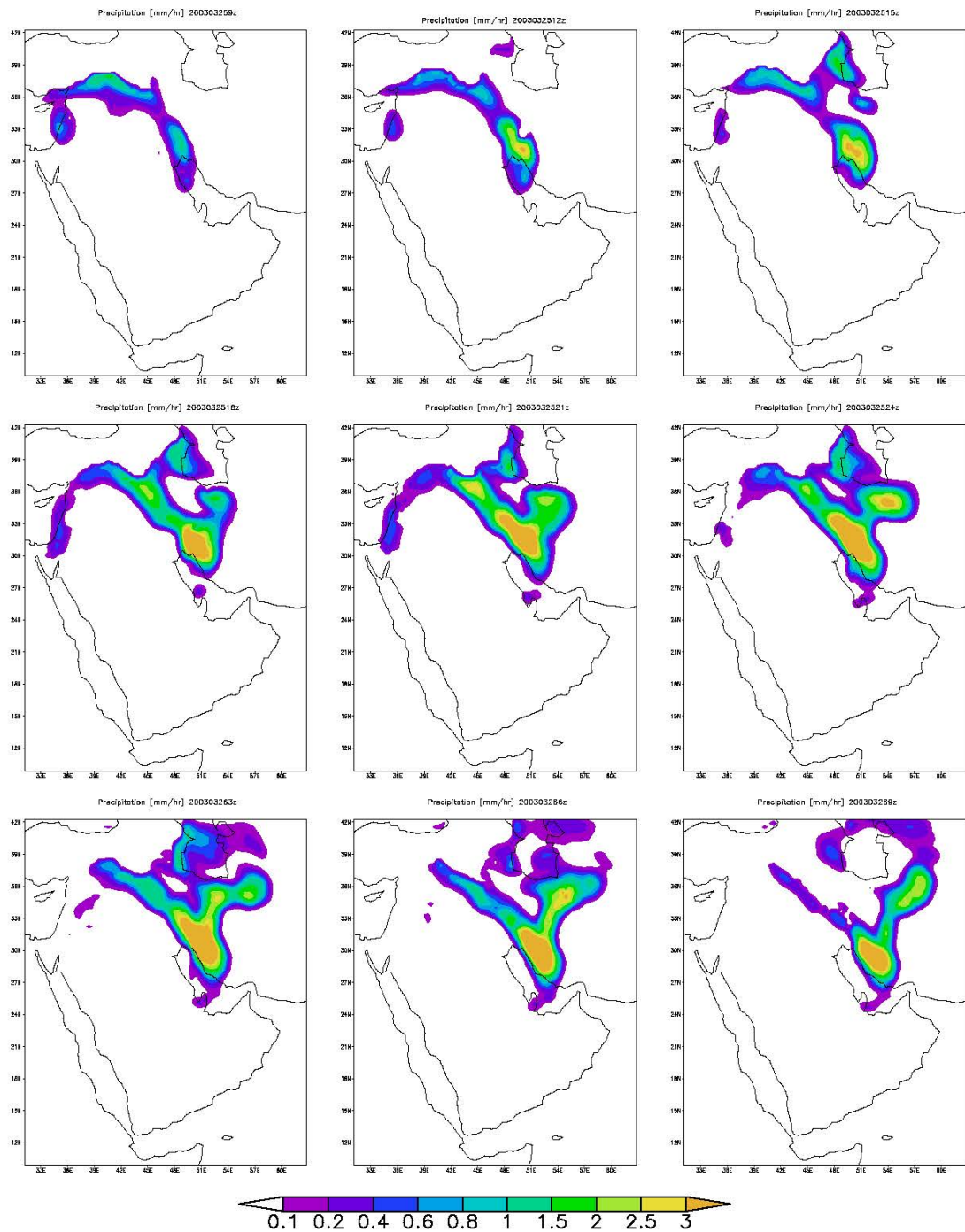
Figure 5.4: Surface precipitation rate [mm/hr] for the period 09Z 25 March through 09Z 26 March, 3 hour time step. Temporal progression is left to right, top to bottom.

vertical transport and the injection of dust to higher altitudes. The decoupling of the boundary layer is also an important feature for the model to capture, as it will usually result in much lighter winds and less dust emission. A selection of RAOB skewT diagrams are compared here with RAMS output in order to evaluate model skill.

Two stations are examined in some detail; Riyadh, situated at 24.9°N,46.7°E and Kuwait International airport at 29.2°N,47.9°E. These are both situated in prime locations for dust generation, and it is reasonable to assume that model replication of observed atmospheric conditions at these locations is of some importance to the accurate modeling of dust generation and injection into the upper atmosphere.

Riyadh is situated outside of the smaller nested grid, and plots here are from the coarse (40km) grid 1. As was mentioned above, large scale features were accurately reproduced during this run, but smaller features such as inversions and localized wind direction and speed are also important. Figure 5.5 presents four pairs of soundings. In the left hand column are the observations, while the right hand column contains the modeled vertical structure. One feature is immediately evident: The model dewpoints indicate a persistent and significant dry bias. This is a problem not only at this point, but at all stations that fall within the model domain. Several factors may play a part in this discrepancy. Because RAMS is initialized and nudged at the outer boundary with data from the GFS model, it is possible that erroneous values are being fed into it, however an examination of GFS data reveals that while not 100% accurate, it is much closer to reality than RAMS. Another possibility is that RAMS does a poor job of simulating evaporation and moisture transport, however many modeling studies [see Cotton et al. (2003) for a selection] have shown that RAMS generally does well handling moisture. A third possibility is that sufficient moisture is not being introduced into the model. Although boundary nudging should overcome this, it is possible that the inclusion of the Eastern Meditarranean in the model domain could alleviate the discrepancies. This last possibility seems the most likely hypothesis, however

it was not tested. Despite this shortcoming some frontal precipitation was still allowed to develop, leading to the possibility that, in this case at least, it is not a major problem.

Poor simulation of dewpoint aside, the model atmosphere at Riyadh closely approximates the observed conditions. Wind veering near the surface is captured at 00z 25 March and a near-adiabatic lower atmosphere is reproduced at 12z. Strong backing is missed at 00z 27 March as is a weak inversion however wind speed and direction are for the most part faithfully reproduced, as is the temperature profile.

Kuwait International Airport falls within the higher resolution 2nd grid. As was done with Riyadh, four plots are shown side-by-side in Figure 5.6. Here too, the poor reproduction of the dewpoint is very evident. Temperature profiles are well duplicated, as are wind speed and wind direction. A strong inversion is captured at 00z on the 25th while inversions at other times are evident, though slightly weaker than observations.

Overall, with the exception of dewpoint profiles, meteorological variables are modeled accurately by RAMS, including boundary-layer wind speed and direction, which are crucial to regulating the emission of dust and its introduction higher into the atmosphere. The next section will focus on model results for dust and visibility.

5.2   Model Dust Results

This section will examine dust and visibility parameters as output by RAMS for this case. Results will also be compared with available observations, including National Weather Service Automated Data Processing [ADP] surface plots and Aeronet time series data. Constraints of the printed page restrict the amount of data that may be presented, so two times were chosen to be examined in some detail based on the extent and severity of dust and restricted visibility reports. The only case-wide parameter that is examined is the optical thickness at the Aeronet Solar Village site.
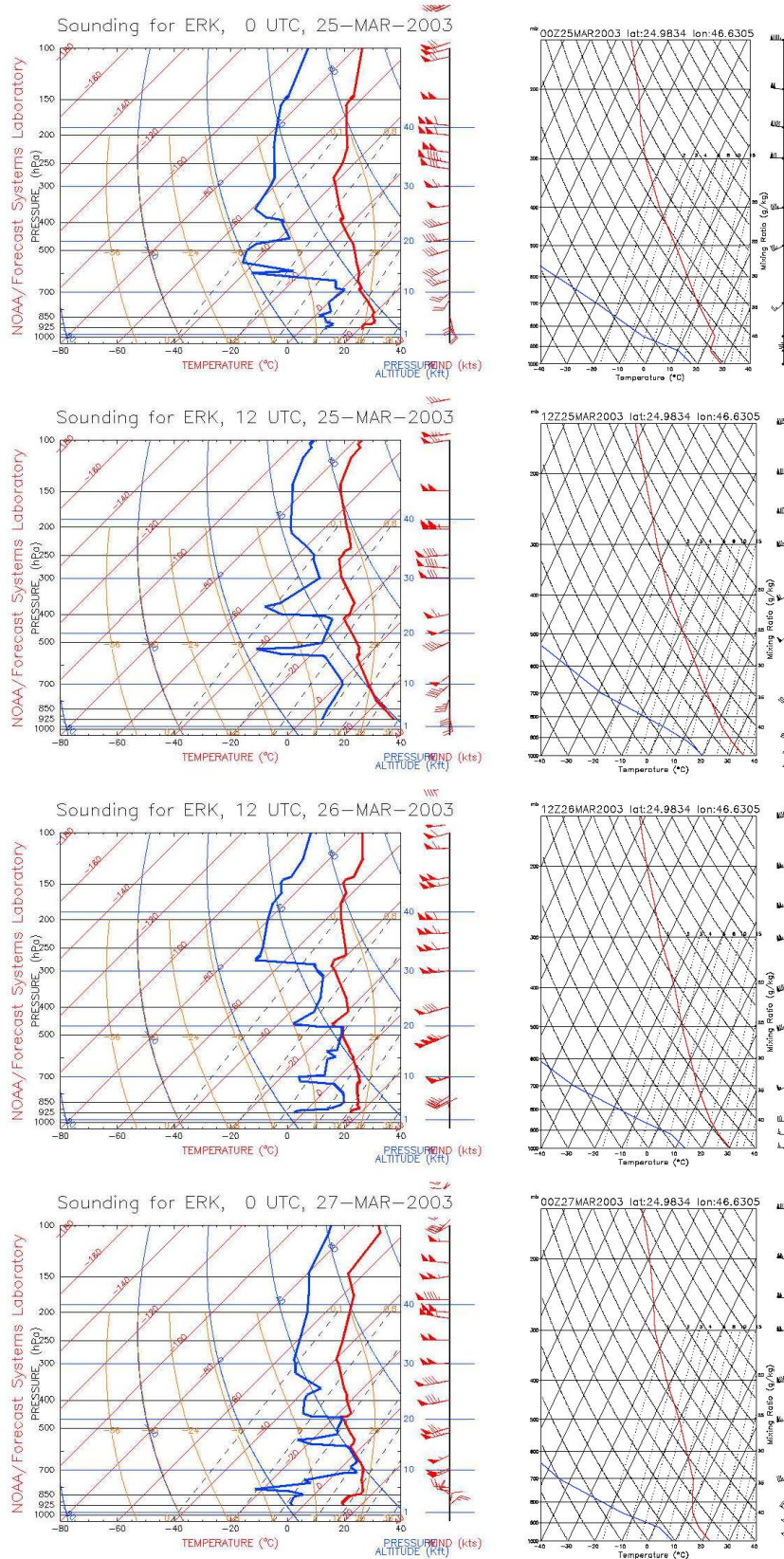
Figure 5.5: RAOB soundings vs. RAMS modeled conditions at Riyadh
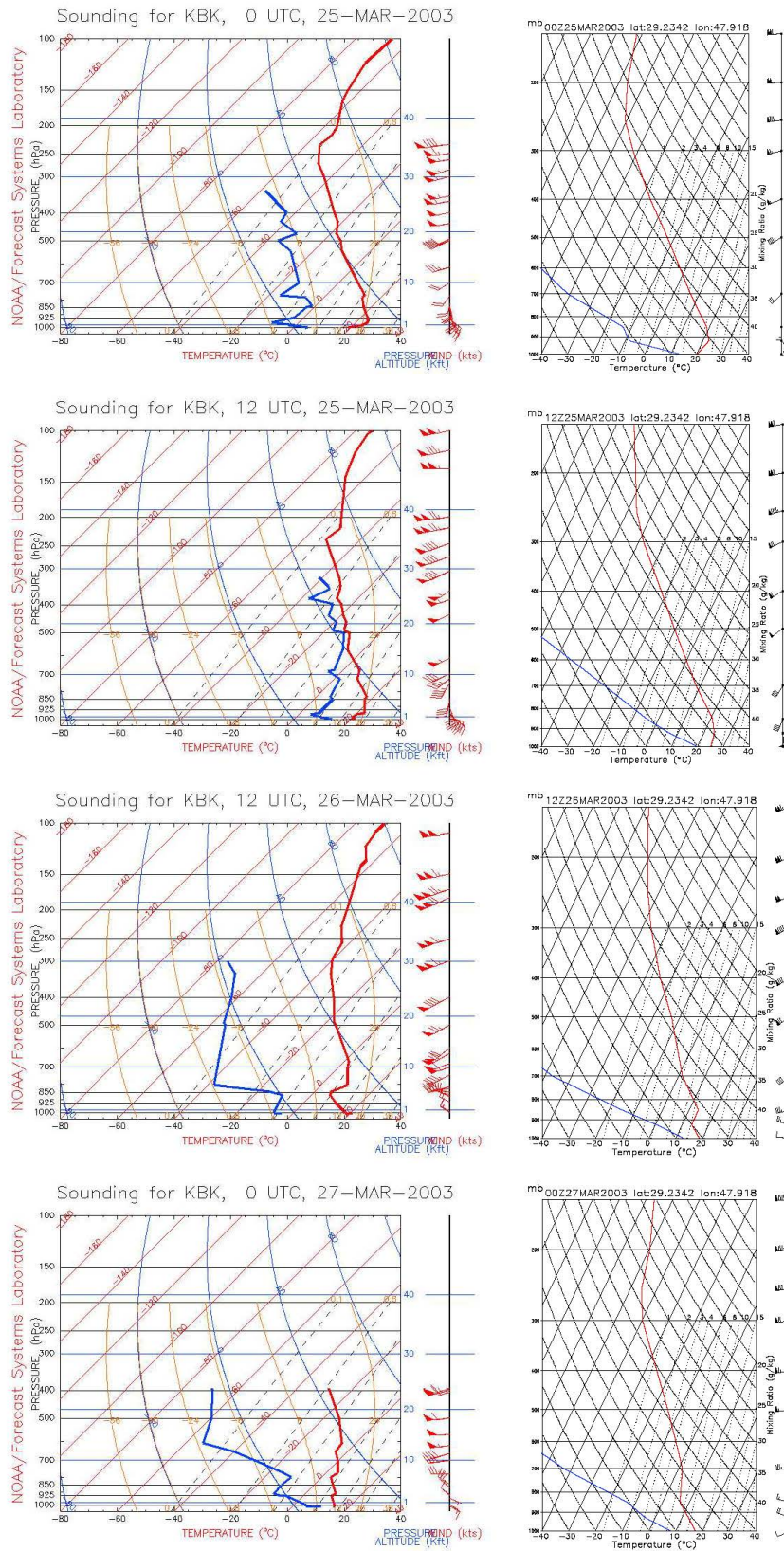
Figure 5.6: RAOB soundings vs. RAMS modeled conditions at Kuwait International Airport
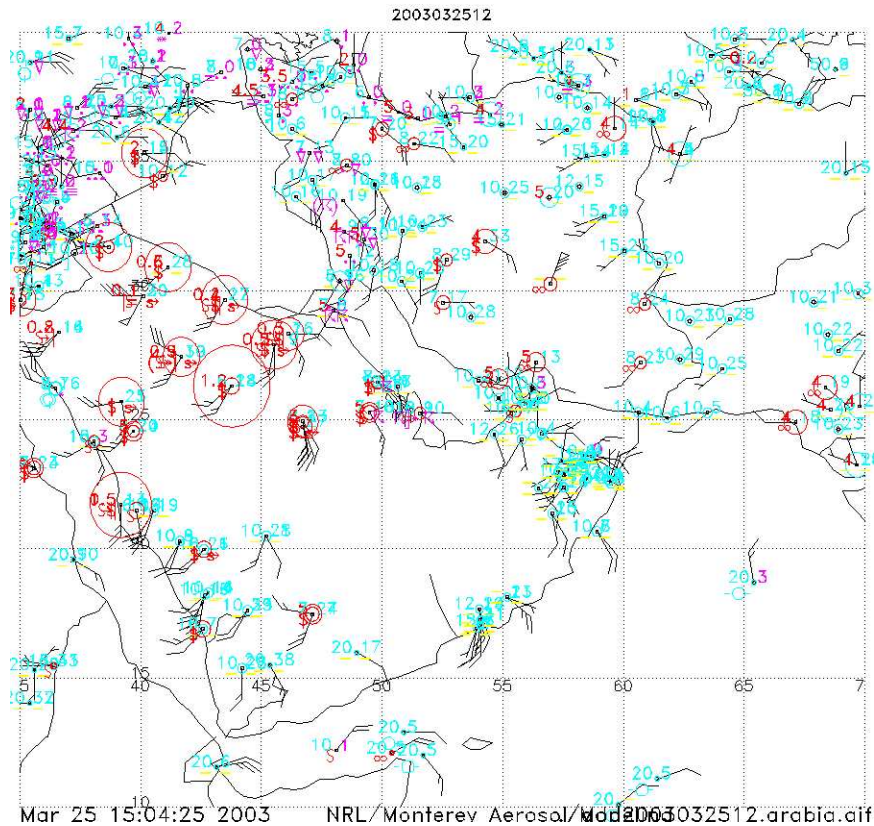
Figure 5.7: Surface plot: 12Z 25 March 2003.

The surface plot for 12z 25 March is shown in Figure 5.7. Syria and Western Iran report widespread rain and thundershowers, likely coinciding with frontal and post-frontal precipitation. Red symbols and numbers denote visibility-reducing effects: The '$' symbol indicates locally-raised dust or sand, 'S' is indicative of a dust storm and numbers are station visibility in kilometers. A single yellow horizontal indicates a missing value for that station. All stations in Northern Saudi Arabia are reporting reduced visibility due to sand or dust along with a number of stations in central and Northern Iran. Observations are unfortunately missing from Iraq through this case.

Figure 5.8 shows dust load at the surface and at 1, 3 and 5km above ground. The plot of surface concentrations also includes wind speed. As can be seen by referring back to Figures 5.2 and 5.3, the winds have increased around the strongest dust sources and are

54

out of the southwest [as seen in the ADP plot]. Not surprisingly, the highest loads at the surface correspond to the intesection of strong sources and high winds. The influence of precipitation is evident as it wraps around the North of Iraq, forming a strong gradient. This also provides a good picture of the position of the front and its influence in dust generation. The 1km layer shows similar structure to the surface load. Change is evident at the 3km and 5km layers, where a significant amount of dust has been injected and lies ahead of the front. Some of these concentrations are somewhat suspect in light of the fact that RAMS does not yet allow for cloud scavenging of dust particles; it is likely that the model is overpredicting the amount of dust that makes it high into the atmosphere, although this can't be verified.

Figure 5.9 shows the surface visibility and atmosphere optical thickness, the latter being derived from the former, thus both span the range from 245nm – 700nm. Note that the RAMS optical thickness accounts for all aerosol species, including cloud water and hydrometeors. A SEAWIFS image from 12z shows thick cloud over the Persian Gulf and parts of Northeast Saudi Arabia. Areas of decreased visibility correlate well with surface dust over Iraq and Saudi Arabia. By comparing with Figure 5.8, it appears that surface dust concentrations of less than $500\mu\text{gm}^{-3}$ are associated with visibility of greater than 10km and would not likely be reported by ground stations. An area of low visibility over Turkey isn't associated with heavy dust loads, but is co-located with an area of high optical thickness and moderate precipitation. Surface stations in the area also reported moderate to heavy rain showers at this time. By far the highest optical thicknesses appear to be associated with the frontal precipitation (and cloud, which is not shown in these plots). Comparing the model visibility to those reported on the ADP plot, it appears that RAMS overpredicts values in Kuwait and along the Southern border of Iraq. An incursion of dust-free air into North-Central Saudi Arabia lowers dust concentrations significantly and likely accounting for this apparent discrepancy.
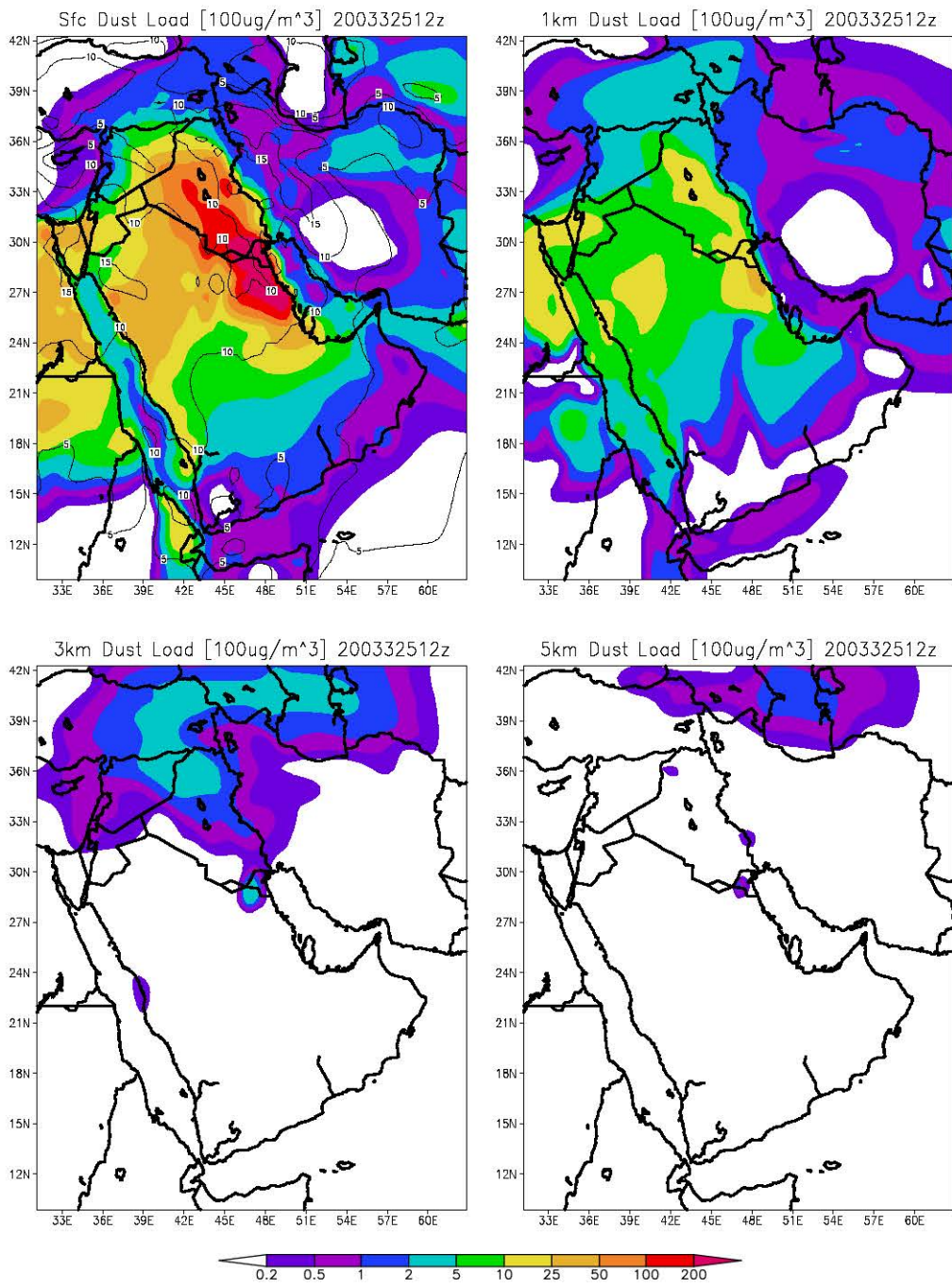
Figure 5.8: Vertical stratification of dust: 12Z 25 March 2003.
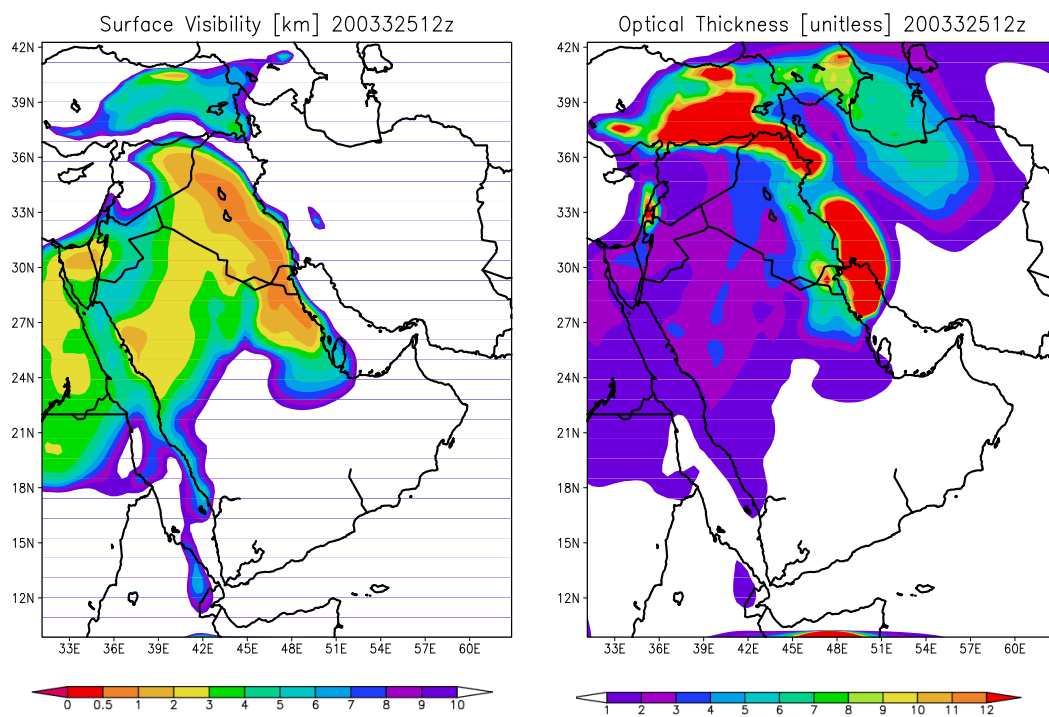
Figure 5.9: Surface visibility and atmosphere optical thickness: 12Z 25 March 2003.
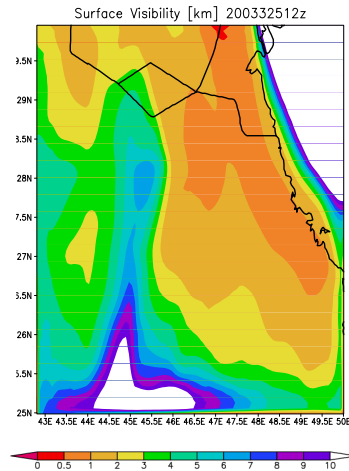
Figure 5.10: Surface visibility, grid 2: 12Z 25 March 2003.

Figure 5.10 shows the surface visibility in grid 2, with a horizontal resolution of 10km. The incursion of cleaner air can be seen better here, and like the coarse grid 1 most visibilities seem to be overforecast by a factor of about two. The results improve somewhat if a selection of points are taken from the model results, thereby avoiding the smoothing effects of contouring. Table 5.1 shows side-by-side comparisons of five geographical points. All points are overestimated, three of them by nearly a factor of ten. Since there was no model precipitation in the area of these points, the error is presumably due to an underestimation of the emitted dust. There could be many causes including poor resolution of sources, incorrect parameterization of particle sizes and properties or simply poor characterization of the meteorology.

Figure 5.11 shows the ADP plot for 12z 26 March. Like 12z on the previous day, there

Point(grid)	1(2)	2(2)	3(2)	4(1)	5(1)
Lat N	26.3	27.7	29.0	32.0	21.5
Lon E	43.5	45.2	43.5	38.5	39
ADP Vis [km]	1.2	0.5	0.2	2.0	0.5
RAMS Vis [km]	3.5	4.9	2.0	4.4	4.2

Table 5.1: Point visibility comparison, RAMS versus observed. 12Z 25 March 2003
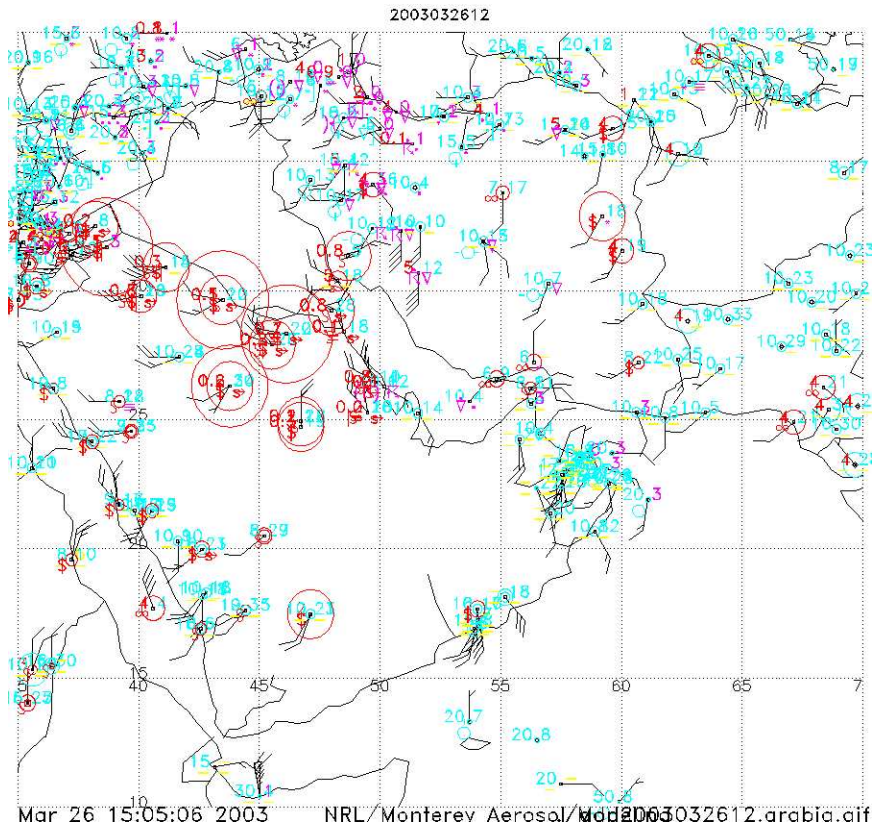
Figure 5.11: Surface plot: 12Z 26 March 2003.

are widespread reports of dust and reduced visibility. These are all throughout Saudi Arabia, with several reports in Eastern Iran. There is also widespread shower and thunder shower activity throughout Syria, Northwestern Iran and presumably Iraq. RAMS predicted heavy precipitation in Southwestern Iran, where there are no reporting stations to either confirm or refute, but for the most part missed the heavy showers along the Iran-Iraq border.

Figure 5.12 shows the vertical distribution of dust through the model domain. The highest surface loads are once again concentrated around Kuwait and Southern Iraq, with substantial loads spreading through most of Saudi Arabia. The extent of model dust matches the reported dust, though much of the area has no stations reporting so it is difficult to validate the high loads over central Saudi Arabia. The 1km loads mirror the surface with the exception of a large quantity of dust over the North end of the Persian

Gulf. A comparison with the precipitation map shows that the front passed over this area within the last three hours and injection to this height was likely a result of vigorous frontal uplift. Loads of up to $500\mu\mathrm{gm}^{-3}$ are evident at the 3km and 5km layers, once again slightly suspect due to the inability of clouds to scavenge. It is evident however that dust is easily advected to high altitudes, something that is necessary for long-distance transport.

Figure 5.13 shows the surface visibility and optical thickness. Most areas of impeded visibility are co-located with high surface dust load, though the precipitation in Iran produces some lower values. The area of extremely low visibility in the southeast corner of the plot is associated with very high vapor and relative humidity in the model and is likely a fog bank. Agreement with the surface observations is good near Kuwait and along the Southern border of Iraq, but looks to be significantly high further to the West and into Syria. Reasonably high optical thickness is co-located by dust, with the high load at 1km over the Persian Gulf clearly visible. The highest values are associated with precipitation and cloud, something confirmed by satellite images and surface observations. The area of low optical thickness centred around 36N, 51E is at first puzzling, but a look at the thickness map in Figure 5.3 shows strong winds, and this may be an area of relatively thin cloud and dust-free air. Figure 5.14 shows the visibility in grid 2. The latter shows a good capture of the low visibilities reported around the intersection of the Saudi Arabia-Iraq-Kuwait borders, with values of 0.5-2km compared to reported visibilities of 0.3-0.8km. The western portion of the grid still shows good agreement, but still overestimates.

Table 5.2 compares five points for ADP versus RAMS visibility. Model performance is significantly better at this time. Point #3, lying within the second grid, is overpredicted by a factor of four, but the two remaining points are very close to the observed visibility. Point #5 is the only poorly predicted station with RAMS significantly overpredicting the visibility by 4.7km, or almost 25 times the observed value.

60
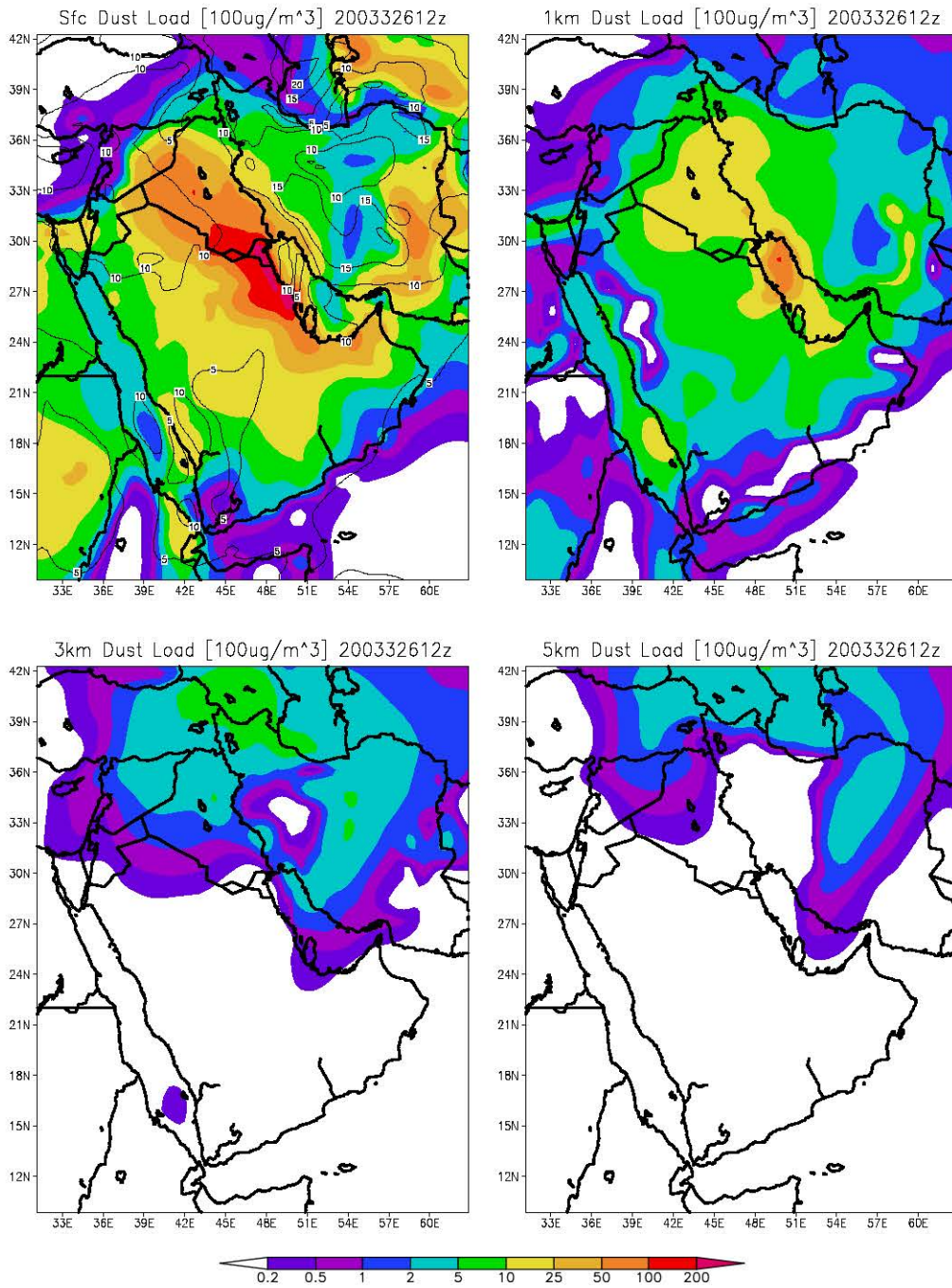
Figure 5.12: Vertical stratification of dust: 12Z 26 March 2003.
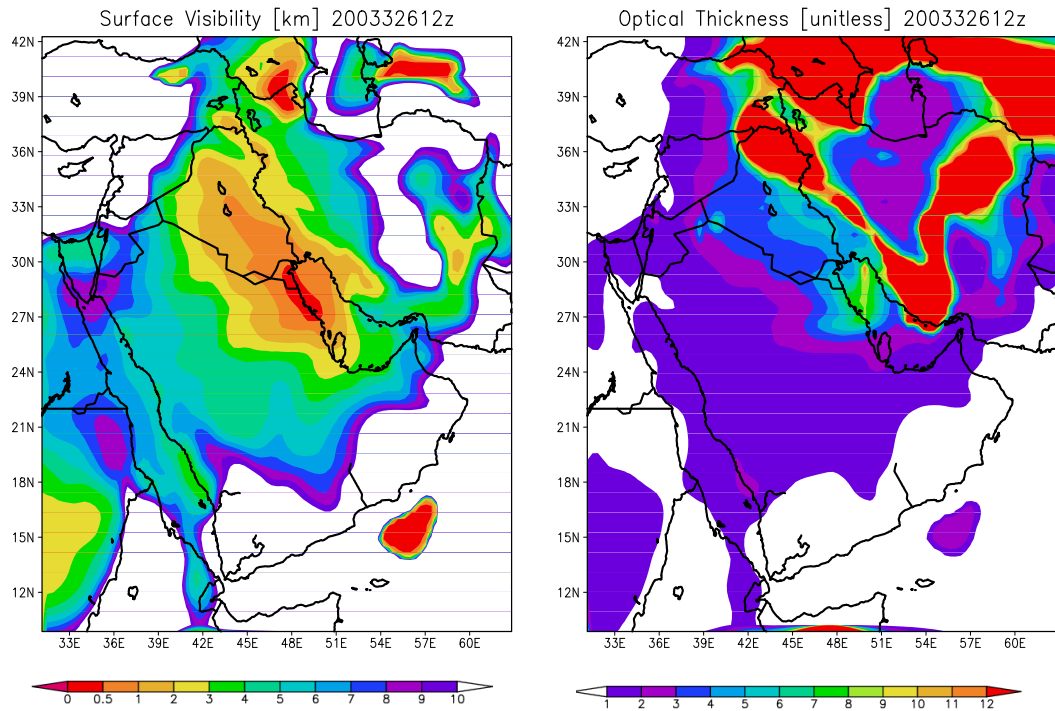
Figure 5.13: Surface visibility and atmosphere optical thickness: 12Z 26 March 2003.
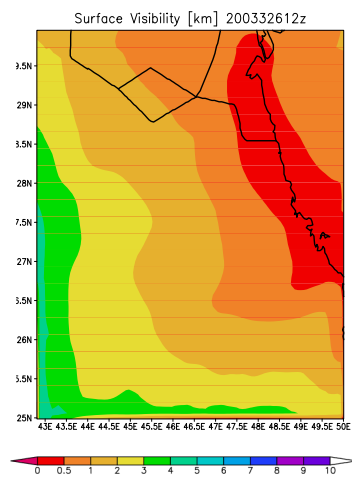

Figure 5.14: Surface visibility, grid 2: 12Z 26 March 2003.

Point(grid)	1(2)	2(2)	3(2)	4(1)	5(1)
Lat N	25.0	29.0	29.5	31.5	32.5
Lon E	47.0	48.0	43.5	60.0	38.0
ADP Vis [km]	0.2	0.8	0.5	4.0	0.2
RAMS Vis [km]	0.1	0.4	2.1	2.8	4.9

Table 5.2: Point visibility comparison, RAMS versus observed. 12Z 26 March 2003

The last verification product used to evaluate this case comes from the Aeronet site at Solar Village [24.9°N, 46.4°E]. There are unfortunately large gaps in the data, but a comparison can still be made. It should be noted that data used here are optical thickness level 1.0 data, meaning that they have not been quality-controlled or cloud screened, since RAMS includes cloud effects.

The RAMS optical thickness for 25 March is consistently slightly over twice what was measured by Aeronet. The station lies at the Southern tip of an area of high dust load and the band of frontal precipitation passes over between 09z and 12z, possibly responsible for the measured spike at 0930z. RAMS does capture an increase in optical thickness after 830z, though the magnitude is much smaller than is shown on the Aeronet plot. Data are missing from 26 March, so the only remaining comparison is for 27 March between 00z and 12z, when the run ends. Aeronet and RAMS values are comparable at 02z, but the model again misses a sudden drop in optical thickness and remains elevated, about 1.2 versus the 0.5 on the Aeronet plot. An examination of the dust plots (not shown) reveal that Solar Village still lies just within the Southern tip of high dust load at the surface. ADP plots do show very low visibility within close proximity to the North and East so it is possible that this very dusty area simply extends slightly too far South. The model performance with regards to optical thickness in this instance is fair, falling generally within a factor of two, more validation data would help to further explore performance with regards to columnar dust load in this case.
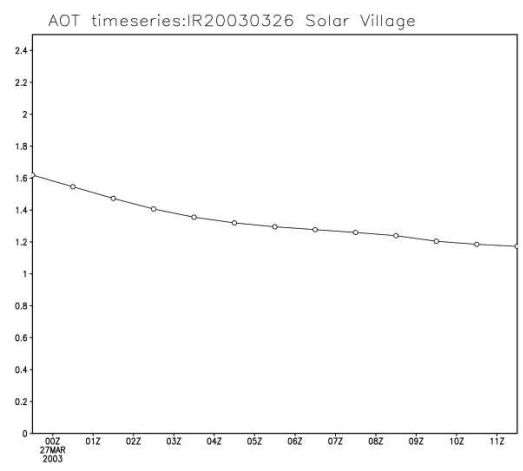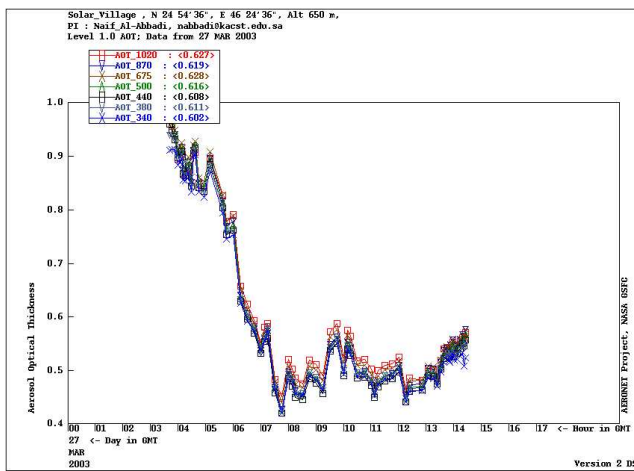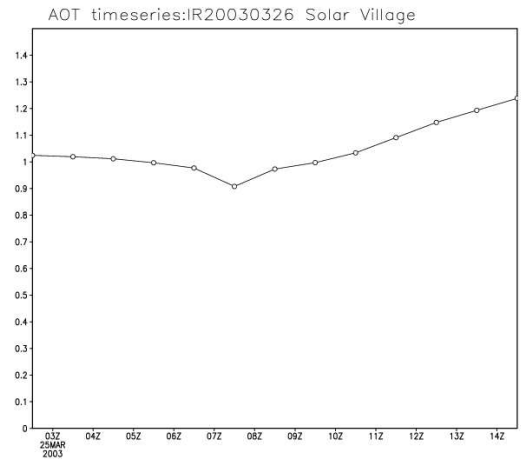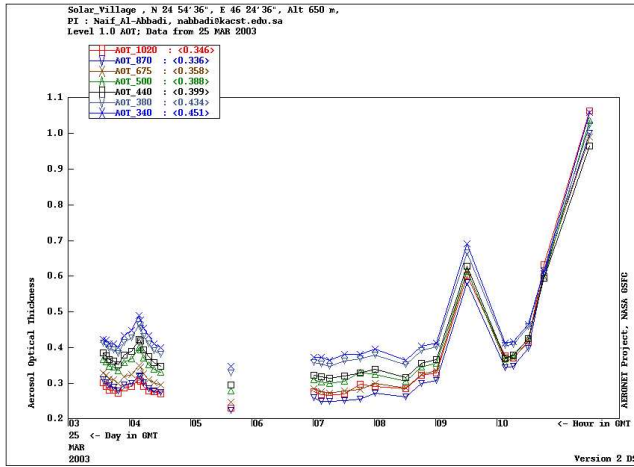
Figure 5.15: Aeronet [left colummn] versus RAMS optical thickness timeseries, 25 and 27 March 2003

5.3   Dust Effects on Radiation

The effects of dust on the incoming and outgoing radiative streams, as well as on the temperature profile will be briefly examined in this section, following in the style of Stokowski (2005). As was mentioned in Chapter 2, the radiative effects of dust are calculated at each time step and fed back into the model, potentially affecting the meteorology. The next section will touch upon the resultant effects on precipitation.

Four domain-wide plots are shown in Figure 5.3. These are the changes due to dust in longwave and shortwave radiation streams at the surface. Values greater than zero are indicative of an increase caused by dust while negative values mean that dust has suppressed that particular stream. The top row shows shortwave streams while the bottom row shows changes in the longwave streams. Recall that these are derived from the eight radiation bands used in RAMS: Three in the shortwave (or solar) and five in the longwave (or terrestrial, infrared).

Not surprisingly given dust's absorbtive qualitites, areas of heavy dust (refer back to Figure 5.8) correspond to areas of reduced downwelling shortwave radiation at the surface. The areas of heaviest column load are also spatially correlated with the areas of strongest reduction, with most of the domain seeing at least a mild reduction in incoming shortwave radiation. Interestingly the only areas of enhanced downwelling shortwave radiation are associated with the edge of the front, where Figure 5.9 shows high optical thickness and Figure 5.4 shows moderate precipitation. It is apparent, at least in this case, that dust acts to reduce the optical thickness in the shortwave by thinning the clouds. The same general features are apparent in the upwelling solar radiation with the notable exception of the Red Sea due to its relatively low albedo at 12z (1500 local time).

The downwelling longwave radiation shows an increase that is well-correlated with the highest dust load in the lowest model layer. The exception to this is over Northwest

65
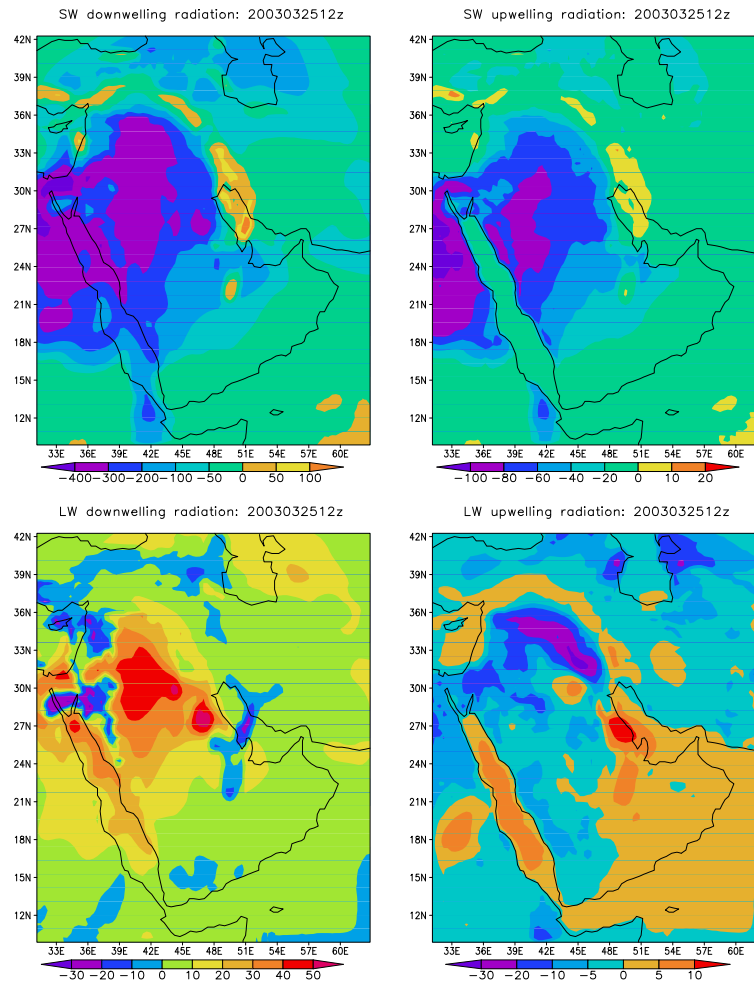
Figure 5.16: Differences due to dust in upwelling and downwelling shortwave and longwave radiation, 12Z 25 March 2003

Saudi Arabia where a reduction in precipitation and cloud cover in the dusty case appears to be responsible for a corresponding reduction in downwelling longwave radiation. Changes in upwelling longwave radiation are for the most part a mirror image of the changes in downwelling shortwave radiation, while also influenced by changes in downwelling longwave radiation. Areas of water are the exception here, where higher heat capacity reduces the sensitivity to temporary changes in incoming radiation.

Changes in the vertical radiation streams are examined at Kuwait International Air-
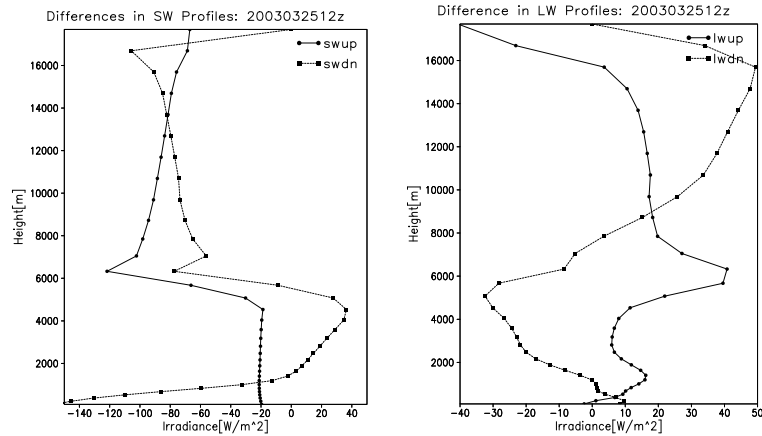
Figure 5.17: Vertical dust concentration and changes in radiation streams, 12Z 25 March 2003.

port in Figure 5.3. Once again referring to Figure 5.8, heavy dust loads are apparent in the lower layers. A noticeable reduction in downwelling shortwave radiation occurs up to very high levels. This is explained by increased convection and cloud over Kuwait in the dusty case. The slight increase in radiation around 4km is attributable to widespread low cloud and precipitation in the 'no dust' case. Lower levels, with high dust loads, experience the same sharp reduction in incoming radiation as was seen in Figure 5.3. The upwelling short-wave stream is likewise sharply reduced at upper levels. Changes in the longwave streams are shown in the righthand panel. A slight increase near the surface is likely attributable to the high dust concentrations, though it may be offset by the accompanying decrease in downwelling shortwave radiation. Higher cloud-top height in the dusty case may explain the slight decrease in upwelling longwave radiation at high altitudes.

An significant consequence of the changes in shortwave and longwave radiation streams is an increase in temperature close to the surface. Figure 5.3 shows the temperature profile in the lower atmosphere for both dusty and dust-free cases alongside the vertical dust profile. A significant temperature increase is evident up to about 1.8km, along with a strengthened inversion. Note also that the increased temperature persists well above the
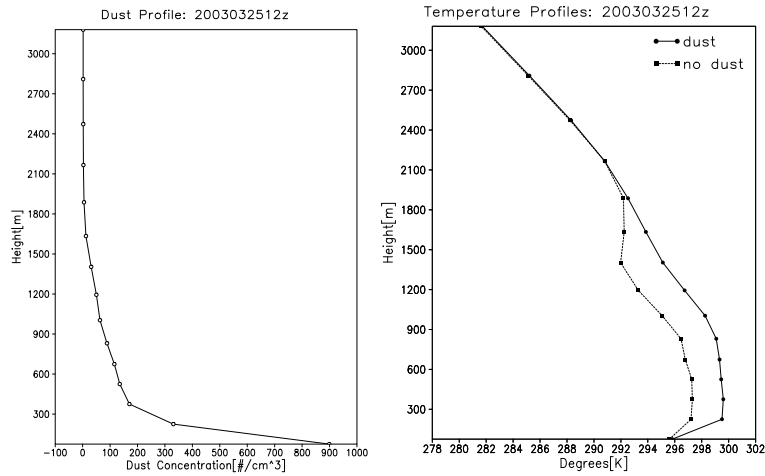
Figure 5.18: Dust and temperature profiles, 12Z 25 March 2003

high dust concentrations, which taper off to below $100cm^{-3}$ at around 500m.

00z 26 March is examined as a 'night' case to better see the lingering effects on radiative streams. The shortwave is not examined in this case as it corresponds to 0300 local time. The effects on the longwave radiation domain-wide at the surface are shown in Figure 5.3. The magnitude of effects is much smaller than during the daytime, but the effects of dust are still evident near the surface where concentrations reach up to $2000cm^{-3}$. The extent of enhanced upwelling longwave radiation closely matches the area of high surface dust concentration. The patch of increased upwelling radiation in the northwest corner of the domain is cloud-free in the dusty case but overcast in the dust-free case. Downwelling longwave radiation is likewise heavily influenced by the presence of high dust concentrations in the lower atmosphere and is increased over most of the domain.

The longwave radiation profiles over Kuwait International Airport are shown in Figure 5.3. The vertical concentration of dust peaks at about 500m, coinciding with a peak in downwelling radiation. This decreases to near zero at 5km with another peak in both upwelling and downwelling longwave radiation at 6km. Dust concentrations are near zero
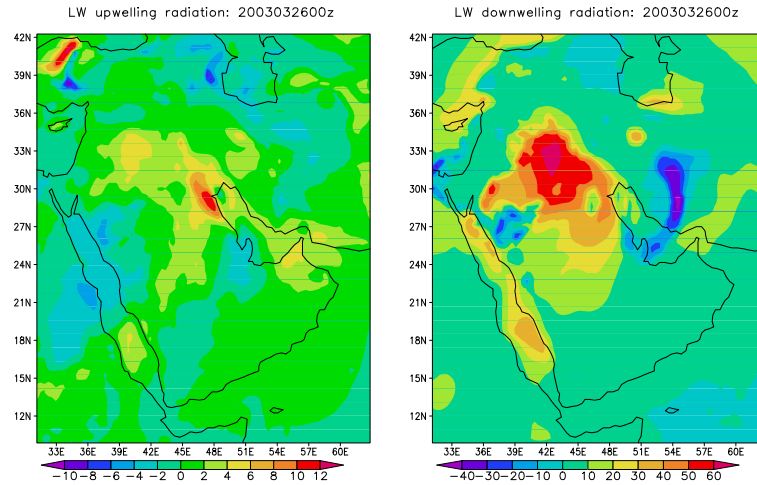
Figure 5.19: Differences due to dust in upwelling and downwelling longwave radiation 00Z 26 March 2003

at this altitude and this latter peak is likely attributable to cloud effects.

From this brief examination it is evident that dust can have potentially large impacts on the radiation streams in the shortwave and longwave bands. These manifest themselves not only through increased heating near the surface, but also in stronger inversions and decreased cloud thickness. These results match qualitatively what was found by Stokowski (2005) while testing with fixed dust profiles.

5.4   Suppression of Precipitation by Dust

In light of the results of the previous section along with the sometimes poor simulation of precipitation, the effects of dust on liquid precipitation are examined. Comparison is made between the present run, and another run with identical parameters except that dust sources are deactivated and its radiative effects are removed. Dust can affect precipitation by modifying the boundary layer as well as through the semi-direct effect.

Figure 5.4 shows a series of images spanning the period from 18z on 25 March to 09z on 26 March. The shaded contours represent the deficit in precipitation caused by
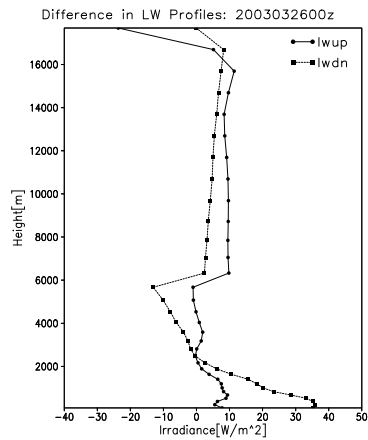
Figure 5.20: Changes in longwave radiation streams, 00Z 26 March 2003.

atmospheric dust: A positive value means that dust is enhancing precipitation over the clear air case. Plain black contours show the 1km dust concentration, to give an idea of how important the deficit or enhancement may be. As can be seen there is no constant, and dust has the potential to either enhance or suppress precipitation over a clear air case. This adds a dimension of complexity to the model, as the choices for dust radiative, size and mass characteristics will now affect not only the visibility, but also the cloud cover and precipitation.

The remaining cases will be examined in a style similar to what has been presented above, albeit with slightly less meteorological detail. RAMS was found in this case to have done a fair job of predicting these variables with the exception of the dewpoint profile. Further examination showed that incorrect cloud and precipitation forecasts also propogated through the model to produce errors in the visibility and optical thickness forecasts as well.
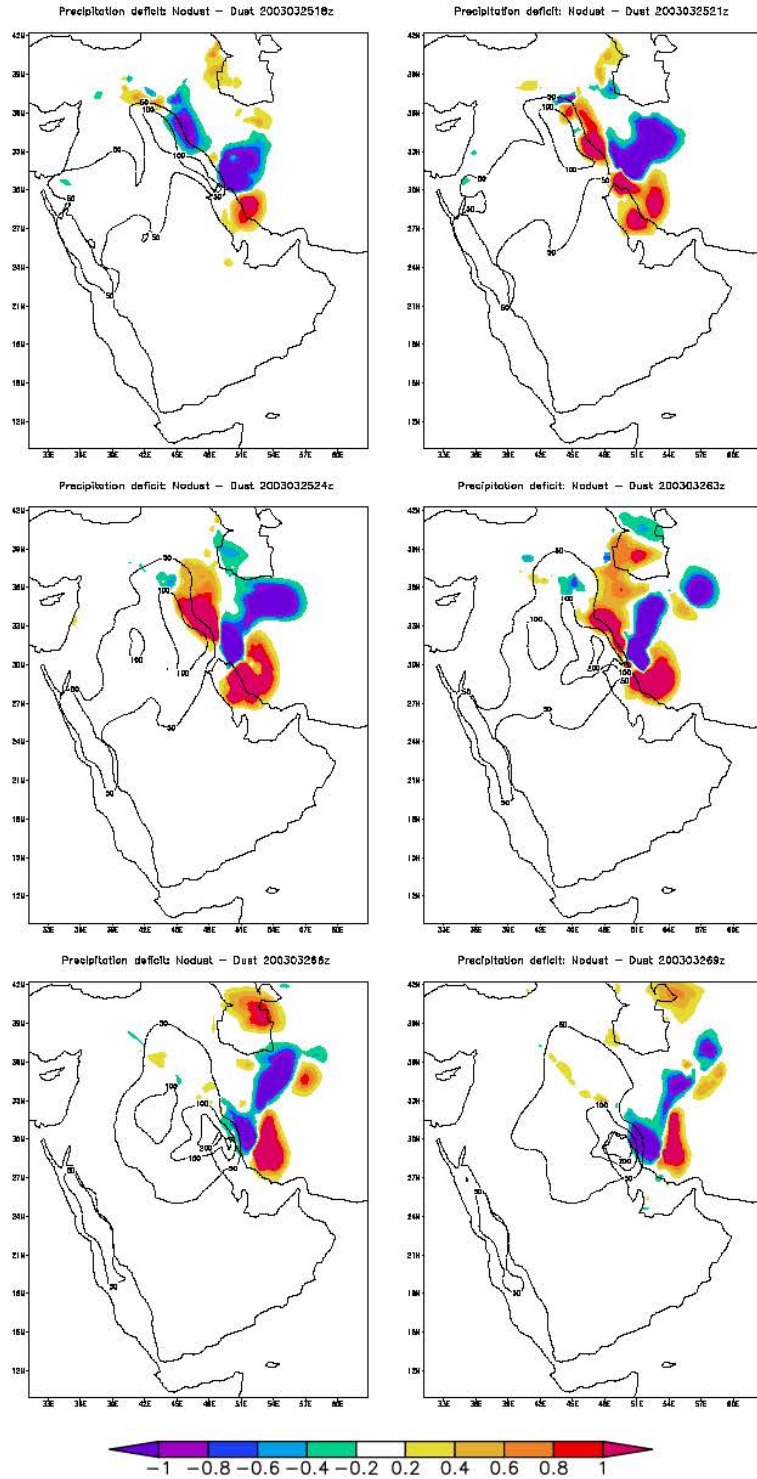
Figure 5.21: Suppression in precipitation rate [mm/hr] - Clear air versus dusty air. Contours are dust concentration [cm^{-3}] at the 1km model layer

Chapter   6

CASE IR20060310

As with IR20030325, this case examines a recent dust storm in the Middle East. The meteorological conditions were well-documented and some verification for dust and visibility was available via Aeronet and ADP surface plots. A two-day period was chosen for the model run, this time from 18z 8 March through 06z 11 March 11. As usual, the first six hours are discarded for model spinup, giving an effective start time of 00z 9 March. Two grids were used and are shown, along with NCEP reanalysis initial conditions, in Figure 6.1. Grid 1 spans 9.8°N to 42.2°N and 26.1°E to 57.8°E while grid 2 covers 40.2°N to 49.4°N and 25.7°E to 33.8°E. Localized outbreaks appear in the eastern part of the domain as early as 00z 9 March and progress eastward, reaching the Persian Gulf on the 10th and mostly disappearing by early morning 11 March.

6.1   Meteorology

The synoptic conditions are examined, though in somewhat less detail than in IR20030325. Plots of 1000-500mb thickness and surface wind speed are shown every 12 hours in Figures 6.2 and 6.3, with the last plot at 06z 11 March given at a 6-hour interval. Similar to IR20030325, generation here is due to a low pressure system that moves across the domain in a generally westerly direction. High surface winds start to develop around source regions [see Figure 2.2] early on 9 March as the low dips slightly to the South. Surface winds remain in excess of $10\mathrm{ms}^{-1}$ until late in the day on 10 March. As the low moves out over the Black
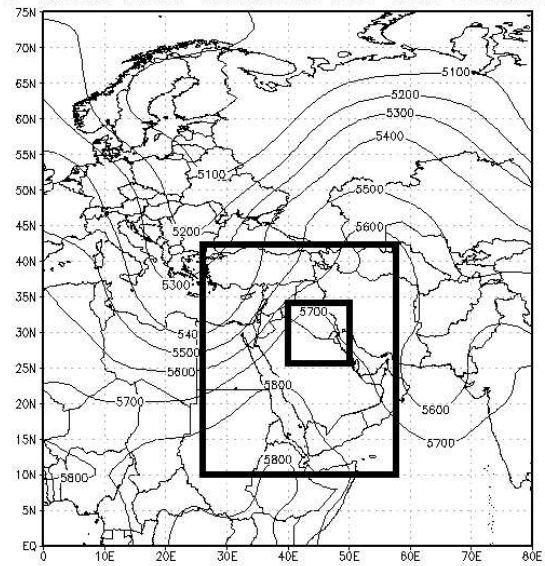
Figure 6.1: Location of Grids 1 and 2 for run IR20060310

Sea early on 11 March, a small region of high winds remains in the Northern Persian Gulf. These plots were compared qualitatively with 6-hourly NCEP reanalysis plots and with exception of strong surface winds along the Northwestern Persian Gulf at 12z on the 10th, pressure and wind fields were well-simulated by RAMS.

RAMS develops patchy frontal precipitation which reaches a maximum during the evening of 9 March and into the morning of 10 March. This is shown in Figure 6.4. Maximum rates briefly reach $3 \mathrm{mmhr}^{-1}$ over a very limited area as the band tracks to the Southeast toward the Persian Gulf. The location and timing of the model precipitation agrees with ADP surface plots, however the horizontal extent appears to have been underpredicted.

SkewT diagrams are not included for this case, however five stations were examined for successful reproduction of wind speed and direction, vertical temperature profile and boundary layer features. Once again, there was a serious dry bias at every station. The domain for this run includes much of the Mediterranean, so it seems unlikely that the hypothesis advanced for the problems in IR20030325 applies here. Initialization of moisture may be to blame but with limited sources of initialization data there is no way to test this. Regardless, this will likely lead to a high bias in dust concentrations for some frontal and post-frontal regions.

Overall, RAMS does well in simulating the synoptic environment during IR20060310. The glaring exception to the successful simulation is once again the poorly-simulated dewpoint (the dewpoint depression was never below 10°C at any of the stations examined) and its impact on rainfall rate and extent. Upper level winds were especially well represented and nighttime inversions were captured about 80% of the time.
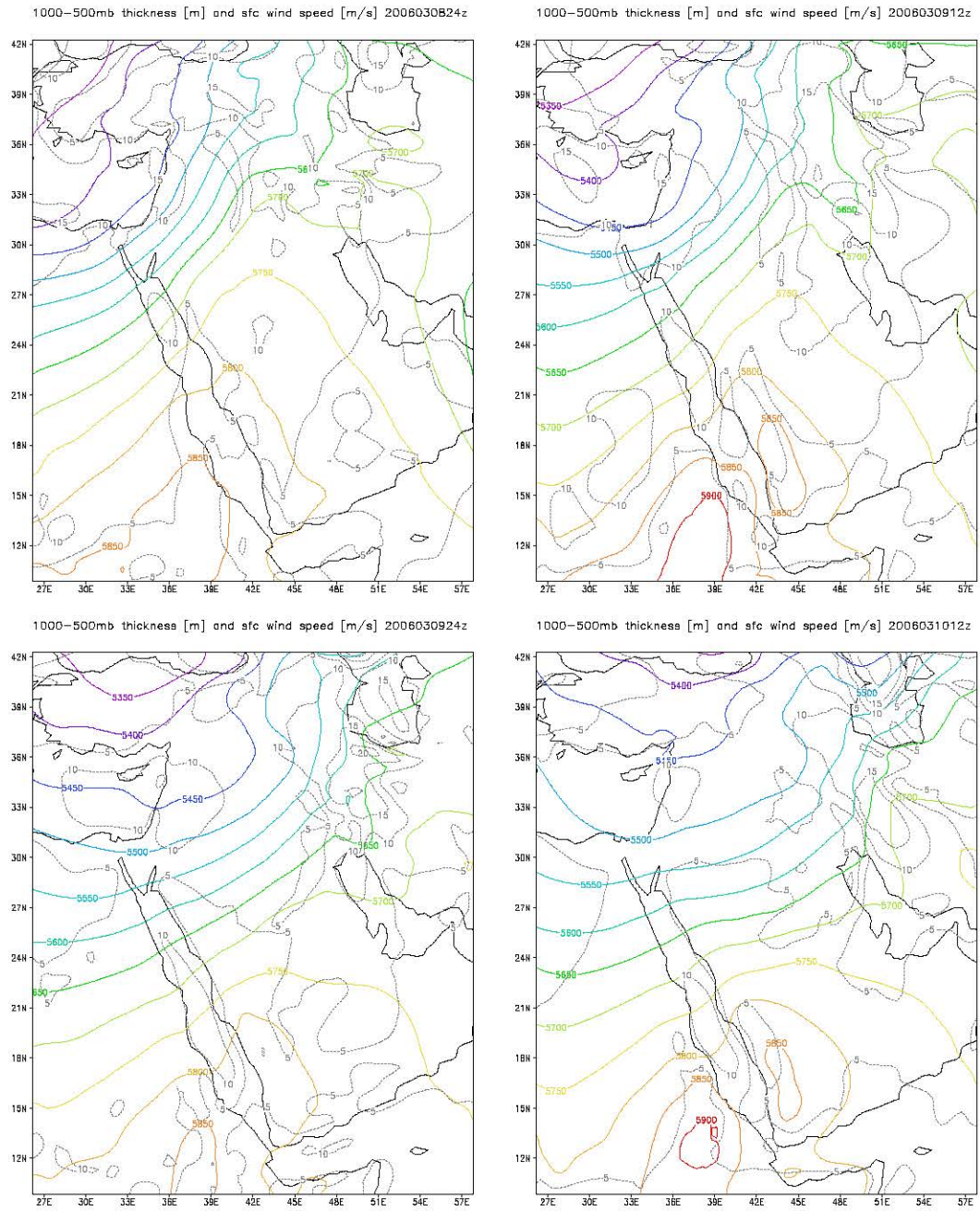
Figure 6.2: 1000-500mb thickness [m] and surface wind speed for the period 00Z 9 March to 12Z 10 March. Temporal progression is left to right, top to bottom.

1000−500mb thickness [m] and sfc wind speed [m/s] 2006031024z

1000−500mb thickness [m] and sfc wind speed [m/s] 200603116z
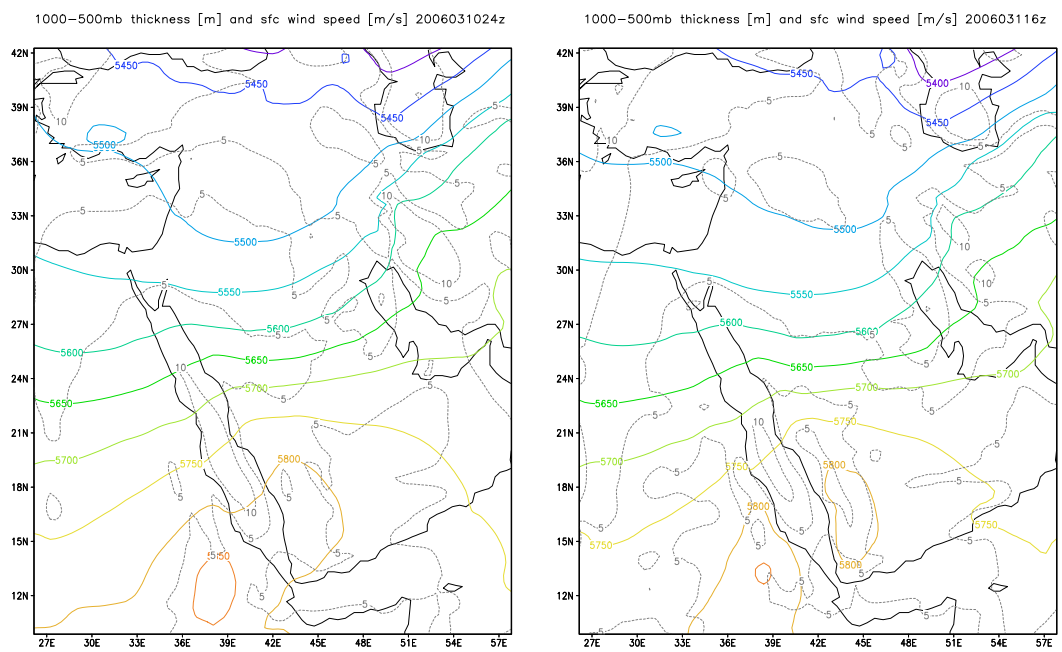
Figure 6.3: 1000-500mb thickness and surface wind speed for 00Z and 06Z 11 March.
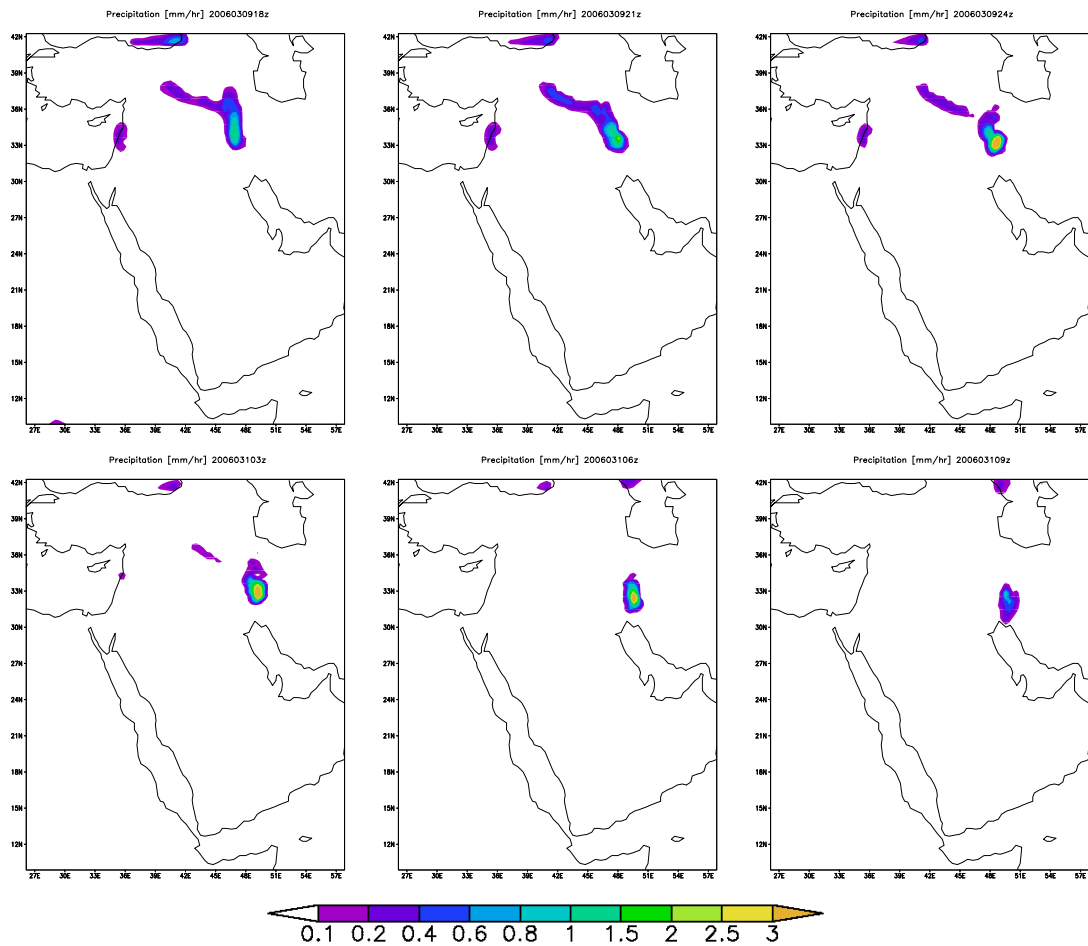
Figure 6.4: Surface precipitation rate [mm/hr] for the period 18Z 9 March through 06Z 10 March, 3-hour time step. Temporal progression is left to right, top to bottom.

6.2   Model Dust Results

Modeled and observed dust-related weather are compared using ADP surface plots, Aeronet time series and back-trajectory plots. Because the domain extends further west than IR20030325, it is useful to examine the back-trajectories to find air masses that have passed over the Sahara-Sahel region, thus possibly entraining dust that wouldn't be resolved in this model run. Once again two distinct times are chosen for the comparison of modeled and observed visibility.

The ADP visibility-reducing surface plot is shown in Figure 6.5. Surface winds are southerly, and a large number of stations at the north end of the Red Sea are reporting locally-raised or suspended dust. More sporadic reports extend east to the Persian Gulf, and into Northern Iraq. Most of Turkey and parts of Western Iran are reporting drizzle, showers and fog. Though not shown in Figure 6.4, model precipitation was occurring in parts of Turkey at rates of less than $0.2\mathrm{mmhr}^{-1}$. Additionally, this case benefits somewhat by the fact that reports are available throughout most of Iraq. The model back-trajectories from Aeronet show air parcels below 500mb coming from the South for the preceding three days, so any observed dust should be either locally raised, or come from an area that is resolved by the model.

The dust load at the surface and 1km, 3km and 5km is shown in Figure 6.6. From analysis of IR20030325 it appeared that a load of less than $500\mu\mathrm{gm}^{-3}$ wouldn't be reported. If this is the case, then the extent of the surface dust as forecast by RAMS closely matches that reported by surface stations. Depending on the intensity of the actual precipitation, it is also possible that model dust is overforecast. The highest loads are forecast over central Iraq and Kuwait. A significant amount of dust is present in the 1km layer, with some injection up to the 3km layer. The 5km layer shows no dust loads greater than $20\mu\mathrm{gm}^{-3}$

The surface visibility, along with column optical thickness, is shown in Figure 6.7.

Figure 6.5: Surface plot: 12Z 9 March 2006
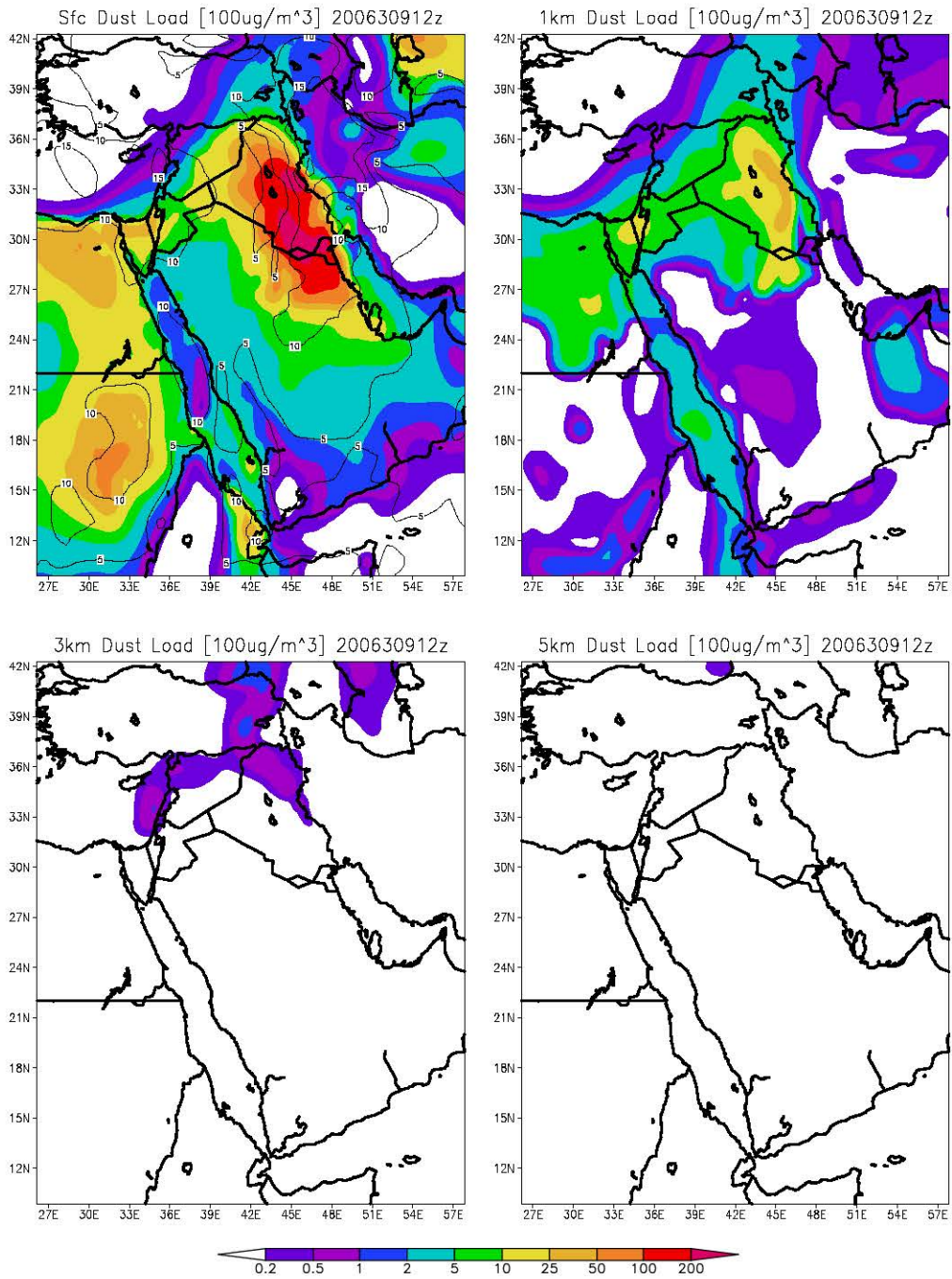
Figure 6.6: Vertical stratification of dust: 12Z 9 March 2006.
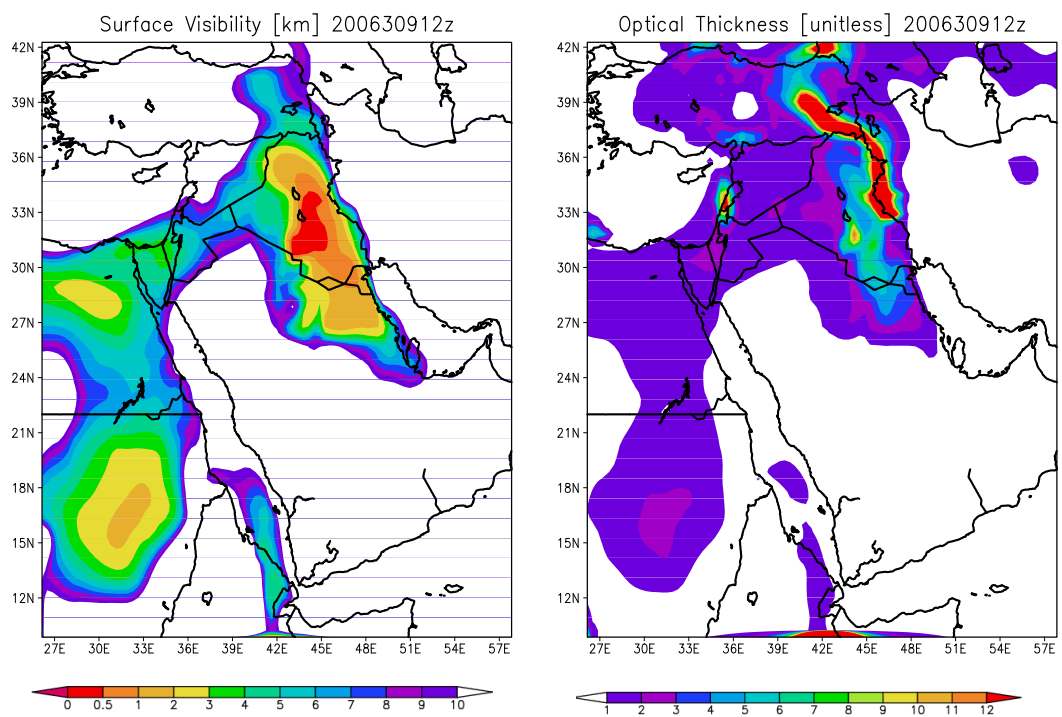
Figure 6.7: Surface visibility and atmosphere optical thickness: 12Z 9 March 2006.
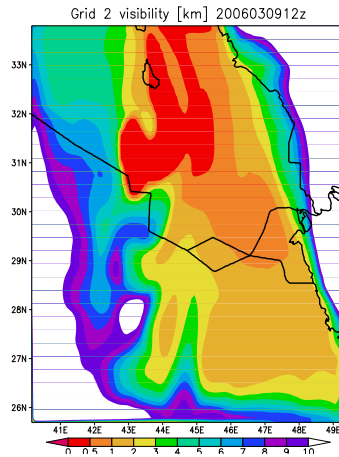
Figure 6.8: Surface visibility, grid 2: 12Z 09 March 2006.

The visibility is generally well-correlated with the surface dust concentrations shown in Figure 6.6. An area of low visibility in Eastern Turkey is due to a band of hail over that region. The contours over Iraq appear to indicate that visibility is underestimated, while an area over Syria is overestimated. Egypt has a bullseye of low visibility that corresponds well with the values reported in Figure 6.5. The higher-resolution visibility in grid 2 is shown in Figure 6.8 and the area around Iraq again looks slightly underpredicted. Values of high optical thickness correspond to high dust concentrations over Iraq, hail over Turkey and a band of cloud that extends down the Northwest coast of the Persian Gulf. The veracity of the model cloud in this area is proven by the surface reports of thunderstorms; in this RAMS did not predict the precipitation, but did adequately resolve cloud.

A 5-point visibility comparison is shown in Table 6.1. Both points in grid 2 are predicted within a factor of 1.6, while two of the three points in grid 1 are predicted within a factor of 2.6. In this case, it appears that the use of contouring obscured what were otherwise generally good results.

The ADP plot for 12z 10 March is shown in Figure 6.9. The dust front has moved across Saudi Arabia, and the majority of reports are around the northern tip of the Persian

Point(grid)	1(2)	2(2)	3(1)	4(1)	5(1)
Lat N	28.3	31.0	31.0	26.0	34.5
Lon E	46.12	46.0	41.0	32.5	41.0
ADP Vis [km]	2.5	1.0	3.0	2.5	0.8
RAMS Vis [km]	1.5	0.7	6.9	4.9	4.3

Table 6.1: Point visibility comparison, RAMS versus observed. 12Z 9 March 2006

Gulf, with lingering reports in Egypt. Surface winds have shifted to northerly and reports of precipitation and fog are confined to Eastern Turkey and Western Iran as the cold front continues to move east. Aeronet back-trajectory shows most air masses below 500mb continue to originate from the South, save for the lowest layer which is now from the north due to shifting surface winds.

The dust load is shown in Figure 6.10. Surface generation in Egypt has tapered off considerably. The areas of highest dust load are still the same over Iraq and Saudi Arabia, though the intensity has diminshed somewhat. Most dust has made its way up to the 3km and 5km layers and is moving to the northeast. Comparison with the ADP plot indicates that the areal extent is approximately correct over Egypt and Saudi Arabia, but loads appear to be below the reporting threshold over Syria where at least one station reported dust.

Visibility and optical thickness are shown in 6.11. Two large areas of lowered visibility are evident, one over Sudan and the other extending in a crescent through Iraq, Kuwait and Saudi Arabia. These are mostly due to high surface concentrations of dust, and appear to be well-approximated except for the aforementioned area of Syria where dust load was underforecast. Areas of elevated optical thickness are for the most part attributable to dust concentrations at the surface and 1km layers, though the highest value at the northeast tip of the Persian Gulf is caused by a combination of dust and precipitation. Another isolated spot of elevated optical thickness on over the Eastern Mediterranean also appears to be a combination of the two.
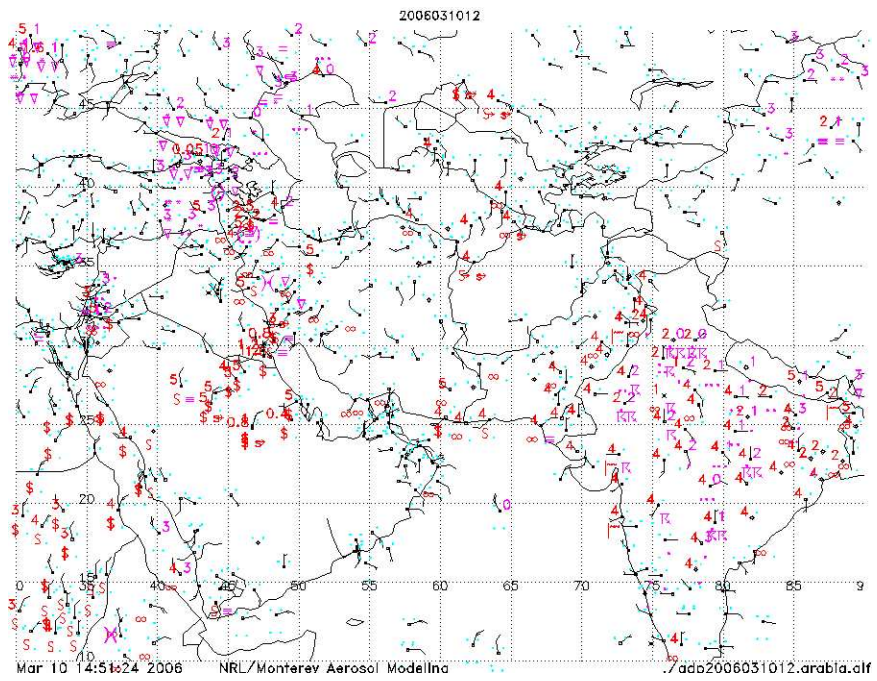
Figure 6.9: Surface plot: 12Z 10 March 2006
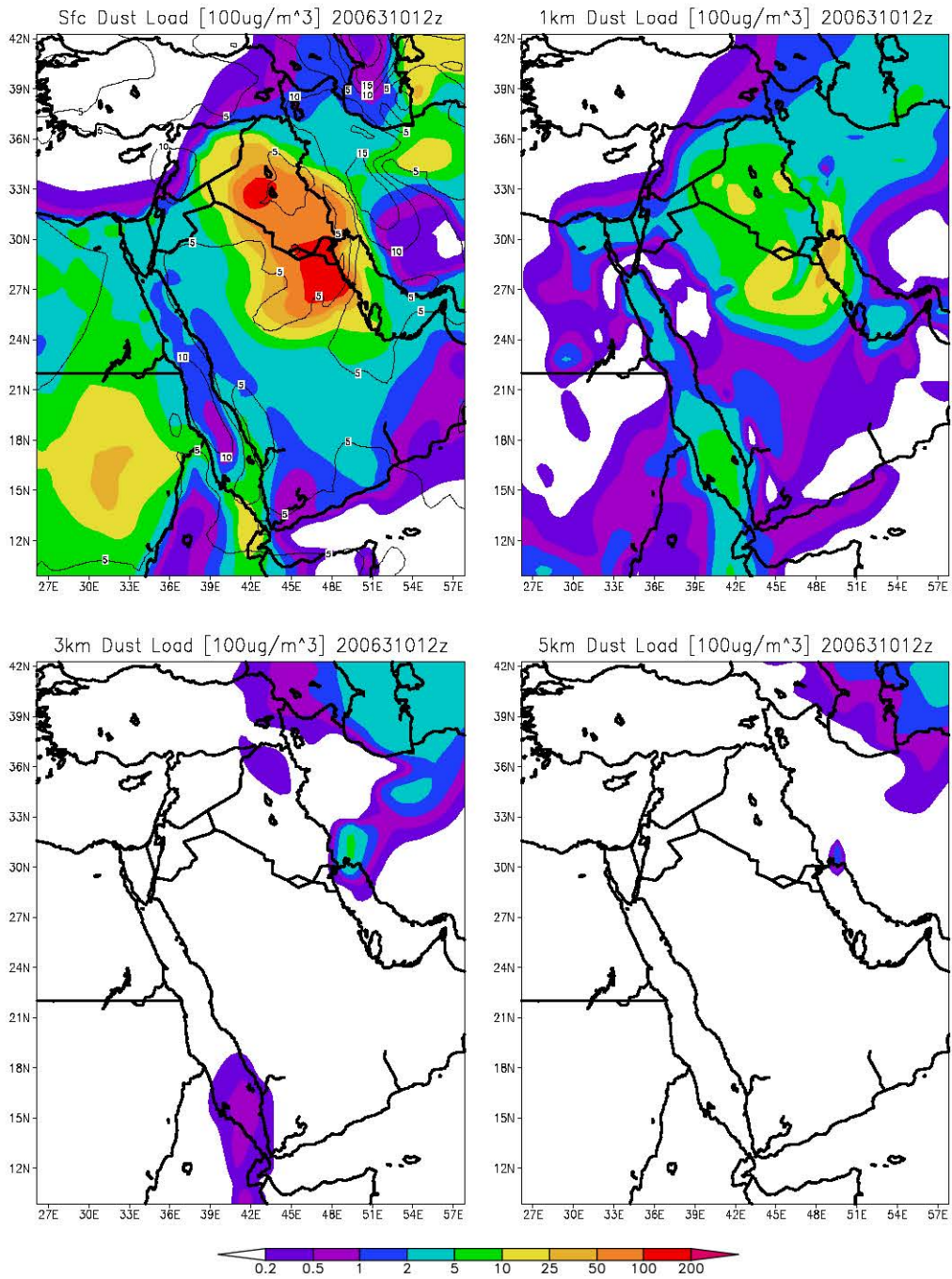
Figure 6.10: Vertical stratification of dust: 12Z 10 March 2006.
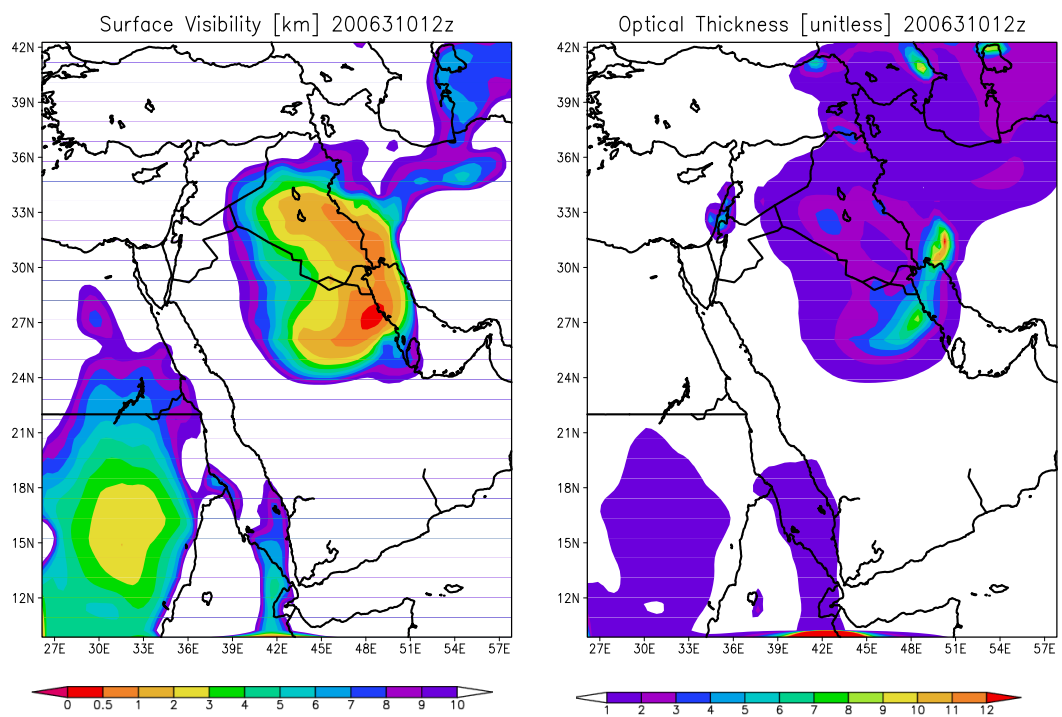
Figure 6.11: Surface visibility and atmosphere optical thickness: 12Z 10 March 2006.

Point(grid)	1(2)	2(2)	3(1)	4(1)	5(1)
Lat N	28.3	29.0	24.0	18.0	36.0
Lon E	46.1	47.5	38.0	34.0	51.0
ADP Vis [km]	4.5	0.8	4.0	3.0	5.0
RAMS Vis [km]	2.2	1.5	16.9	4.0	11.1

Table 6.2: Point visibility comparison, RAMS versus observed. 12Z 10 March 2006

The 5-point visibility comparison is shown in Table 6.2. The two points within grid 2 are still predicted relatively well, with both points predicted within a factor of two. Performance on grid 1 is within a factor of 2.1 for two of the points, but well off for the remaining point. This last may be a case of underforecast winds, since it lies near a relatively strong source and under southerly winds according to Figure 6.9.

The IR20060310 run coincided with the continuous operation of two Aeronet sites within the model domain, therefore there are three partial days of optical thickness data with which to evaluate RAMS output. The Sede Boker site is located at 30.9°N and 34.8°E, while the Solar Village site is at 24.9°N,46.4°E. Figure 6.2 shows plots from both sites against RAMS time series for 9 March. The model optical thickness for Solar Village is consistently too high. The optical thickness at Sede Boker is much better, with the model duplicating a slow increase throughout the morning but missing a sudden drop, and subsequent increase at 11z.

Plots for 10 March are shown in Figure 6.2. Solar village shows very good agreement between model and observations, with the former slightly underestimating the optical thickness at 12z when Aeronet stops reporting. Another item of note here is the miniscule spread in optical thickness for different wavelengths. This is indicative of the dominance of large particles in the atmosphere, likely meaning very strong surface winds Sede Boker only reports for two hours on 10 March, but agreement is very poor with RAMS showing triple the observed values. One possible reason for this is that precipitation and fog were reported in the area, and while an examination of the optical thickness in Figure 6.11 shows some
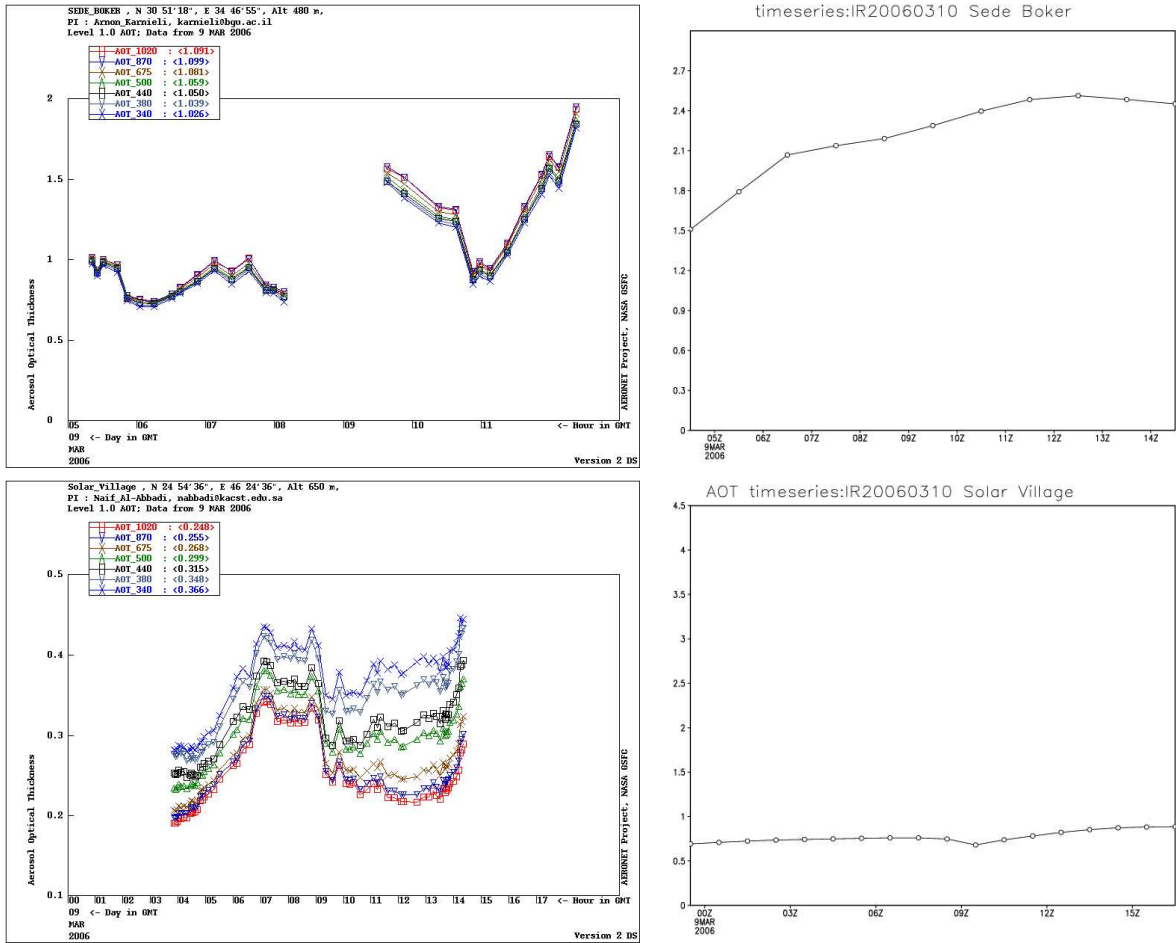
Figure 6.12: Aeronet [left colummn] versus RAMS AOD timeseries, 9 March 2006.

water vapor in the air, it is not directly over the Aeronet site and significant dust rainout may have been missed. Finally, Figure 6.2 shows data for 11 March. Only Sede Boker coincides with model runtime on this day, and once again RAMS significantly overpredicts the optical thickness, possibly for the same reason as on the previous day.
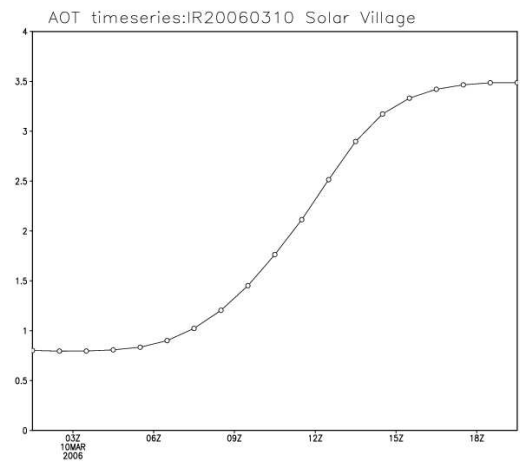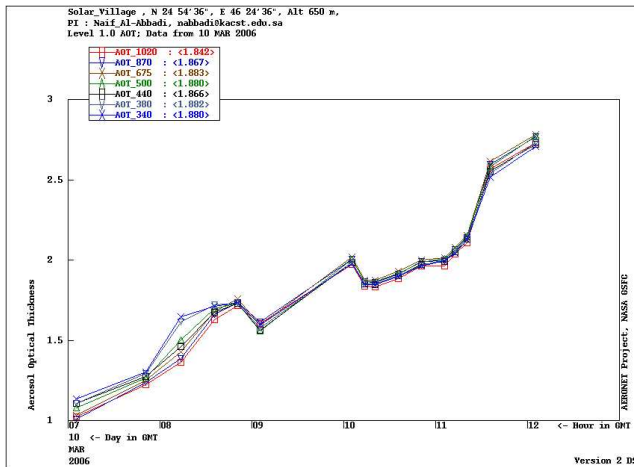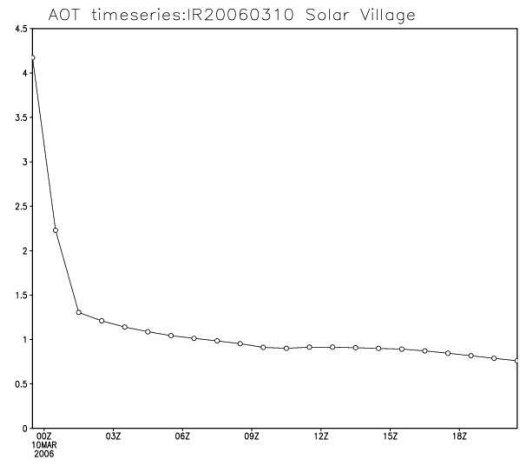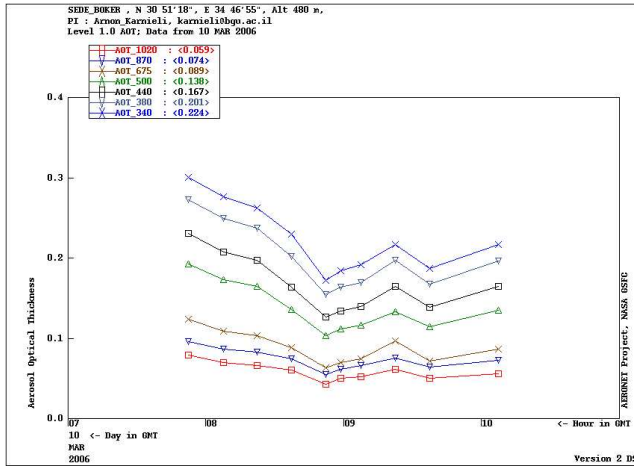
Figure 6.13: Aeronet [left colummn] versus RAMS AOD timeseries, 10 March 2006.
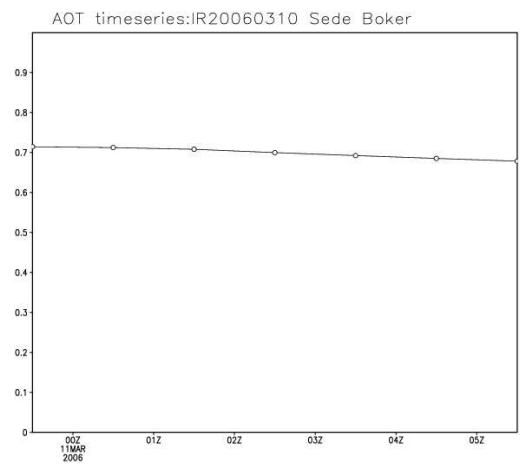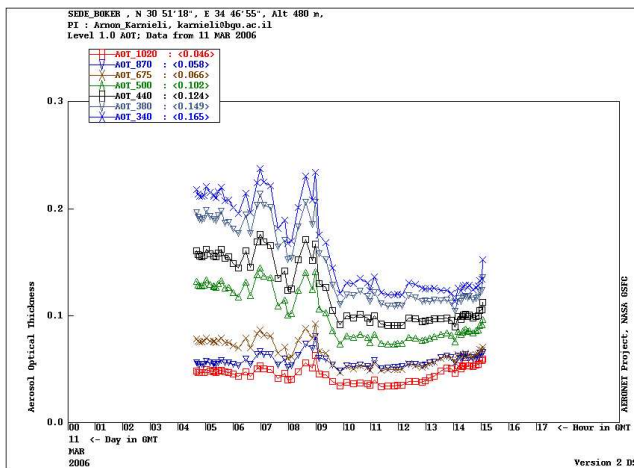
Figure 6.14: Aeronet [left colummn] versus RAMS AOD timeseries, 11 March 2006.

Chapter 7

CASE KU20030225

This is the final of three cases which examines the simulation of dust storms in the Middle East. It is somewhat unique from the previous two in that there are no widespread reports of suspended dust, rather most reports seem to be from more local sources. The majority of reports occurred between 12z 24 February and 00z on 26 February, with some reports continuing until 12z. The model was allowed to run from 00z on 24 February through 12z on 26 February with the first six hours discarded for spinup. Grid 1 is nearly the same as was used in IR20030325, extending from 10°N to 42°N and 31°E to 63°E. Grid 2 is slightly different and is centered over Kuwait and Iraq, with dimensions 25.7°N to 33.8°N and 40.4°E to 49.6°E. These grids are shown in Figure 7.1, superimposed over initial conditions at the model start time.

7.1   Meteorology

Plots of the 1000-500mb thickness and surface wind speed are shown for the start of the analysis time at 06z 24 February, then every 12 hours starting 12z 24 February through 12z 26 February in Figures 7.2 and 7.3. As with the previous two cases, the catalyst for dust mobilization is the passage of a low pressure system north of Iraq and Saudi Arabia. Wind speeds around the Persian Gulf begin to reach speeds of up to 10ms^{-1} by 18z on 24 February and remain between 5 and 10ms^{-1} throughout the rest of the modeled period. RAMS never shows speeds of greater than 15ms^{-1} except for brief periods along the northeast shores of
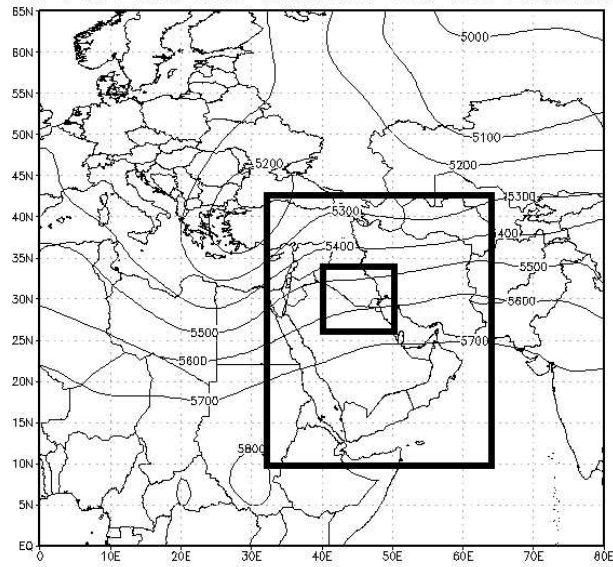
Figure 7.1: Initial Conditions for run KU20030225 00z 24 February, and location of Grids 1 and 2

the Persian Gulf. Thickness and surface wind speed compare well with those from the NCEP reanalysis data except for two instances where high wind speeds are missed; once at 00z on 25 February in the southeast of Saudi Arabia, and once at 18z on the northwest and central Gulf. The latter has greater potential to impact results since it lies over a stronger dust source.

Surface observations show only scattered reports of fog and thunderstorms until 12z on 25 February, when more widespread rain is reported along about 30N through Syria, Western Iran and presumably Iraq, although observations are missing for this period. These persist for the next 12 hours then revert to patchy fog and one report of snow at 12z on the 26 February. There are however many missing reports through Iran on 24 February, when the cold front appears to pass. The most active precipitation in RAMS occurs through this period, and is shown in Figure 7.4. Though widespread through much of the early part of the run, precipitation is not especially intense and rarely exceeds 2mmhr^{-1}. Only light and patchy precipitation is forecast for the remainder of the run, most persistently over Western Syria. It appears that the precipitation accompanying the frontal passage is well-simulated, though missing observations make this statement difficult to verify. Post-frontal precipitation appears to be under-forecast, most notably in areas that reported thunderstorms through the afternoon of 25 February.

Of four stations examined for vertical structure via skewT plots, RAMS performed the best at Tabuk, in Northwestern Saudi Arabia, and relatively poorly at King Fahad International Airport [along the West-Central Persian Gulf] where inversions were consistently missed. Comparisons at Riyadh and Tehran were relatively good, with only one instance of low-level veering missed at each. All stations had very poor reproduction of the dew point structure, indicating either a systematic problem with the RAMS model in this region, the initialization data, or both.
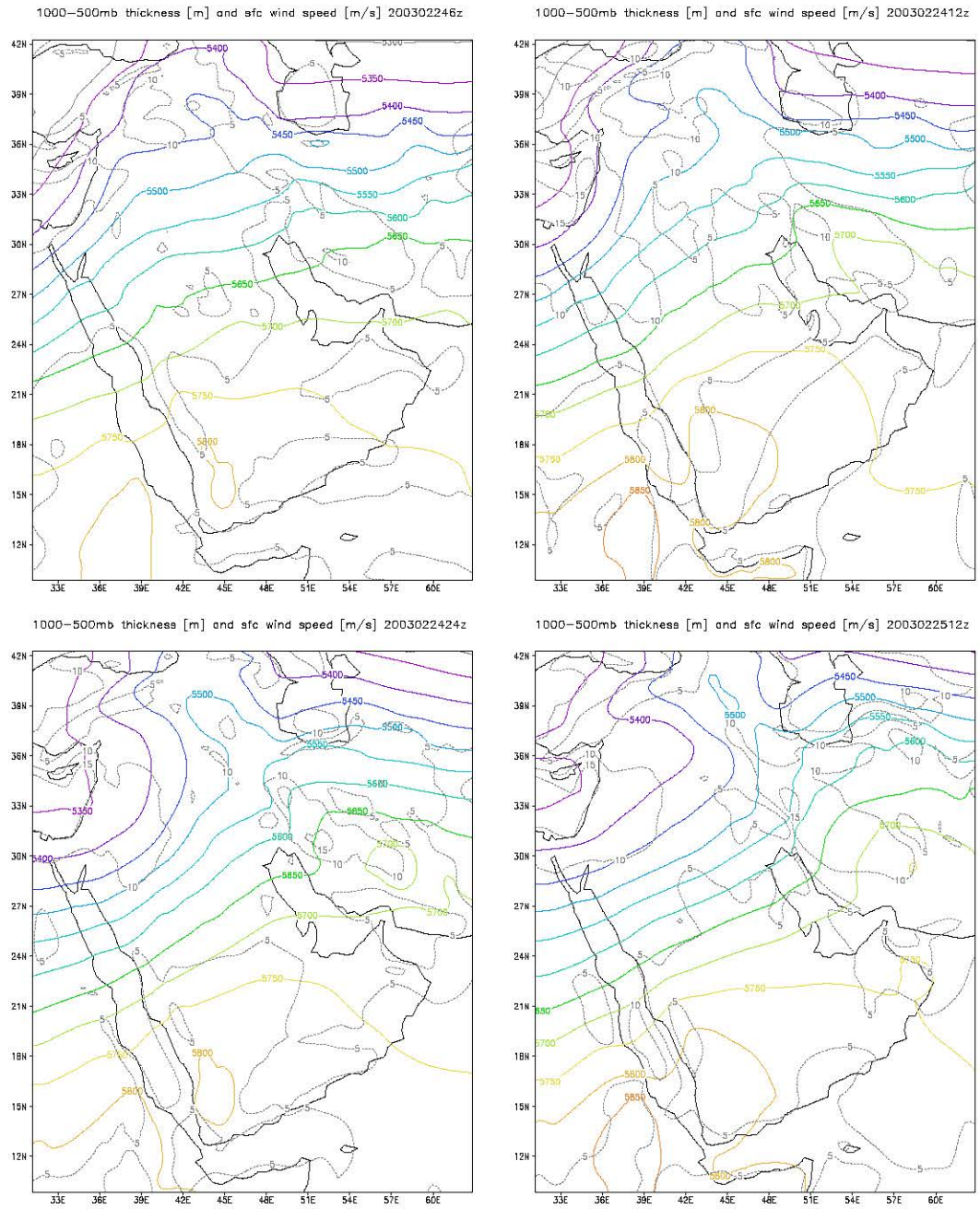
Figure 7.2: 1000-500mb thickness [m] and surface wind speed for the period 06Z 24 February to 12Z 25 February. Temporal progression is left to right, top to bottom.
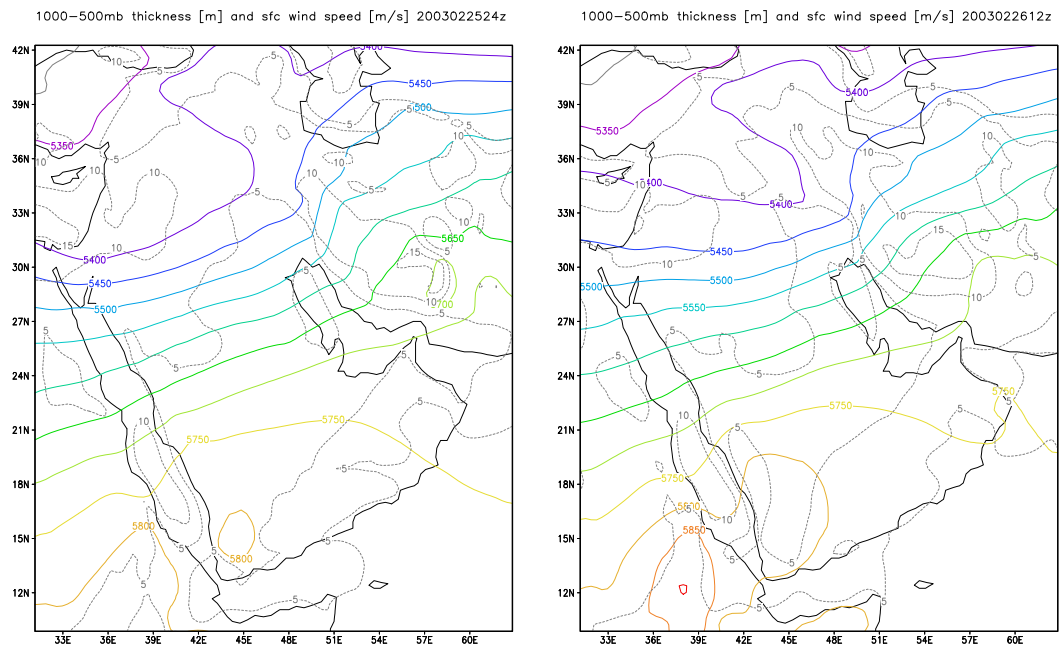
Figure 7.3: 1000-500mb thickness [m] and surface wind speed for the period 00Z to 12Z 26 February.
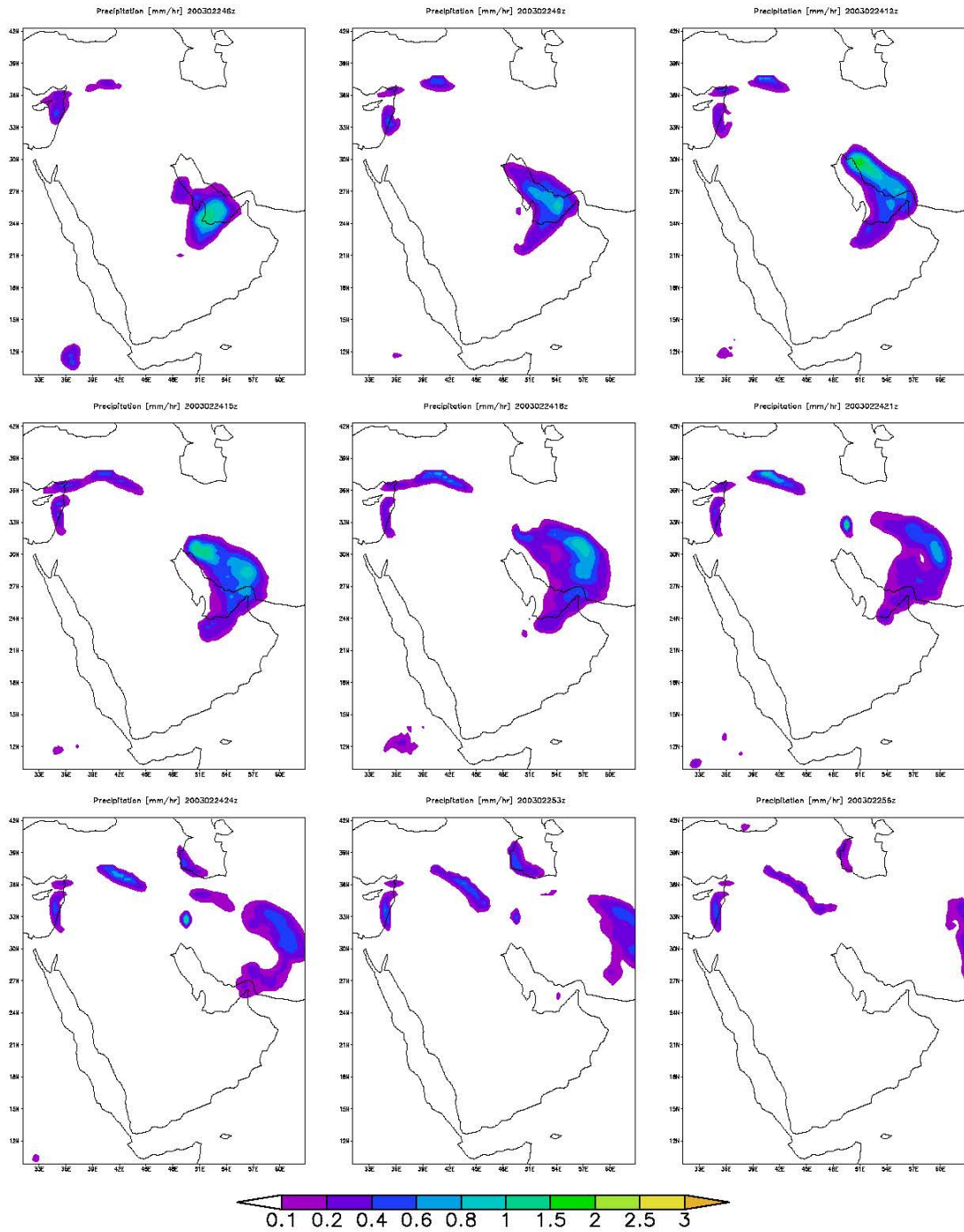
Figure 7.4: Significant model precipitation [mm/hr] - 06z 24 February to 06Z 26 February.

7.2   Model Dust Results

Although many stations report dust on 24 February, few report visibilities. Likewise many archived METARS for the region are either missing or lie outside of the region reporting dust. For this reason only a qualitative comparison can be made between RAMS and ADP surface plots on this day. Two more detailed examinations are made for 06z and 12z on 25 February, when better verification is available.

Figure 7.5 shows side-by side comparisons of surface dust load in grid 1 and surface reports of dust for 24 February. If the threshold for station reporting of dust is assumed to be $500\mu\mathrm{gm}^{-3}$ as it was in previous cases, then RAMS does a good job of simulating the extent of surface dust at 12z in Northeast Saudi Arabia as well as along the West-Central Red Sea. This threshold would result in some of Syria being missed. In addition, missing reports throughout Southeast Saudi Arabia prohibit the verification of the dust forecast over that region. Results at 18z are similarly hard to quantify since many stations are not reporting weather conditions (yellow bars). The area around the Suez Canal and Western Syria has many stations reporting dust, and here RAMS does a good job of matching the observations. Note also that red text does not necessarily imply the presence of dust, only that the visibility is less than 5km, as in the case of Turkey at 18z.

The dust load for 06z 25 February is shown in Figure 7.7 and the corresponding ADP plot is shown in Figure 7.6. The maximum surface load is concentrated over Iraq and Kuwait, with secondary maxima in Southern Saudi Arabia and Syria. The boundary with the area of precipitation can be seen in the low loads wrapping around the North of Syria and Iraq. A small area on Syria's coast has been almost completely washed out. An area of negligible dust load in central Iran is explained by the frontal precipitation that formed a boundary to dust transport from the West through the morning and on the evening of the previous day. Overall, the surface loads match well with the ADP observations. Loads
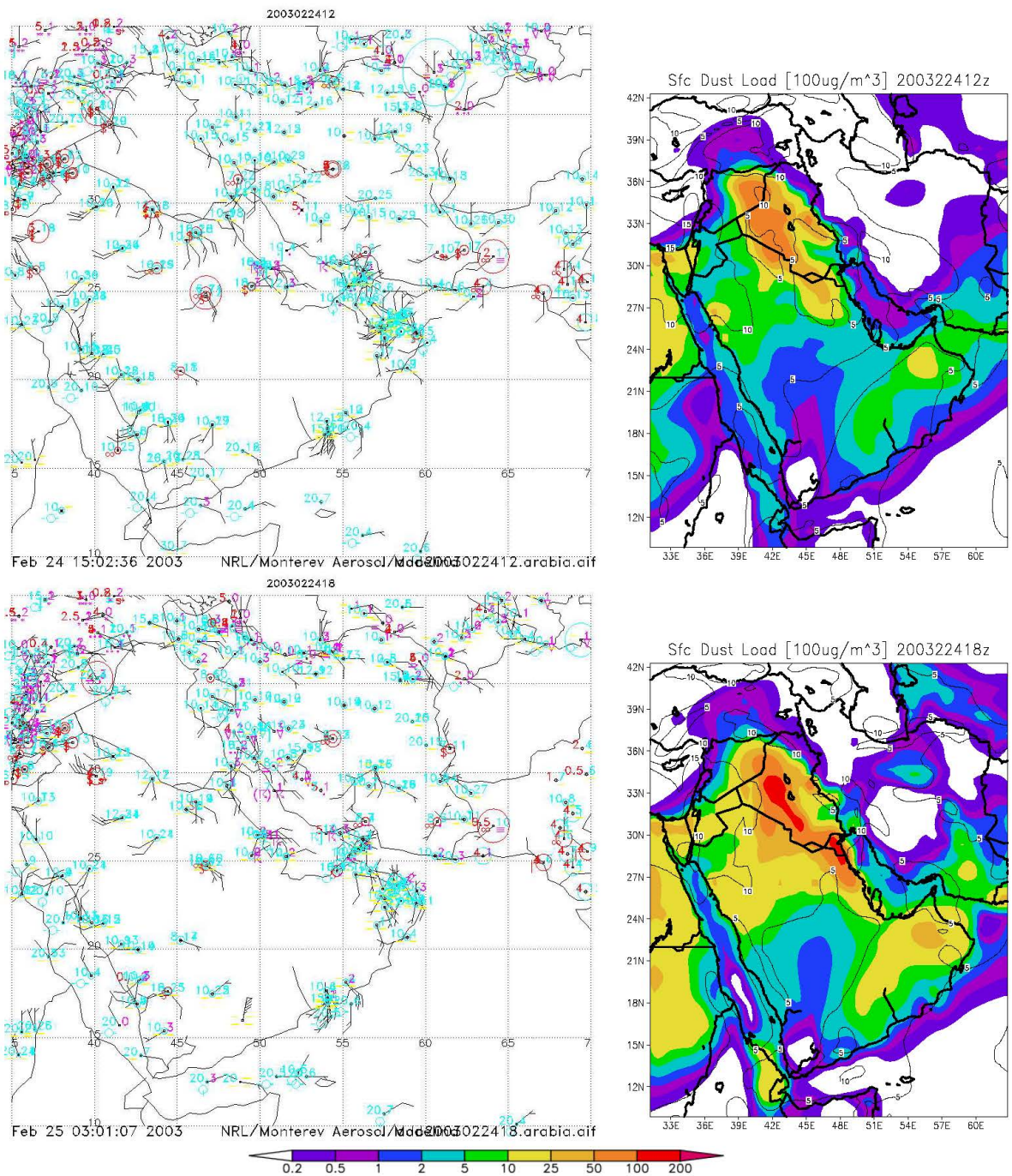
Figure 7.5: Comparison of model dust load and surface observations - 24 February 2003.
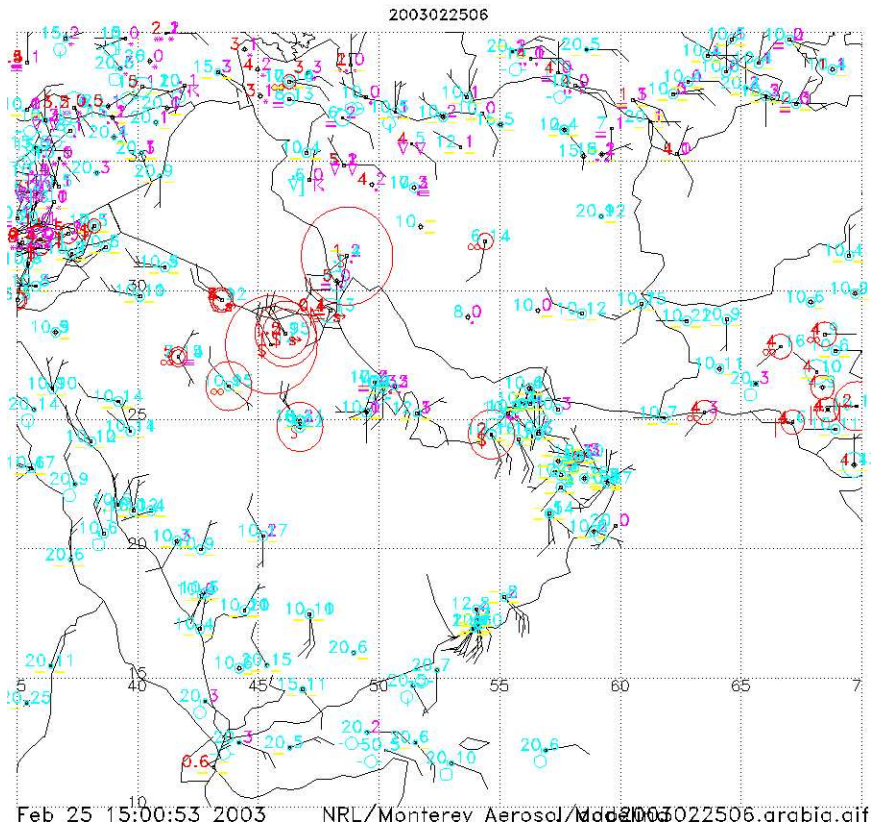
Figure 7.6: ADP Surface observations: 06Z 25 February 2003.

at the 1km generally mirror the areas of high concentration at the surface including the dust-free area over Iran. Relatively high loads are evident are 3km behind the front and in an area of relatively weak precipitation. It is worth emphasizing once again that dust is not scavenged by clouds, so loads co-located with cloud are likely artificially high. The Aeronet back-trajectory data are unavailable for this day however plots from 26 February show that parcels in much of the lower atmosphere passed over the Sahara-Sahel region in the preceding days, so it is possible that transported dust has been missed.

The visibility and optical thickness are shown in Figure 7.8. Two areas of very low visibility are evident: In Iraq this is due to dust load, and in the Gulf of Oman it is caused by a small but dense area of fog. Several smaller areas of restricted visibility north of 36N are due to precipitation in the form of rain, graupel and hail, while the remaining areas
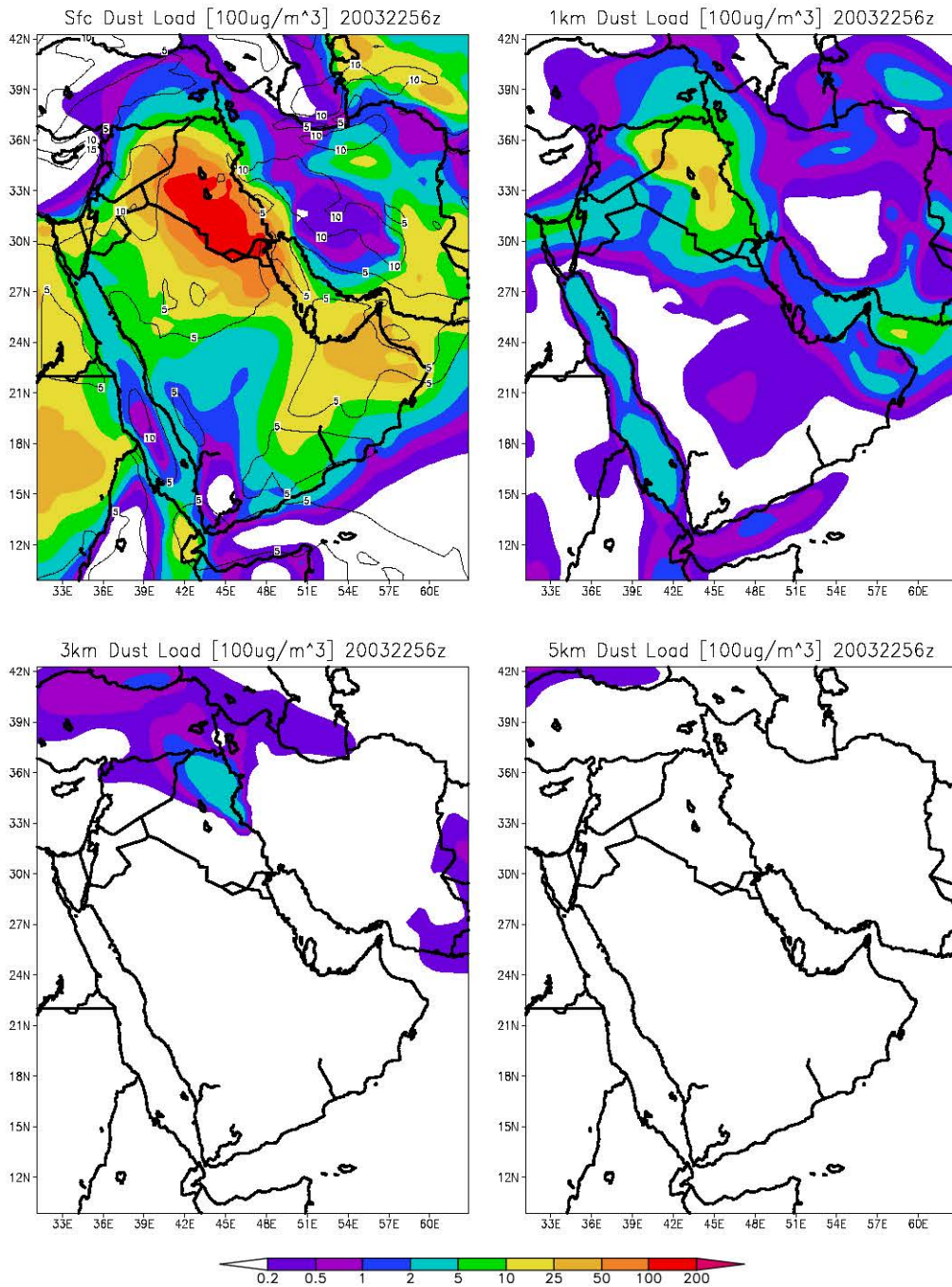
Figure 7.7: Vertical stratification of dust: 06Z 25 February 2003.
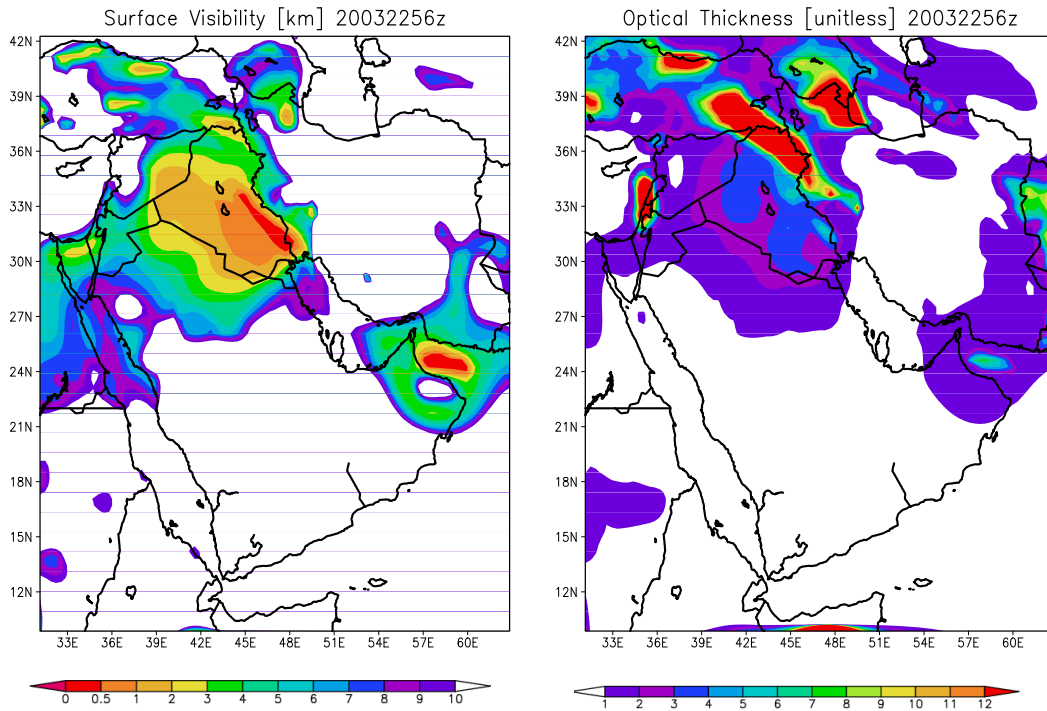
Figure 7.8: Surface visibility and atmosphere optical thickness: 06Z 25 February 2003.

are due to surface dust. A surface report of 0.4km in Kuwait suggests that the area of restricted visibility in Iraq should extend further south. Several stations in Western Iran confirm the fog mentioned above and visibility reports along the Iraq-Saudi Arabian border generally look to be well reproduced by RAMS. Features discussed in the surface visibility also explain the areas of high optical thickness, that is low-lying fog in the Gulf of Oman and areas of cloud and precipitation wrapping around the North of the domain. The same zone of clean air discussed with the dust loads is also very visible in both the visibility and optical thickness plots.

The five point visibility comparison is shown in Figure 7.1. Some observations come from the ADP surface plot, while others are taken from archived airport METARS. The two points in grid 2 greatly overestimate the visibility while two of the three points in grid 1 underestimate the visibility, though only by a factor of about 2. Without surface

Point(grid)	1(2)	2(2)	3(1)	4(1)	5(1)
Lat N	28.3	27.9	30.17	30.6	24.0
Lon E	46.12	45.5	35.8	32.3	54.5
Vis [km]	0.1	1.0	10.0	10.0	2.0
RAMS Vis [km]	4.0	4.2	6.2	3.7	5.3

Table 7.1: Point visibility comparison, RAMS versus observed. 06Z 25 February 2003

observations in Iraq it is difficult to pinpoint the cause of the overestimates in grid 2, however the slight underestimations of surface wind speed through 25 February may have resulted a corresponding underestimate of dust. The widespread nature of the frontal precipitation discussed earlier also leads to the possibility of poor model simulation of timing and/or intensity.

Dust loads for 12z are shown in Figure 7.10. Several differences are evident from the plot at 06z: The aereal extent of high dust loads has diminished at the surface and increased at the 1km layer, indicative of relatively strong vertical motion behind the front. Loads are slightly lower, but still considerable, throughout Iraq. There are also slightly higher loads at 3km and 5km as dust is transported vertically. The dust-free area over Iran is still evident at the surface, though at 1km dust has encroached upon it and it is now an area of maximum load. The corresponding ADP plot is shown in Figure 7.9. The RAMS surface load once again corresponds well with the aereal extent of dust reports.

Surface visibility and atmosphere optical thickness are shown in Figure 7.11. Areas of light precipitation are diminishing visibility over Western Syria and Afghanistan. Overall, all types of precipitation have diminished and reduced visibility is almost entirely attributable to dust. The few reports from the ADP plot suggest that aside from Kuwait, RAMS is significantly overestimating visibility. Areas of high optical thickness correspond very well to areas of high condensate and decreased incoming shortwave radiation, indicating cloud cover. Precipitation has diminished considerably and the dust-free area is still visible in the column optical thickness despite the relatively high dust loads that were evident at
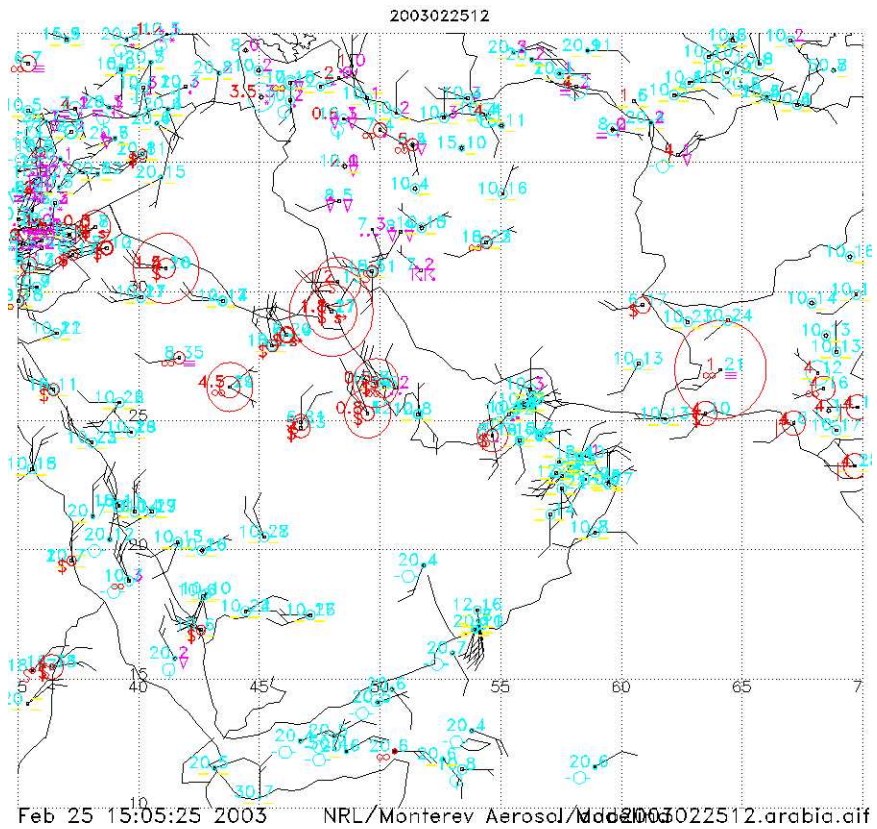
Figure 7.9: ADP Surface observations: 12Z 25 February 2003.
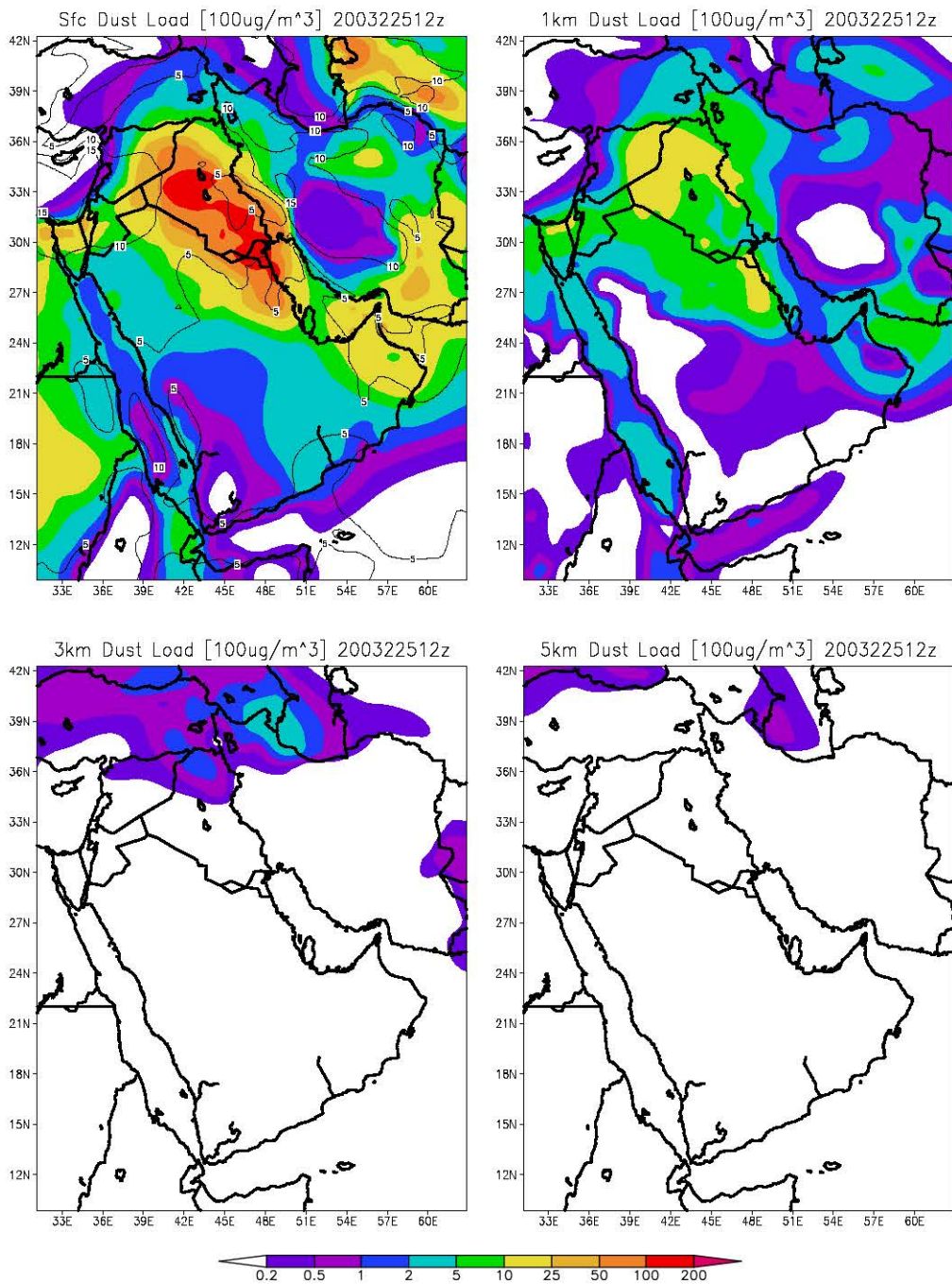
Figure 7.10: Vertical stratification of dust: 12Z 25 February 2003.
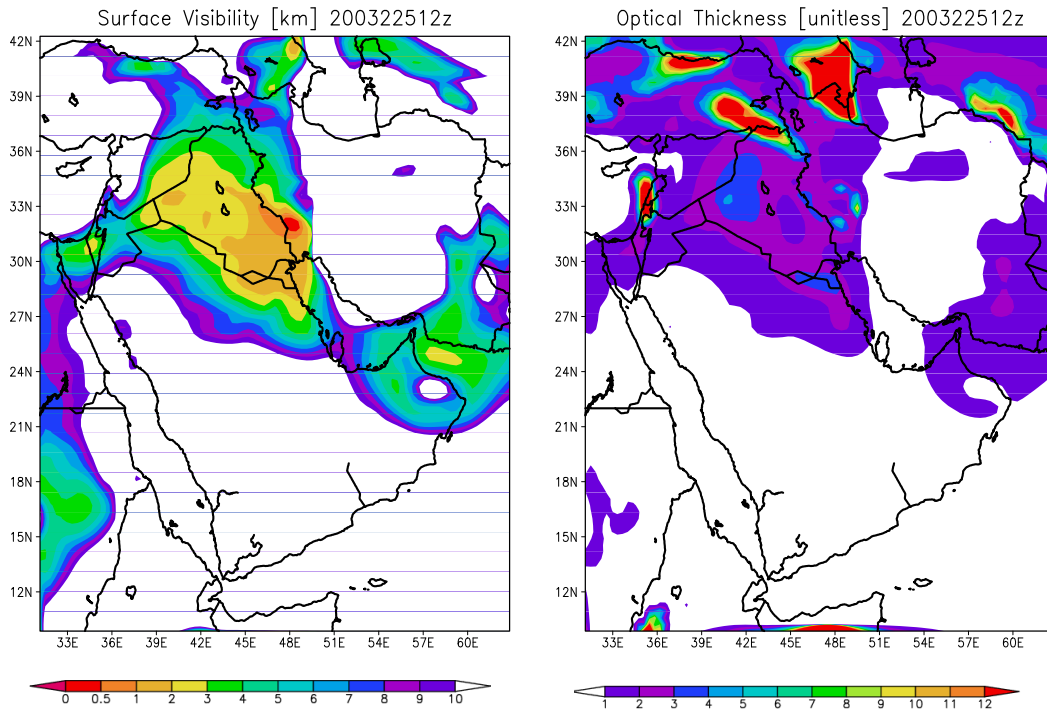
Figure 7.11: Surface visibility, optical thickness and vertical sections: 12Z 25 February 2003.

1km.

Table 7.2 shows the visibility at two points in grid 2 and three points in grid 1. Counter to what was seen in the contour plot, visibility in Kuwait is significantly underestimated, while only one point, near Bahrain, is badly overestimated. Still, by any metric model replication of reported visibility is relatively poor here.

Aeronet plots are only available for the Solar Village site on 24 and 26 February, and comparisons with model optical thickness are shown in Figure 7.2. Model optical thickness

Point(grid)	1(2)	2(2)	3(1)	4(1)	5(1)
Lat N	28.3	27.9	30.17	30.6	25.5
Lon E	46.12	45.5	35.8	32.3	49.5
ADP Vis [km]	7.0	10.0	10.0	3.0	0.8
RAMS Vis [km]	1.9	2.9	6.5	5.2	6.3

Table 7.2: Point visibility comparison, RAMS versus observed. 12Z 25 February 2003

on 24 February remains relatively constant at about 0.6. A sudden drop at about 13z is missed. Because the RAMS radiation band used to calculated optical thickness spans 245-700nm, and optical properties are the arithmetic mean of 100 sub-bands, the 'correct' value for this day lies somewhere between 0.6 and 0.9, which the model slightly underestimates. The comparison for 26 February is fair between 04z and 08z, but RAMS fails to replicate the drop recorded by Aeronet. An examination of dust load and optical thickness plots shows that Solar village is on the edge of a cleaner air mass at both the surface and 1km throughout the morning of 26 February. This mass shows signs of moving out past the station and over the Persian Gulf by 12z, likely leading to a delayed drop in optical thickness had the run continued.
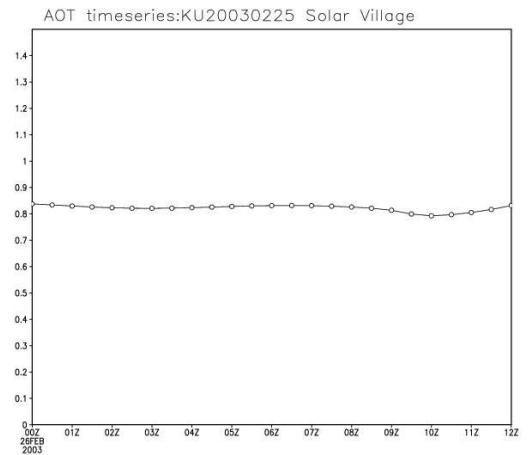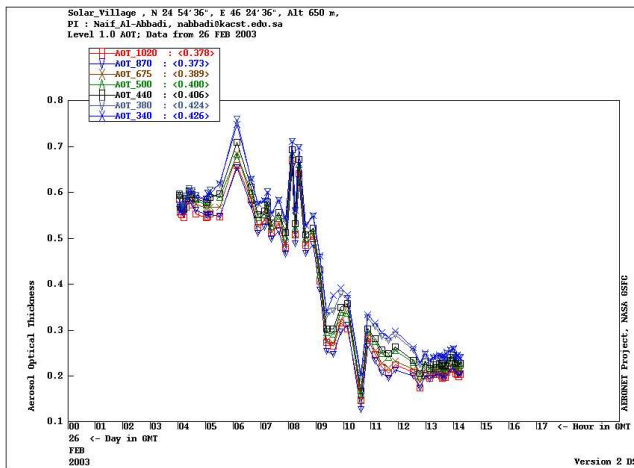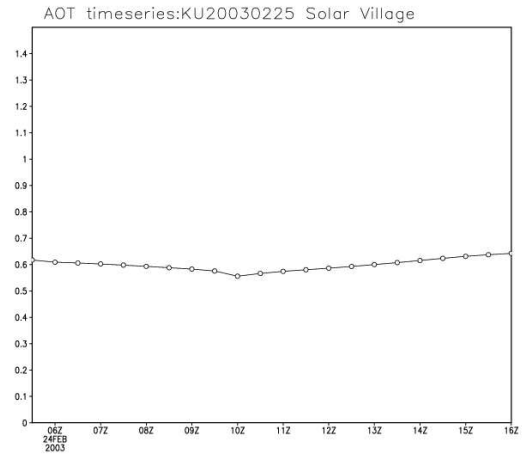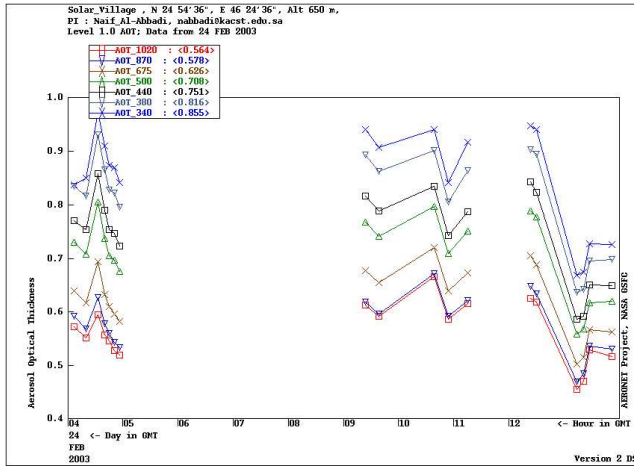
Figure 7.12: Aeronet [left colummn] versus RAMS AOD timeseries, 24 and 26 February 2003.

Chapter 8

CASE SH20000924

This brief final case focuses on the reproduction of a pair of vertical dust profiles that were measured off the West coast of Africa during the Saharan Dust Experiment [SHADE] in September of 2000 [Myhre et al. (2003)]. The goal of the campaign was to investigate how to better model the direct radiative forcing of Saharan dust. To that end a number of parameters were measured concurrently, including radiance along with in-situ sampling of atmospheric dust. Stokowski (2005) made use of a number of these measurements in the validation of the modified Harrington radiation code and in the process adapted a five mode dust distribution to a two mode distribution suitable for use in RAMS. Also examined were a number of measured vertical dust profiles, which were used to initialize RAMS. The purporse of this case is to attempt to replicate these dust profiles using the two mode distribution in place of the default distribution covered in Chapter 2, and to explore the utility of adopting known regional dust parameters.

8.1   Dust Data

The profiles modeled here were measured using the Passive Cavity Aerosol Spectrometer Probe [PCASP] on the UK MET C-130, described in further detail by Haywood et al. (2003). The two 'new' dust modes used in this run are shown in Table 8.1. The seven 'in-situ' size bins used in the RAMS dust subroutine were not modified and although the number fraction for the fitted modes is shown, no constraints were placed on ratios within

	Fraction	r [um]
md1np	94.3%	0.056
md2np	5.7%	0.690

Table 8.1: Two-mode SHADE dust distribution

the model. The dust source function for Northern Africa is shown in Figure 8.1

8.2   Model Setup

RAMS was run for 72 hours, from 00z 23 September through 00z 26 September 2000. Unlike previous cases, three grids were used here; one large coarse grid with 40km spacing and two smaller grids with 10km spacing. This was done because the projected area of dust emission and the area of the vertical dust profiles were quite different, making the use of one finer grid impractical. The three grids are shown in Figure 8.2. There is some difficulty in selecting an appropriate domain that includes the proper source regions. Both the Cape Verde Aeronet site and analysis by Tanré (2003) show very different sources for air parcels between the surface and 5km. The inclusion of all possible origins, both temporal and spatial, would be prohibitively expensive when run on a single PC. The coarse grid in this case includes most possible source regions, but at a lower resolution than would normally be desired. The location of the fine grid over the emission sites amounts to a best guess based on the aforementioned back-trajectories. This illustrates the possible advantage of nesting RAMS within a coarse global dust model, thus avoiding the uncertainty in decision-making.

8.3   Model Meteorology

The synoptic conditions for the period 12z 23 September through 18z on 25 September are shown in Figure 8.3. Unlike previous cases there is no passage of a strong cold front. Wind speeds rarely exceed 10ms^{-1}, the exception being a tongue of strong wind off the West coast at 20N on 25 September. SkewT plots were compared with stations at Dakar, Bamako and Tambacounda, all of which lie in an area extending from $12°N - 15°N$ and
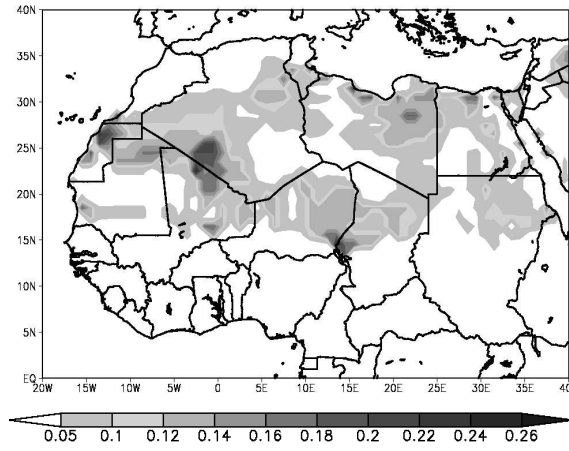
Figure 8.1: Fraction of grid cell acting as a potential dust source.
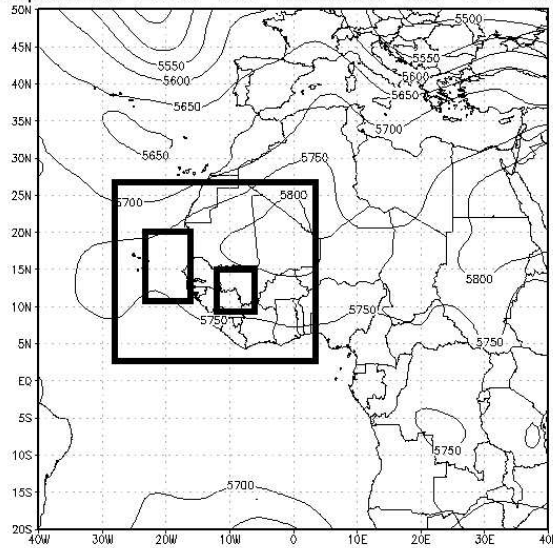
Figure 8.2: Initial Conditions for run SH20000924 00z 23 September and location of Grids.

14°W – 18°W. As with previous cases the temperature and wind profiles were well-modeled while the dewpoint profile showed a significant dry bias. Model precipitation was confined to an area south of the dust sources during 23 and 24 September, but does develop over the sampling area early on 25 September (Figure 8.4), before tapering off in the evening.

8.4   Model Dust results

Figures 8.5 and 8.6 show the 6-hourly progression of dust load at the surface and 1km, 3km and 5km from 12z 24 September through 00z 26 September. The lack of vertical transport compared to other cases is striking, with almost no dust appearing at 3km and none at all at 5km. The only significant loading over the sampling area occurs at the 1km layer, and curls around to the North of the profile locations. The morning precipitation likely plays a role here, though rates were very light.

Figure 8.7 shows a comparison of the measured and modeled dust profiles at 16°N and 21.°W. As can be seen, there is almost no similarity between the two profiles, either in shape or in number concentration. Figure 8.8 shows a comparison of the measured and modeled dust profiles at 115°N and 18°W. As with the profile at 18z the model completely fails to reproduce the observed characteristics. If profiles are shifted North to 18N the concentrations increase somewhat at both times, up to 100cm^{-3}, but the strong maximum above the marine boudnary layer is never reproduced.

8.5   Aeronet Comparison

The only aeronet station lying in the region of interest is at Cape Verde, 16.7°N and 22.9°W. Figure 8.9 shows the comparison between measured and model optical thickness at the site on September 25th. Model values are several orders of magnitude greater than the observed optical thickness. A closer examination of model conditions shows persistant light precipitation over the station throughout the entire day, tapering off at 17z and following
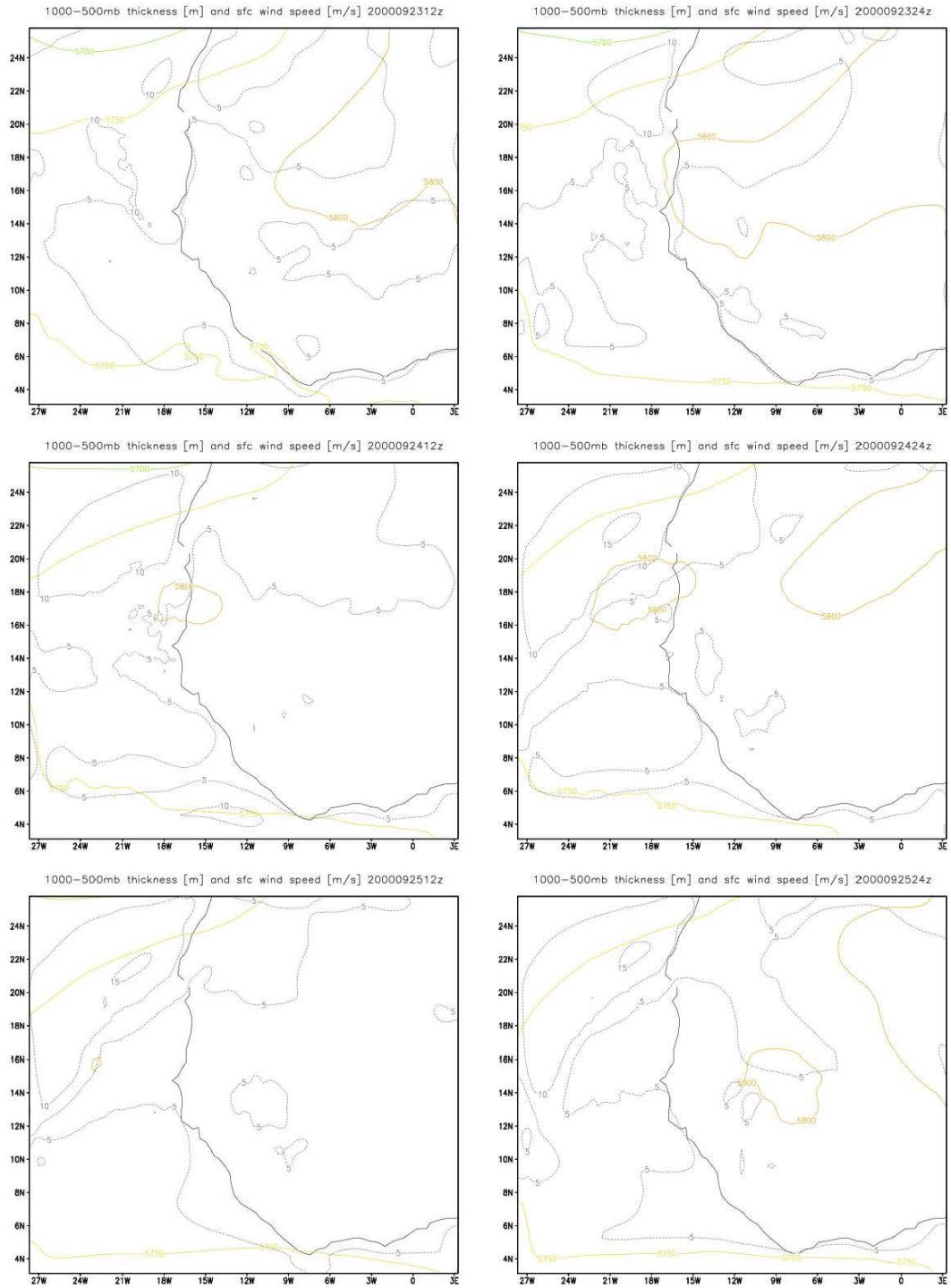
Figure 8.3: 1000-500mb thickness [m] and surface wind speed for the period 12Z September 23 to 00Z September 26 2000. Temporal progression is left to right, top to bottom.
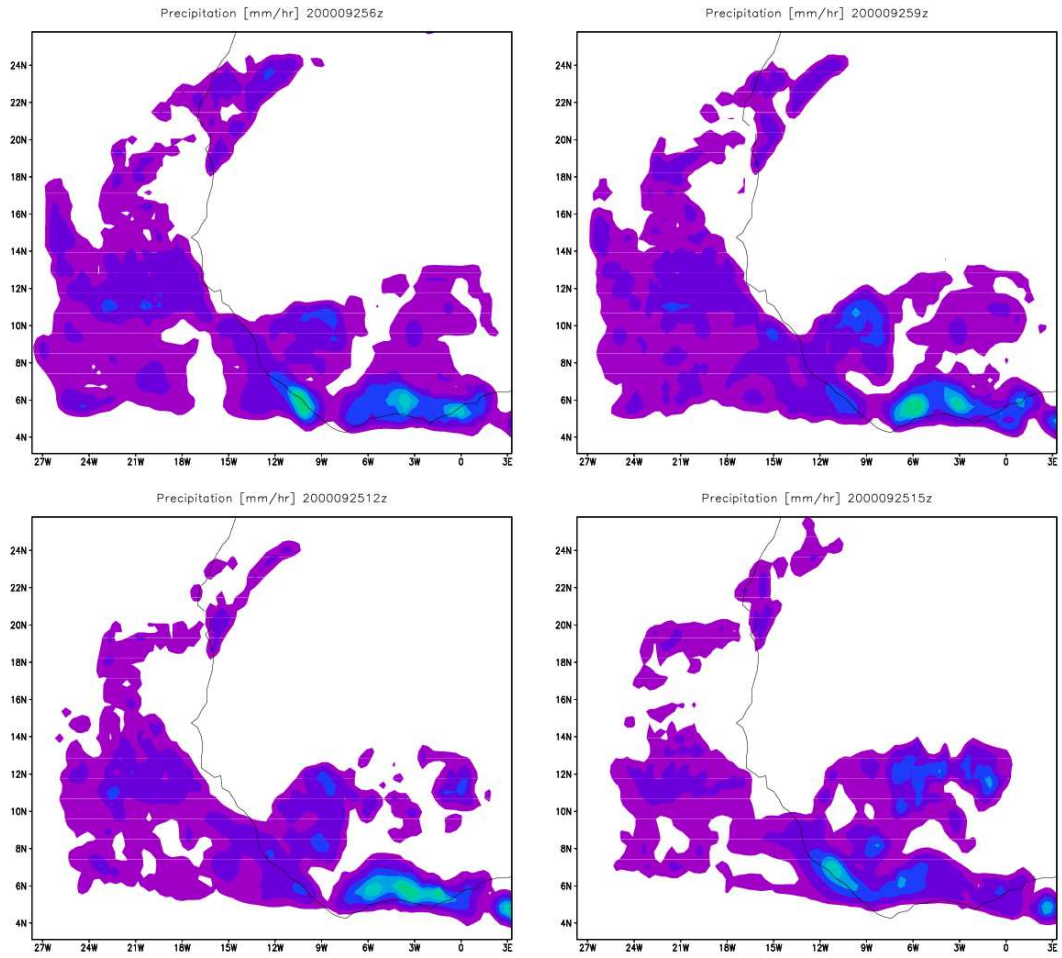
Figure 8.4: Precipitation over the dust sampling area, 06Z to 15Z on 25 September 2000.
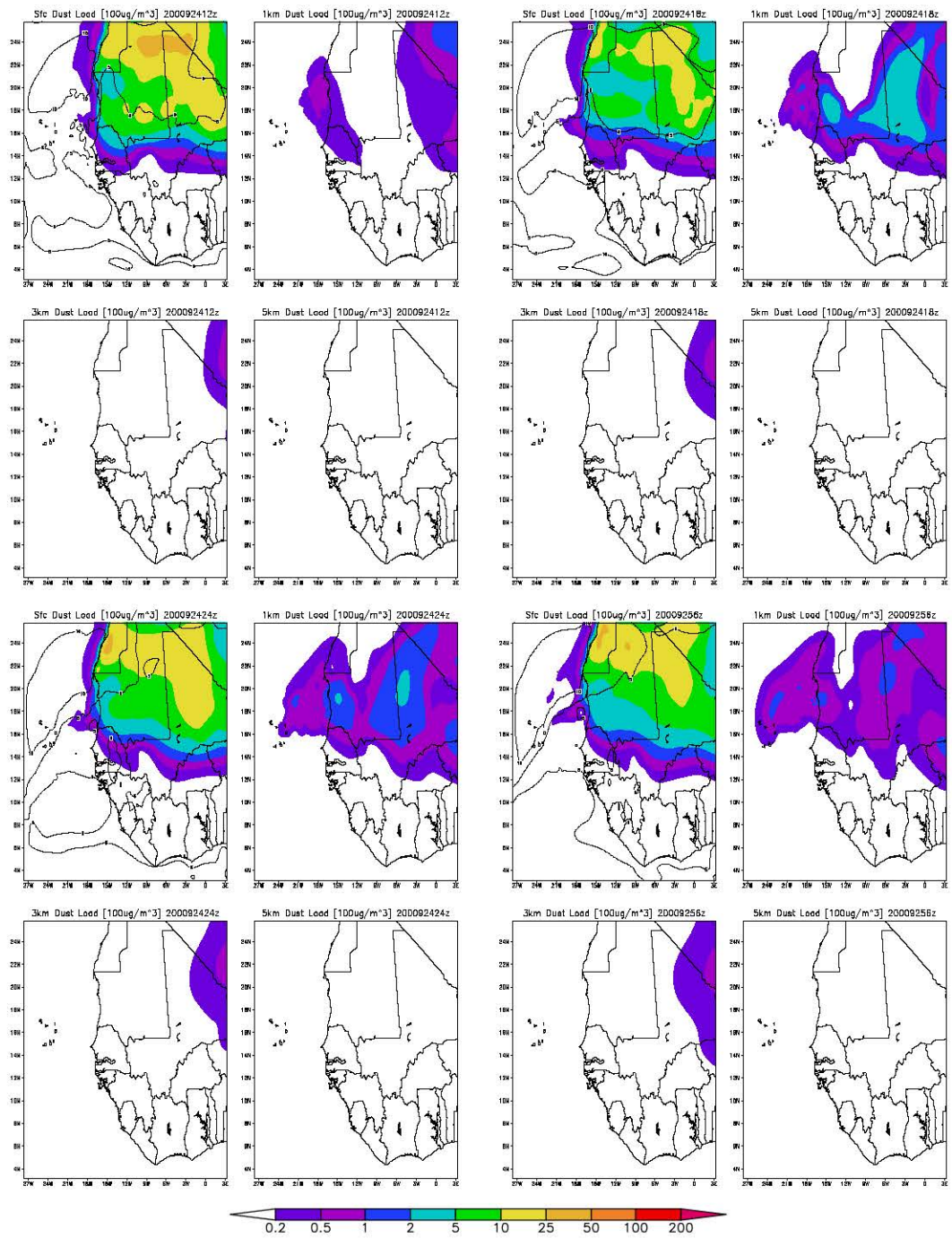
Figure 8.5: Dust uplift and transport: 12Z 24 September to 06Z 26 September.
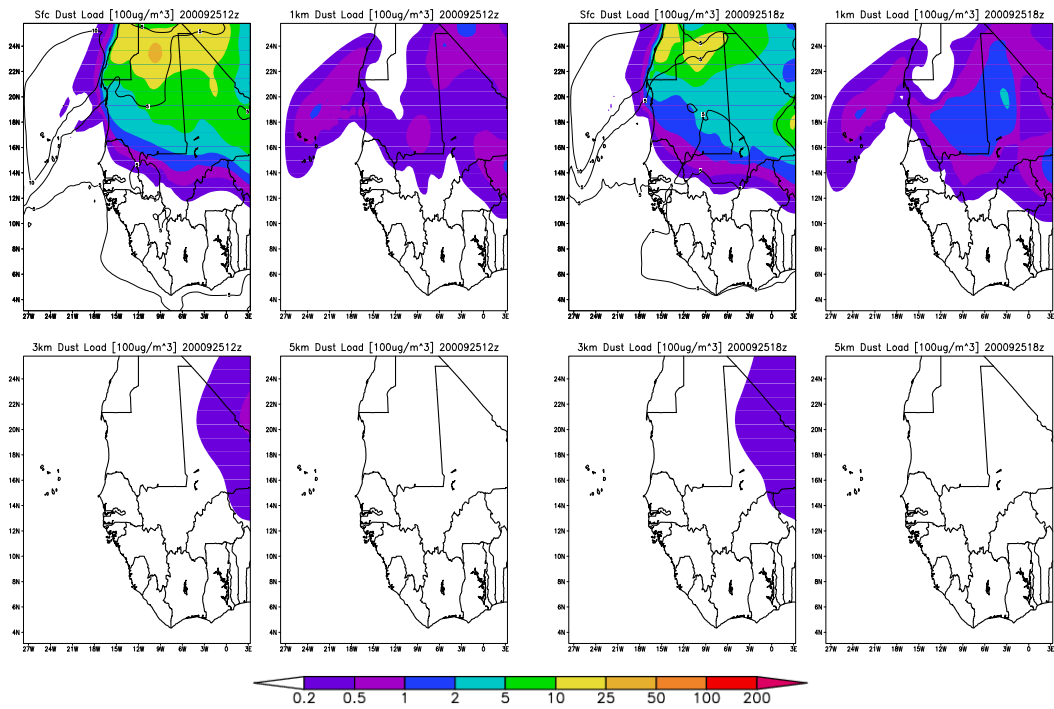
Figure 8.6: Dust uplift and transport: 12Z to 18Z 25 September.
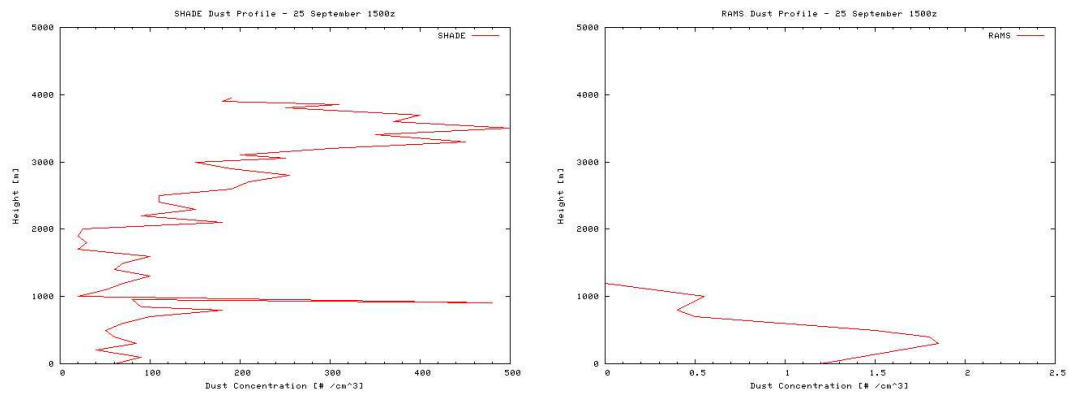
Figure 8.7: Comparison of SHADE and RAMS vertical dust profiles, 25 September 15Z

114
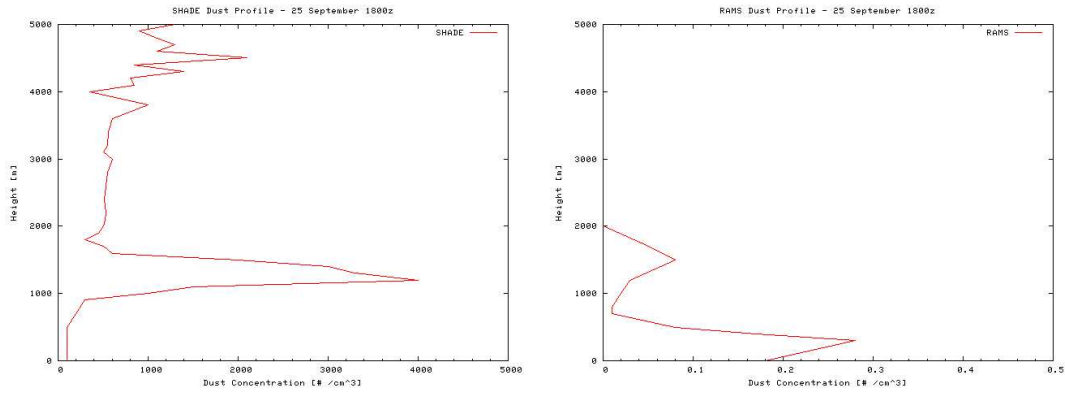
Figure 8.8: Comparison of SHADE and RAMS vertical dust profiles, 25 September 18Z

by a fog or cloud bank extending from the surface up to 1200m. Neither the large values or the sudden increase around 17z are seen in the Aeronet plot, suggesting that RAMS has overpredicted cloud and precipitation in this area.

Overall, RAMS did an extremely poor job of simulating observed dust profiles and optical thickness for this case. The latter is explained, at least in part, by a poor forecast of the extent of cloud and precipitation. The dust profiles bear no similarity to what was observed, even when model dust radii are changed to match those found during SHADE. After examining the results, the case was re-run using default dust parameters, yielding similarly poor performance. There are several possible explanations for this poor performance: A flaw in the dust parameterizations would naturally cause a poor fit between observations and model results, however performance over the Middle East was relatively good. This leaves only the assumed in-situ distribution or dust source function as culprits. The distribution of precipitation over the profile sites is likely partly to blame however even in areas with no precipitation, dust concentrations never exceeded $100 cm^{-3}$. Terrain over much of the source region is complex, not the ideally flat and homogenous environment that is implicitly assumed. Inadequate resolution of terrain may play a role in the poor simulation of dust in this case. The last possibility is a flaw with the model setup. The
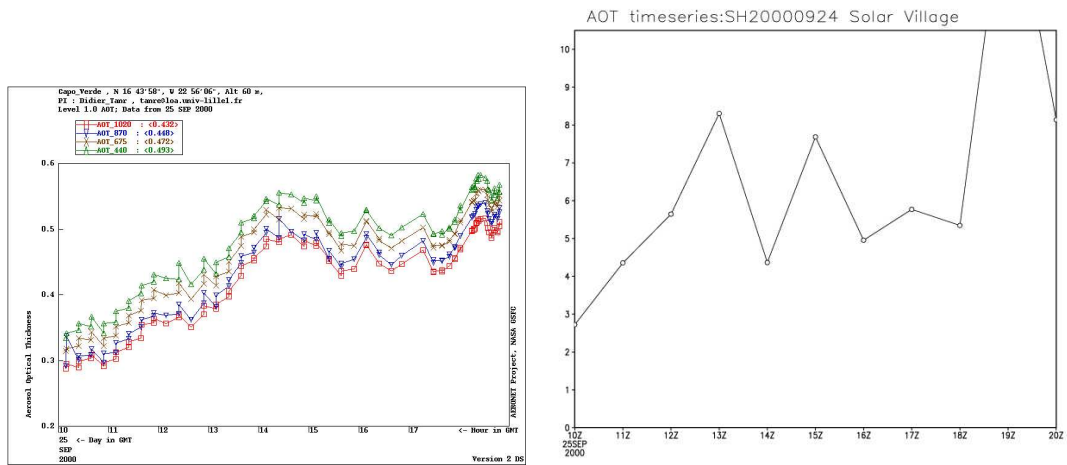
Figure 8.9: Aeronet [left column] versus RAMS AOD timeseries, 25 September 2000.

back-trajectories mentioned earlier suggest that to capture all possible emissions, a 7-10 day simulation would be required over a larger domain than was used here. Given the computational constraints of this study, such a run was not practical however this is somthing that could be examined in the future.

Chapter 9

CONCLUSIONS AND SUGGESTIONS FOR FUTURE WORK

A new dust emission module has been added to RAMS. This allows for the prediction of dust aerosol loads and interacts with the existing radiation module to diagnose an isotropic visibility. Possible applications include local visibility forecasts for the military and civilian sectors, air quality forecasting as well as higher-resolution studies of the impacts on microphysical processes. The module has been added in such a way that further modifications and additions may be made with relative ease.

9.1   Summary of Work

RAMS was modified with the addition of a dust source and deposition module, allowing dust to be emitted from pre-defined dust sources, and to settle or wash out of the atmosphere. This complements the work of Stokowski (2005) in that allowing dust to be emitted, rather than specifying a constant profile or homogeneous concentration, allows the effects of dust on the atmosphere to be studied in a more realistic environment. Sources are defined as the percentage of a grid that is able to emit dust, and a 7-bin in-situ distribution is defined. Once lofted the distribution is reduced to two bins, where they are advected through the model in the horizontal and vertical directions. Either of the binned parameters may be easily modified to suit a specific known distribution. Dust is removed from the atmosphere through dry deposition, gravitational settling or rain scavenging. Cloud scavenging is not active as present studies do not provide for a suitable parameterization

for use in the RAMS model.

RAMS was first tested in a variety of configurations in order to identify which user-specified variables are most critical when designing a run. This information allows for the best balance between accuracy and computational time required, as unnecessary features that provide no increase in accuracy are avoided. It was found that with the current version of RAMS, the only parameter of critical importance was the vertical grid spacing. Once sensitivity testing was concluded, a series of cases were studied in order to evaluate real-world performance. A variety of criteria were examined, including success in reproducing observed meteorology, visibility and optical thickness. A consistent problem throughout this phase was a lack of verification data. For this reason, no specific metric was used to judge the overall success or failure of RAMS in reproducing a dust event. Some quantitative comparisons were possible but for the most part evaluation was qualitative.

9.2   Conclusions

Based on the cases that were examined in this study, it appears that the newest version of RAMS is capable of modeling dust emission and its effects on visibility. Several problems were identified, most noticeably the persistent dry bias in all runs, and at all stations. There are several possible causes for this, but no definitive solution was found. The spatial extent of precipitation was underpredicted on several occasions thereby impacting the accuracy of model results by allowing high concentrations of dust to remain in the atmosphere. The choice of convective parameterization emerged as being important with regards to resolved surface precipitation; the Kain-Fritsch scheme led to a noticeable increase in vertical dust transport and in some cases improved the modeling of surface precipitation. Smaller-scale problems included the failure to resolve inversions or other boundary layer features. A strong inversion can delay strong winds or even suppress dust production altogether along with impacting the distribution of moisture in the lower atmosphere.

When attempting to model an historic dust event, it is important to consider the time required for dust to be lofted into the atmosphere. In the present study, an effort was made to select events where local dust sources dominate, thereby shortening the spinup time. If any transport is required, appropriate consideration must be given not only to the transport time, but the time for dust reach levels where its residence time is sufficient for long term transport. An example of where this was a likely source of error was case SH20000924, where model results completely failed to mimick reality. The back-trajectory plots that were used in the evaluation of the case studies are one useful tool for helping to determine an appropriate lead time.

Visibility was generally predicted within a factor of 5 or less in both grids. Moreover, the higher ratios in the fine grid 2 usually entailed relatively small absolute errors. There appears to be an advantage to running the model on a fine scale if point forecasts of visibility are desired, as contoured maps at times obscured the results. Though it was not examined in detail, the choice of convective parameterization schemes had little effect on the accuracy of the surface visibility. As was shown in Chapter 3, there is presently no distinct advantage to a 3rd nested grid, but if resolution is increased for the dust source function, topography or vegetation this option should be explored. With the limited validation tools available, RAMS did a good job at predicting the aereal extent of dust at the surface. Column optical thickness was also generally well-resolved, though at times features such as a sudden rise or drop were missed. Some of the errors were attributable to poor resolution of precipitation, such that dust load was subsequently overforecast. Others were due to the late passage of dust-laden air such as during KU20030225.

With the exception of case SH20000924, the new dust module shows promise for deployment in areas where its features such as high resolution, detailed microphysics scheme and radiatively active aerosols are desirable. The structure of the module allows for the modification of dust characteristics with relative ease, making it tuneable for a specific

119

region.

9.3   Suggestions for Future Work

Although RAMS performed well in this study, there are a number of ways to improve upon the current configuration, based on results presented here and also from information in recent literature. Firstly, although a brief look was given to radiative effects on precipitation, a more detailed study should be undertaken on a 3D cloud-resolving scale. Results presented here relied on convective parameterization and are not the best indicator of dust effects on relative humidity or convective initiation. This was also noted by Stokowski (2005), who examined radiative effects in a 2D LES configuration.

The dust source function used in this study was designed for use on a global scale, and does not account for dust emission from farming or industrial activities. Though much debate remains on the relative importance of such emissions, there is no doubt that they have the potential to affect atmospheric processes on regional scales. As was mentioned in Chapter 1, there are regional dust source models under development or already available, and the use of these would likely improve model performance. In addition, adding at least one, or possibly several more dust size bins to the two already in existence would likely improve the model accuracy. The paradigm that was used in the implementation of the current bin design assumes that the only particles of consequence are those with an atmospheric residence time of greater than several hours. On the local scale this is not true, and larger particles do likely play a role in creating extremely low visibility events. More bins may also help to improve cases where transport far beyond the source region occurs.

There are several variables that exist internally within RAMS, but are not available as model output. These include the single scatter albedo, the asymmetry parameter and the extinction coefficient. Making these available would serve to increase the potential pool of validation sources and would also facilitate the further validation of the aerosol radiation

120

module. Additionally, the addition of dry and wet deposition variables could be of interest if RAMS was to be coupled with a more involved ocean or terrestrial model.

Finally, the logical next step in the development is to allow dust to be microphysically active within the model. As was discussed at some length in Chapter 1, there is little doubt that atmospheric dust has the ability to influence cloud development, glaciation and precipitation rates, however the implementation of such a scheme in RAMS is not a trivial matter. Nevertheless, the inability of these particles to act as CCN, GCCN or IN constitutes another source of potential error in the model.

BIBLIOGRAPHY

Baron, P. A., and K. Willeke, 2001: *Aerosol measurement: Principles, techniques and applications. Second Edition.*. Wiley-Interscience Inc.

Bergametti, G., 1998: Mineral aerosols: Renewed interest for climate forcing and tropospheric chemistry studies. *IGACtivities Newsletter*, **1**, 13–17.

Brooks, N., 2000: Dust-climate interactions in the Sahel–Sahara zone of Northern Africa, with particular reference to late twentieth century Sahelian drought. Ph.D. thesis, Climatic Research Unit, University of East Anglia, Norwich.

Chylek, P., and Coauthors, 2006: Aerosol indirect effect over the indian ocean. *Geophys. Res. Letters*, **33**.

Cotton, W., and Coauthors, 2003: Rams 2001: Current status and future directions. *Meteo and Atmos. Phys.*, **82**, 5–29.

Davies, H. C., 1983: Limitations of some common lateral boundary schemes used in regiona nwp models. *Mon. Wea. Review*, **111**, 1002–1012.

DeMott, P. J., K. Sassen, M. R. Poellot, D. Baumgardner, D. C. Rodgers, S. D. Brooks, A. J. Prenni, and S. M. Kreidenweis, 2003: African dust aerosols as atmospheric ice nuclei. *Geophys. Res. Letters*, **30**.

Falkovich, A. H., E. Ganor, Z. Levin, P. Formenti, and Y. Rudich, 2001: Chemical and mineralogical analysis of individual mineral dust particles. *J. Geoph. Res.*, **106**, 18,029–18,036.

Fan, S.-M., L. W. Horowitz, H. L. II, and W. J. Moxim, 2004: Impact of air pollution on wet deposition of mineral dust. *J. Geoph. Res.*, **31**.

Formenti, P., W. Elbert, W. Maenhaut, J. Haywood, and M. Andreae, 2003: Chemical composition of mineral dust aerosol during the saharan dust experiment (shade) airborne campaign in the cape verde region, september 2000. *J. Geoph. Res.*, **108**.

Gillette, D. A., and R. Passi, 1988: Modeling dust emission caused by wind erosion. *J. Geoph. Res.*, **93**, 14,233–14 242.

Ginoux, P., M. Chin, I. Tegen, J. M. Prospero, B. Holden, O. Dubovik, and S.-J. Lin, 2001: Sources and distributions of dust aerosols simulated with the gocart model. *J. Geoph. Res.*, **106**, 20,255–20,273.

Gong, S., X. Y. Zhang, T. L. Zhao, I. G. McKendry, D. A. Jaffe, and N. M. Lu, 2003: Characterization of soil dust aerosol in china and its transport and distribution during 2001 ace-asia: 2. model simulation and validation. *J. Geoph. Res.*, **108**.

Hansen, J., M. Sato, and R. Ruedy, 1997: Radiatve forcing and climate response. *J. Geoph. Res.*, **102**, 6831–6864.

Harrington, J., 1997: The effects of radiative and microphysical processes on simulated warm and transition season arctic stratus. Ph.D. thesis, Colorado State University.

Haywood, J., P. Francis, S. Osborne, M. Glew, N. Loeb, and E. Highwood, 2003: Radiative properties and direct radiative effect of saharan dust measured by the c-130 aircraft during shade: 1. solar spectrum. *J. Geoph. Res.*, **108**.

IAPSAG, 2006: Aerosol Cloud-Precipitation Interaction: Facts and Fiction. *AGU Fall Meeting Abstracts*.

IPCC, 2001: 2001 third assessment report: Climate change 2001, the scientific basis. Cambridge University Press.

Iverson, J. D., and B. R. White, 1982: Saltation threshold on earth, mars and venus. *Sedimentology*, **29**, 111–119.

Johnson, B., K. Shine, and P. Forster, 2004: The semi-direct-aerosol effect: Impact of absorbing aerosols on marine stratocumulus. *Q. J. R. Metoerol. Soc.*, **130**, 1407–1422.

Karyampudi, V., and T. Carlson, 1988: Analysis and numerical simulations of the saharan air layer and its effect on easterly wave disturbances. *J. App. Meteo.*, **45(21)**, 3102–3136.

Klemp, J. P., and R. B. Wilhelmson, 1978: The simulation of three-dimensional convective storm dynamics. *J. Atmos. Sci.*, **35**, 1007–1096.

Kuciauskas, A. P., S. Miller, and D. Westphal, 2003: Tactical application of a satellite-derived optical depth product during dust storm events in support of operation iraq freedom. *Proceedings from the Battlefield Atmospheric and Cloud Impacts of Military Operations (BACIMO) Conference, Monterey, CA, 9-11 Sept. 2003*, 1–10.

Lacis, A. A., and M. I. Mishchenko, 1994: Climate forcing, climate sensitivity, and climate response: a radiative modeling perspective on atmospheric aerosols. R. J. Charlson and J. Heintzenberg, Eds., *Aerosol Forcing of Climate: Report of the Dahlem Workshop on Aerosol Forcing of Climate, Berlin 1994, April 24-29.*, 11–42.

Levin, Z., E. Ganor, and V. Gladstein, 1996: The effects of desert particles coated with sulfate on rain formation in the eastern mediterranean. *J. App. Meteo.*, **35**, 1511–1523.

Levin, Z., A. Teller, and E. Ganor, 2005: On the interactions of mineral dust, sea salt particles and clouds: A measurement and modeling study from the mediterranean israeli dust experiment campaign. *J. Geoph. Res.*, **110**.

Mahowald, N., and Coauthors, 2005: The atmospheric global dust cycle and iron inputs to the ocean. *Global Biogeochem. Cycles*, **19**.

Mahowald, N., K. Kohfeld, M. Hansson, Y. Balkanski, S. P. Harrison, I. C. Prentice, M. Schulz, and H. Rodhe, 1999: Dust sources and deposition during the last glacial maximum and current climate: A comparison of model results with paleodata from ice cores and marine sediments. *J. Geoph. Res.*, **104**, 15,895–15,916.

Mahrer, Y., and R. A. Pielke, 1977: A numerical study of the airflow over irregular terrain. *Beiträge zur Physik der Atmosphäre*, **50**, 98–113.

Marticorena, B., and G. Bergametti, 2005: Modeling the atmospheric dust cycle: 1. design of a soil-derived dust emission scheme. *J. Geoph. Res.*, **100**, 16,415–16,430.

Mbourou, G. N., J. Bertrand, and S. Nicholson, 1997: The diurnal and seasonal cycles of windborne dust over africa north of the equator. *J. App. Meteo.*, **36**, 868–882.

Meloni, D., A. di Sarra, T. D. Iorio, and G. Fiocco, 2004: Direct radiative forcing of saharan dust in the mediterranean from measurements at lambedusa island and MISR space-borne observations. *J. Geoph. Res.*, **109,D08206**.

Miller, R., I. Tegen, and J. Perlwitz, 2005: Surface radiative forcing by soil dust aerosols and the hydrologic cycle. *J. Geoph. Res.*, **109**.

Myhre, G., A. Grini, J. M. Haywood, F. Stordal, B. Chatenet, D. Tanré, J. K. Sundet, and I. S. Isaken, 2003: Modeling the radiative impact of mineral dust during the saharan dust experiment (shade) campaign. *J. Geoph. Res.*, **108**.

Myhre, G., and F. Stordal, 2001: Global sensitivity experiments of the radiative forcing due to mineral aerosols. *J. Geoph. Res.*, **106**, 18,193–18,204.

Nicholson, S., 2000: Land surface processes and Sahel climate. *Rev. Geophys.*, **38**, 117–139.

Nickovic, S., G. Kallos, A. Papadopoulos, and O. Kakaliagou, 2001: A model for prediction of desert dust cycle in the atmosphere. *J. Geoph. Res.*, **106**, 18,113–18,129.

O'Dowd, C. D., J. A. Lowe, and M. H. Smith, 2003: Coupling sea-salt and suphate interactions and its impact on could droplet concentration predictions. *J. Geoph. Res.*, **26**, 1311–1314.

Overpeck, J., D. Rind, A. Lacis, and R. Healy, 1996: Possible rolse of dust-induced regional warming in abrpt climate change during the last glacial period. *Nature*, **384**, 447–449.

Perry, K., T. Cahill, R. Eldred, and D. Dutcher, 1997: Long-range transport of north african dust to the eastern united states. *J. Geoph. Res.*, **102**, 11,225–11,238.

Pielke, R. A., and Coauthors, 1992: A comprehensive meteorological modeling system - RAMS. *Meteol. Atmos. Phys.*, **49**, 69–91.

Prospero, J., 1999: Long-term measurement of the transport of african mineral dust to the southeastern united states: Implications for regional air quality. *J. Geoph. Res.*, **104**, 15,917–15,927.

Prospero, J. M., P. Ginoux, O. Torres, S. E. Nicholson, and T. E. Gill, 2002: Environmental characterization of global sources of atmospheric soil dust identified with the numbus 7 total ozone mapping spectrometer (toms) absorbing aerosol product. *Rev. Geophys.*, **40**.

Rosenfeld, D., Y. Rudich, and R. Lahav, 2001: Desert dust suppressing precipitation: A possible desertification feedback loop. *Proceedings of the National Academy of Sciences*, **98**, 5975–5980.

Sassen, K., 2002: Indirect climate forcing over the western US from asian dust storms. *Geophys. Res. Letters*, **29**.

Sassen, K., P. Demott, J. Prospero, and M. Poellot, 2003: Saharan dust storms and indirect aerosol effects on clouds: Crystal-face results. *Geophys. Res. Letters*, **30**.

Slinn, S., and W. G. N. Slinn, 1980: Predictions for particle deposition on natural waters. *atenv*, **14**, 1013–1016.

Stokowski, D. M., 2005: The addition of the direct radiative effect of atmopsheric aerosols into the regional atmospheric modeling system (RAMS). Master's thesis, Colorado State University Department of Atmospheric Science, Fort Collins, CO.

Tang, Y., and Coauthors, 2003: Impacts of aerosols and clouds on photolysis frequencies and photochemistry during trace-p: 2. three-dimensional study using a regional chemical transport model. *J. Geoph. Res.*, **108(D21)**.

Tanré, D., 2003: Measurement and modeling of the saharan dust radiative impact: Overview of the saharan dust experiment (SHADE). *J. Geoph. Res.*, **108(D18)**.

Tegen, I., and I. Fung, 1994: Modeling of mineral dust in the atmosphere: Sources, transport and optical thickness. *J. Geoph. Res.*, **99**, 22,897–22,914.

Tegen, I., M. Werner, S. P. Harrison, and K. E. Kohfeld, 2004: Relative importance of climate and land use in determining present and future global soil dust emission. *Geophys. Res. Letters*, **31,L05105**.

Tratt, D. M., R. J. Frouin, and D. L. Westphal, 2001: April 1998 asian dust event: A southern california perspective. *J. Geoph. Res.*, **106**, 18,371–18,379.

Tremback, C. J., 1990: Numerical simulation of a mesoscale convective complex: Model development and numerical results. Ph.D. thesis, Colorado State University, Department of Atmospheric Science.

Tripoli, G. J., and W. R. Cotton, 1982: The colorado state university three-dimensional cloud/mesosclae model - 1982. part I: General theoretical framework and sensitivity experiments. *J. Rech. Atmos.*, **16**, 185–219.

Trochkine, D., Y. Iwasaka, A. M. M. Yamada, Y.-S. Kim, D. Z. T. Nagatani, G. Shi, and Z. Shen, 2003: Mineral aerosol particles collected in dunhuang, china, and their comparison with chemically modified particles collected over japan. *J. Geoph. Res.*, **108**.

Twomey, S., 1977: The influence of pollution on shortwave albedo of clouds. *J. Atmos. Sci.*, **34**, 1149–1152.

Uno, I., and Coauthors, 2003: Regional chemica weather forecasting system cfors: Model descriptions and analysis of surface observations and japanese island stations during the ACE-asia experiment. *J. Geoph. Res.*, **108(D23)**.

Uno, I., and Coauthors, 2004: Numerical study of asian dust transport during the springtime of 2001 simulated with the chemical weather forecasting system (CFORS) model. *J. Geoph. Res.*, **109,D19S24**.

VanCuren, R., and T. Cahill, 2002: Asian aaerosols in north america: Frequency and concentration of fine dust. *J. Geoph. Res.*, **107**.

VandenHeever, S., G. G. Carrió, W. R. Cotton, and P. J. DeMott, 2006: Impacts of nucleating aerosol on florida storms. part i: Mesoscale simulations. *J. Atmos. Sci.*, **63**, 1752–1776.

Walko, R. L., L. E. Band, J. Baron, T. G. F. Kittel, R. Lammers, and T. J. Lee, 2000: Coupled atmosphere-biophysics-hydrology models for environmental modeling. *J. App. Meteo.*, **39**, 931–944.

Wang, J., S. A. Christopher, U. S. Nair, J. S. Reid, E. M. Prins, J. Szykman, and J. L. Hand, 2006: Mesoscale modeling of central american smoke transport to the United States: 1. top-down assessment of emission strength and diurnal variation impacts. *J. Geoph. Res.*, **111**.

Wang, J., U. Nair, and S. A. Christopher, 2004: Goes 8 aerosol optical thickness assimilation in a mesoscale model: Online integration of aerosol radiative effects. *J. Geoph. Res.*, **109**.

Wurzler, S., T. G. Reisin, and Z. Levin, 2000: Modification of mineral dust particles by cloud processing and subsequent effects on drop size distributions. *J. Geoph. Res.*, **105**, 4501–4512.

Yin, Y., S. Wurzler, Z. Levin, and T. G. Reisin, 2002: Interactions of mineral dust particles and clouds: Effects on precipitation and cloud optical properties. *J. Geoph. Res.*, **107**.

Zhang, L., S. Gong, J. Padro, and L. Barrie, 2000: A size-segregated particle dry deposition scheme for an atmospheric aerosol module. *Atmos. Environ.*, **35**, 549–560.